Nature of the Electronic States in Monolayer WTe_2

Bosong Sun

A dissertation

submitted in partial fulfillment of the

requirements for the degree of

Doctor of Philosophy

University of Washington

2021

Reading Committee:

David H Cobden, Chair

Xiaodong Xu

Anton Andreev

Program Authorized to Offer Degree:

Physics

University of Washington

Abstract

Nature of the Electronic States in Monolayer WTe_2

Bosong Sun

Chair of the Supervisory Committee:
Professor David H Cobden
Department of Physics

Quantum materials are those with essential properties that cannot be described in terms of semiclassical particles and elementary quantum mechanics. In these materials, strong electronic correlations or electronic order, such as superconducting or magnetic order, or topologically nontrivial electronic structure play a key role. The study of two-dimensional quantum materials was triggered by the discovery of graphene as the first stable, isolated atomic monolayer. Beyond graphene, the emergence of other atomically thin two-dimensional materials, such as transition metal dichalcogenides, has offered a promising platform for realizing tunable quantum states.

This thesis focuses on the nature of electronic states in monolayer tungsten ditelluride (WTe_2). In the first part, I will introduce the discovery of the quantum spin Hall insulator (QSHI) state and

superconducting state in single layer WTe_2. There, the carrier density-dependent phase transition from a topological insulator to superconductor hints at BCS-like excitonic condensation in this exotic material. In the second part, I will address studies of the possibility of forming excitons and an exciton condensate in monolayer WTe_2 with both experimental and theoretical evidence. Then, I will show studies of stacking induced ferroelectricity in few-layer WTe_2 and illustrate that bilayer WTe_2 is another potential excitonic insulator candidate with further study on its insulating state. At the end, I will talk about a selection of other approaches to studying two-dimensional materials and give an outlook to future opportunities in the study.

TABLE OF CONTENTS

LIST OF FIGURES

LIST OF TABLES

ACKNOWLEDGEMENTS

Before I started my PhD journey, I was told "A PhD is the crowning achievement in academia, but the road towards the finishing line proves to be a strenuous climb of resilience and perseverance." When I am so close to completing my PhD, I reflect on my progress as a student. I am glad I had so many great peers and friends with me, who made this a joyful, albeit stressful journey. It is my great pleasure to thank them.

First and foremost, I am extremely grateful to my PhD advisor, Prof. David Cobden. He is a great and very knowledgeable scientist. He often shows the subtlety of "chalk talk" – illustrating and simplifying the question to make the key to solve it jump to mind. His guidance has helped me in all the time of research. He is not only a mentor for my research, but also for my life. Back in 2020, I was struggling to look for a job since the market became shockingly tough due to the COVID-19 pandemic. His support stayed with me during that time. I will always keep it in mind. Now, I have found one position and am about to start a new journey. I could not have imagined having a better advisor for my PhD study.

Besides my advisor, there are other two professors helping me a lot on condensed matter experiments. Prof. Xiaodong Xu gave me lots of advice. He is a great and enthusiastic scientist with exceptional intuition in physics. Collaborations with his lab are always smooth and successful. I am frequently motivated by his style, "be more efficient". Almost all my important projects are about WTe_2 study. They could not have been done without the beautiful WTe_2 crystals grown in Prof. Jiun-Haw Chu's lab. Furthermore, Prof. Jiun-Haw Chu is very resourceful and is

an inspiration to me. I have to say, teamwork between the labs at the University of Washington (UW) is incredibly awesome. I will expand upon this later.

I also would like to thank the rest of my supervisory committee. Prof. Anton Andreev explained many concepts on condensed matter theory to me. Prof. Marcel P Den Nijs and Prof. Andreas Karch cared about my academic progress and career planning. Prof. Alejandro Garcia and Prof. Vincent Holmberg are very responsible. I really appreciate all the professors' encouragement, invaluable suggestions and insightful comments.

Outside UW, I especially thank Prof. Massimo Rontani from CNR-NANO (Modena, Italy). I had a great time and learned a lot when we discussed exciton condensation in monolayer WTe_2. Meanwhile, I specially thank Prof. Yongtao Cui and Xiong Huang from UC Riverside, who did great scanning microwave impedance microscopy measurements on my monolayer WTe_2 devices. Without them, I could not have gotten the very beautiful results in my paper.

Studying at UW is so enjoyable. I credit this to my wonderful friends, lab mates and colleagues. All my lab mates, past and present, are excellent. I wish to express my gratitude for the kindness of Dr. Zaiyao Fei and Dr. Boris Dzyubenko who welcomed me into the group and showed me a great deal on how experiments are conducted. I am deeply indebted to Zaiyao, who taught me all aspects of the project when I was a newbie. Dr. Tauno Palomaki is a senior researcher. He guided me on my PhD's path and gave me many recommendations on my career. Dr. Wenjin Zhao is a terrific collaborator and always gets the job well done. Dr. Paul Nguyen is an expert on ARPES. I learned a lot from him. Furthermore, he gave me many useful tips about how to give a fabulous academic presentation. That makes up for my shortcoming in using English as a second language. Elliott Runburg and Arnab Manna are reliable teammates when we have to take measurements by

the cryostat in turns. Eric Lester just joined us last year. I am pretty sure he will have a lot of fun in the lab. I wish big success in his research.

Teamwork between labs at UW is incredibly awesome. Graduate students in different groups share their knowledge and techniques from different points of views. Powered by the MRSEC (Materials Research Science and Engineering Centers), I have been able to use many other labs' facilities. Each piece of equipment is managed by one or two graduate students – local experts on the respective techniques. I get the good Raman spectra on my sample with the help of John Cenker in Prof. Xu's lab. And I really appreciate the steady WTe_2 crystal supply offered by Paul Malinowski in Prof. Chu's lab. Of course, I also get a great deal of help from others. The critical equipment we share between our labs include electron beam lithography, electron beam evaporation, dilution fridge, glove box, atomic force microscopy, cryostats, etc. It bears mentioning that I am pleased to keys to three different labs.

I want to thank the guys in Prof. Xu's group, Prof. Chu's group and Prof. Matthew Yankowitz's group. I was never alone when I decided to work at night in the lab. I could find Sanfeng Wu, Xinghan Cai, Genevieve Clark, Tiancheng Song, Minhao He and other members all the time. They always inspire me. Especially, Gen can show up energetically in the lab at any time of the day. Perhaps, Dr. Gen Clark is the hardest-working person I have ever met. Tiancheng is very diligent and his mind is full of many novel ideas. Prof. Sanfeng Wu and Prof. Xinghan Cai taught me what the important things are for a PhD.

I will cherish countless hours I spent in the lab as we planned our future and wondered what would become of us. Every friend helps me see a bigger picture from different views and understand how much joy there is while working together.

In addition, I thank Joshua Kahn, Matthew Adams, Kasey James French, Kay Jayachandran, Quinn L'Heureux, Sam Goertz, Blake Owen, Zhenghao Fu, Prof. Jennifer Heath, Prof. Qi Zhang, Dr. Kyle Seyler, Dr. Pasqual Rivera, Dr. Ding Zhong, Jiaqi Cai, Dr. Dmitry Ovchinnikov, Dr. Zhong Lin, Dr. Xi Wang, Dr. Yingqi Wang, Dr. Nathan Wilson, Dr. Bevin Huang, Kyle Hwangbo, Jiayi Zhu, Eric Anderson, Yinong Zhang, Joshua Mutch, Joshua Sanchez, Qianni Jiang, Yue Shi, Dr. Zhaoyu Liu. Dr. Xiayu Linpeng, Xuetao Ma, Chun-Chih Tseng, Prof. Fucai Liu. Working with them nurtured my love of physics and I enjoy every part working in the lab. Additionally, I want to thank my friends outside physics academia. I have had a lot of fun with them when we went biking and hiking, also played board games.

Finally, I want to pour out my warmest and dearest thanks to my fantastic family for their love, tremendous understanding and cheering throughout my life. My wife and my parents are always supporting me with their endless love at anytime and anywhere. I had an amazing life in Seattle. I will absolutely miss this part of my life's journey as a PhD student.

DEDICATION

TO MY PARENTS

for their never-ending love and support

AND TO MY WIFE

for making everything possible

Chapter 1. Introduction

1.1 2D electron gas

A two-dimensional electron gas (2DEG) is a gas of electrons free to move in two dimensions but are confined in the third dimension. Due to quantum mechanics, the energy levels in that direction are quantized, leading to a lot of interesting physical properties and potential applications of smaller and faster electronics.

The most conventional 2DEG is found in the metal-oxide-semiconductor field-effect transistor (MOSFET), which is illustrated in Fig. 1.1. The Fermi energy of p-type Si is inside the band gap but close to the valence band edge. It terminates on an oxide insulator (e.g. SiO_2) with a very large band gap, that electrons cannot penetrate into. Behind this oxide barrier is a metallic gate. With a positive voltage applied to this gate, the bands bend downward as one approaches the semiconductor/oxide interface. The Si conduction band edge is pulled below the Fermi energy within a thin layer known as the inversion layer. We thus obtain a degenerate electron gas that is confined to this (2D) inversion layer. Its motion in the direction perpendicular to the interface is restricted and so forms discrete "particle in a box" quantum levels (known as electronic subbands). Meanwhile its motion in the plane parallel to the interface is "free", and the planar solutions of the Schrödinger equation form extended Bloch waves. We thus have a genuine 2DEG.

The MOSFET is among the most important devices for modern integrated circuit technology such as microprocessors and semiconductor memory[1]. In terms of physics, it is more fascinating that fundamental science of 2DEGs has been realized in this and other systems. A good example is the integer quantum Hall effect (IQHE), which was first discovered by von Klitzing in a Si MOSFET.

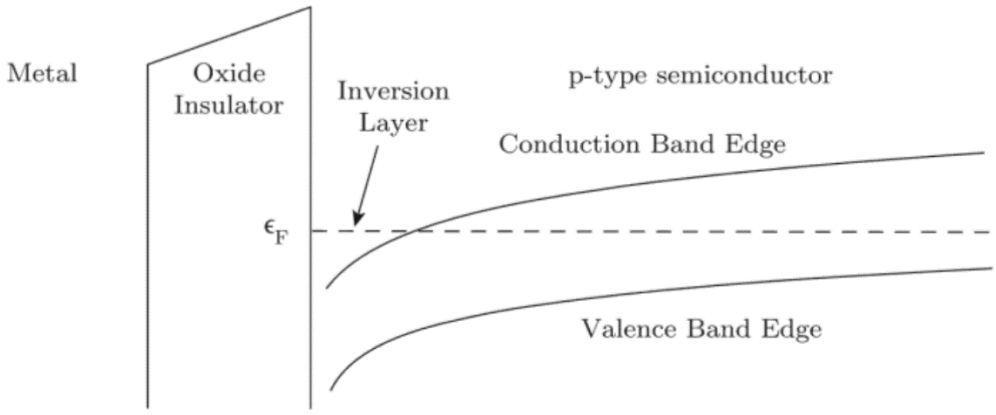

Figure 1.1 An illustration of metal-oxide-semiconductor field-effect transistor (MOSFET). (Figure reproduced from reference[2])

1.1.1 Graphene

Graphene, consisting of a single layer of carbon atoms, is the first two-dimensional material ever found. It can be isolated and identified easily using the Scotch tape technique. In this section, I will briefly introduce the electronic properties of graphene, which paves the way to understanding quantum spin Hall insulator physics in the following sections.

In graphene, there are three fully occupied bonding bands and three empty anti-bonding bands at high energy (called σ bands). Locally one can understand them by mixing the s orbital with p_x and p_y orbitals to form orbitals that extend along the directions of nearest-neighbor bonds, known as σ orbitals. The bonding and anti-bonding combinations of these σ orbitals have energies far below and far above the Fermi energy, respectively. This leaves us with one electron (and one orbital) per atom that does not pair up with neighboring atoms, and it is this orbital that dominates the low-energy physics of graphene. This remaining orbital is basically the p_z orbital that sticks out of the graphene plane and is called the π orbital. In the following we will treat the bands formed by the π orbitals using the tight-binding method and ignore their coupling with other orbitals. For

simplicity, we will also ignore the non-zero overlap between π orbital wave functions on different carbon atoms. Alternatively, we can also formulate the problem in terms of the (orthonormal) Wannier orbitals that correspond to the π bands.

Using $|i\rangle$ to represent the π orbital of the ith atom and setting its energy to be zero, the tight-binding Hamiltonian takes the form

$$H = -t\sum_{\langle ij\rangle}(|i\rangle\langle j| + |j\rangle\langle i|) = -t\sum_{i\in A,\vec{\delta}}\left(|i\rangle\langle i+\vec{\delta}| + h.c.\right),$$

where $\langle ij\rangle$ represents a nearest-neighbor pair, and $\vec{\delta}$ is a contact vector, and $a = |\vec{\delta}| \approx 1.42$ Å as the lattice constant. Here, we have $\vec{\delta}_1 = (1,0)$ and $\vec{\delta}_{2,3} = \left(-\frac{1}{2}, \pm\frac{\sqrt{3}}{2}\right)$.

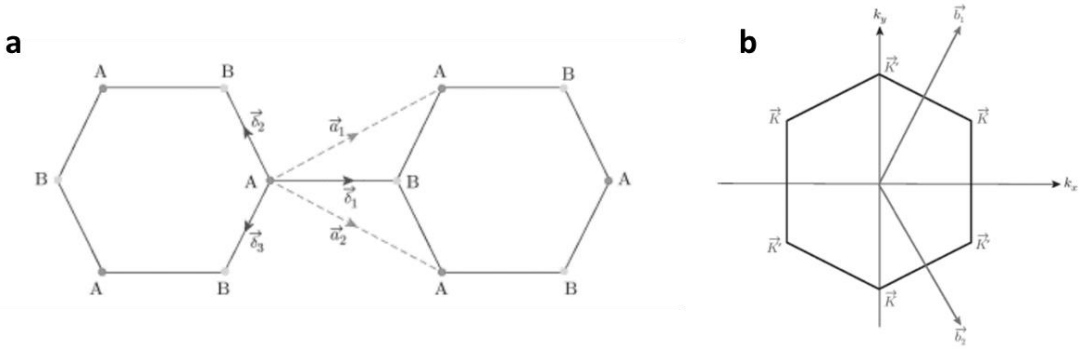

Figure 1.2 (a) Graphene's honeycomb lattice structure. The honeycomb lattice is a triangular lattice with a two-atom basis. The primitive lattice vectors of the underlying triangular lattice are given by the dashed lines. (b) The first Brillouin zone of graphene's underlying triangular lattice. $\overrightarrow{b_1}$ and $\overrightarrow{b_2}$ are primitive unit vectors of the reciprocal space. $\vec{K}$ and $\vec{K}'$ are the two inequivalent Brillouin zone corners that become Dirac points of the spectrum. (Figure reproduced from reference[2])

Since we have two atoms per unit cell, there are two such states for each momentum $\vec{q}$ (one for each sublattice):

$$|\vec{q}\rangle_{A,B} = \frac{1}{\sqrt{N}} \sum_{j \in A,B}^{N} e^{i\vec{q}\cdot\vec{R}_j} |j\rangle.$$

Here $\vec{q}$ is restricted to the first Brillouin zone, which is hexagonal. Our further discussion focuses on the zone corners; while two of the six, namely $\vec{K} = \left(\frac{2\pi}{3}, \frac{2\pi}{3\sqrt{3}}\right)$ and $\vec{K}' = -\vec{K}$, are inequivalent, the others differ from one of them by a reciprocal lattice vector. The Hamiltonian is rewritten as

$$H = -t \sum_{\vec{q}} (|\vec{q}\rangle_A, |\vec{q}\rangle_B) h_{\vec{q}} (\langle\vec{q}|_A, \langle\vec{q}|_B)^T,$$

where $h_{\vec{q}}$ is 2×2 Hermitian matrix, $h_{\vec{q}} = \begin{pmatrix} 0 & f(\vec{q}) \\ f^*(\vec{q}) & 0 \end{pmatrix}$, in which $f(\vec{q}) = \sum_{\vec{\delta}} e^{i\vec{q}\cdot\vec{\delta}} = \sum_{i=1}^{3} e^{i\vec{q}\cdot\vec{\delta}_i}$.

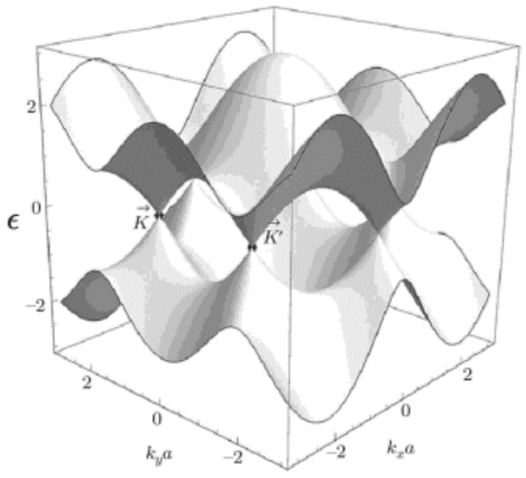

Figure 1.3 Graphene's band structure. Note the Dirac points at $\vec{K}$ and $\vec{K}'$. The other degeneracy points are not independent because they are connected by reciprocal lattice vectors to either $\vec{K}$ or $\vec{K}'$. (Figure reproduced from reference[2])

Diagonalizing $h_{\vec{q}}$ yields the spectra of graphene's conduction and valence bands: $\epsilon_{\pm}(\vec{q}) = \pm t|f(\vec{q})|$. The Fermi energy is at $\epsilon_F = 0$, and notably $\epsilon_{\pm}(\vec{K}) = \epsilon_{\pm}(\vec{K}') = 0 = \epsilon_F$. Thus, there is no band gap and so, graphene is a semimetal. Expanding $\epsilon_{\pm}(\vec{q})$ near $\vec{K}$ we find $\epsilon_{\pm}(\vec{K} + \vec{k}) \approx \pm v_F |\vec{k}|$, where $v_F = \frac{3}{2} ta \approx 10^7\ m/s$. This is manifestly a linear, "Dirac" dispersion and $\vec{K}$ and

$\vec{K}'$ are often referred to as the Dirac points in graphene. I will reiterate this feature in Chapter 3 and introduce this as the key element to measure the chemical potential of monolayer WTe_2.

Now, we need to fix a deficiency of $h_{\vec{q}}$ – it is *not* periodic in reciprocal space: $h_{\vec{q}} \neq h_{\vec{q}+\vec{G}}$, since $\vec{\delta}$ is not a lattice vector of the underlying (triangular) Bravais lattice. We need to fix this by a gauge transformation, namely we introduce an additional ($\vec{q}$-dependent) phase to $|\vec{q}\rangle_B$ and work instead with $|\vec{q}\rangle_B = ie^{-i\vec{q}\cdot\vec{\delta}_1}|\vec{q}\rangle_B$, resulting in a change of $h_{\vec{q}}$ to

$$\tilde{h}_{\vec{q}} = -t\begin{pmatrix} 0 & \tilde{f}(\vec{q}) \\ \tilde{f}^*(\vec{q}) & 0 \end{pmatrix}, \text{ with}$$

$$\tilde{f}(\vec{q}) = ie^{-i\vec{q}\cdot\vec{\delta}_1}f(\vec{q}) = i\left[1 + e^{i\vec{q}\cdot\left(\vec{\delta}_2-\vec{\delta}_1\right)} + e^{i\vec{q}\cdot\left(\vec{\delta}_3-\vec{\delta}_1\right)}\right].$$

Here, $\tilde{h}_{\vec{q}}$ and $h_{\vec{q}}$ describe the same physics. Writing $\vec{q} = \vec{K} + \vec{k}$ and expanding $\tilde{f}(\vec{q})$ to linear order in $\vec{k}$, we obtain

$$\tilde{f}(\vec{q}) \approx \nabla_{\vec{q}}\tilde{f}(\vec{q})|_{\vec{q}=\vec{K}} \cdot \vec{k} = -\frac{3}{2}\left(k_x - ik_y\right), \text{ thus}$$

$$\tilde{h}_{\vec{q}\approx\vec{K}} \approx v_F\begin{pmatrix} 0 & k_x - ik_y \\ k_x + ik_y & 0 \end{pmatrix} = v_F\left(\sigma_x k_x + \sigma_y k_y\right) = v_F\vec{\sigma}\cdot\vec{k}.$$

It also takes the form of a 2D massless Dirac Hamiltonian. The two effective Hamiltonians $H_{\vec{K}}$ and $H_{\vec{K}'}$ can be written in a unified manner by introducing a valley degree-of-freedom index τ_z, where $\tau_z = \pm 1$ for $\vec{K}$ and $\vec{K}'$ respectively, which yields

$$H = v_F\left(\tau_z\sigma_x p_x + \sigma_y p_y\right).$$

Here, $\vec{p}$ should be understood as the operator of lattice momentum measured from $\vec{K}$. I will revisit this equation in the Section 1.3, which is about two-dimensional topological insulator.

1.2 Layered two-dimensional materials

Beyond conventional quantum wells and single layer graphene introduced in the previous sections, more and more two-dimensional materials have caught tremendous attention because of their physical properties. The classes of 2D materials span a broad range including semimetal (e.g. graphene), semiconductor (e.g. MoS_2, WSe_2), insulator (e.g. hBN), charge density wave material (e.g. TaS_2), magnet (e.g. CrI_3) superconductor (e.g. $NbSe_2$) and others.

Along with the rapid development of controllable fabrication methods, numerous device geometries based on 2D materials with extraordinary performance have been devised and demonstrated, including tunneling transistors, spintronic devices and photodetectors. This makes for a rich phase diagram which can be accessed by varying electronic doping level, magnetic field, pressure and temperature in a single device. Meanwhile, the ability to assemble 2D material into 2D "van der Waals" structures have enabled many novel properties to be discovered. The twist angle between the layers in these heterostructures can affect and be used to tune the constituent properties. Intriguingly, such heterostructures do not need to be made of entirely different materials. Indeed, twisted homobilayer systems, such as twisted bilayer graphene, have demonstrated exotic phenomena such as correlated insulator behavior[3] and unconventional superconductivity[4].

1.3 Introduction to 2D topological insulator

In 2005, Kane and Mele explained the concept of topological insulators by discussing ways to open a gap or, equivalently giving a mass to the Dirac fermions in the graphene band spectrum[5,6]. There are two ordinary approaches: (i) the first method is to add a conventional mass, which is same at the two Dirac points. It comes from the sublattice potential difference, which breaks parity or inversion symmetry but respects time-reversal symmetry; (ii) the second method is to add a

Haldane mass, which has opposite signs at the two Dirac points. It can be generated by having imaginary next-nearest-neighbor hopping-matrix elements, which breaks time-reversal symmetry but respect inversion symmetry. These can be summarized by a four-component Dirac-like Hamiltonian.

$$H = v_F\left(\tau_z\sigma_x p_x + \sigma_y p_y\right) + m_R\sigma_z + m_H\tau_z\sigma_z,$$

where the σ and τ Pauli matrices act on the sublattice and valley (or K and K') spaces respectively.

Under inversion (or parity transformation, $\mathcal{P}$) we reverse the A and B sublattices as well as the K and K' points, thus $\sigma_z \to -\sigma_z$ and $\tau_z \to -\tau_z$. Under time-reversal transformation (Θ) we reverse the K and K' points, but the A and B sublattices remain the same, thus $\sigma_z \to \sigma_z$ and $\tau_z \to -\tau_z$. It is thus clear that the regular mass term (m_R) is even under Θ but odd under $\mathcal{P}$, while the Haldane mass term (m_H) is odd under Θ but even under $\mathcal{P}$. Hence, there is a natural question to ask: can one have a mass term that respects both $\mathcal{P}$ and Θ?

Kane and Mele[5,6] pointed out that the answer is yes, provided that one invokes spin-orbit coupling. The simplest possibility would be a mass term of the form

$$m_{KM}\tau_z\sigma_z S_z,$$

where S_z is the $\hat{z}$ component of the electron spin operator $\vec{S}$. Since $\vec{S}$ is even under $\mathcal{P}$ but odd under Θ, it is easy to see that this mass term is even under both $\mathcal{P}$ and Θ. The way to generate this Kane-Mele mass term is simply to have two copies of the Haldane model, one for spin-up and the other for spin-down electrons, with opposite next-nearest-neighbor hoppings. The charge Hall conductance is zero due to cancellation between the up- and down-spin electrons, as guaranteed by the presence of time-reversal symmetry. However, there is quantized spin Hall conductance when the chemical potential is in the band gap. The spin Hall conductance is the difference between the Hall conductance of up- and down-spin electrons, corresponding to the spin current

response to a potential gradient. Hence, this state was initially dubbed a “quantum spin Hall state”, which is topologically non-trivial. Kane and Mele introduced the Z_2 index which characterizes the topological character of the state. The discussed quantum spin hall state has Z_2 index of 1.

The two-dimensional quantum spin Hall insulator (2D QSHI) state is also known as a two-dimensional topological insulator (2D TI). It has two branches of edge modes for each edge, one for spin-up and another for spin-down, which propagate in opposite directions. They are thus consistent with time-reversal symmetry and the overall system is achiral since Θ flips both the orbital motion and the spin direction. The directions of the spin and velocity of the modes are tied together, and such modes are called helical. We thus find that there can be topologically non-trivial bands in the presence of time-reversal symmetry, characterized by gapless helical edge modes.

1.4 Introduction to excitonic insulators

It was predicted several decades ago[7] that Coulomb interactions in a system with electron-hole (e-h) co-existence can make the normal semimetallic state unstable against the spontaneous appearance of excitons, i.e. bound e–h pairs. This can induce a phase transition to an insulating phase, called the excitonic insulator (EI) or Bardeen–Cooper–Schrieffer (BCS)-like excitonic condensation. The excitonic insulator phase emerges with a gap opening at the Fermi surface of the semimetal, in a manner analogous to the BCS gap in a superconductor.

In a monolayer semimetal, low carrier densities combined with reduced dimensionality provide the conditions for strong correlation effects. One possible form of such correlations is the pairing of electrons and holes in the equilibrium state to form excitons. At low temperatures, such excitons could condense to form an exciton insulator[7–10]. However, exciton formation is expected to be easily disrupted by free carriers which screen the binding interaction, and thus to occur only at low temperatures and near charge neutrality. A number of materials have been proposed as

excitonic insulator candidates ($TiSe_2$[11,12], Ta_2NiSe_5[13,14], Carbon nanotube[15], MoS_2[16]), but there is no consensus as to whether any truly contains excitons in equilibrium, either as a gas or as a coherent condensate, except in the case of bilayer heterostructure at high magnetic fields[17–20].

1.5 Outline and summary

The emergence of atomically thin 2D materials, such as transition metal dichalcogenides, opens up great opportunities for creating novel functional materials, and advances our understanding of phase transitions. This thesis focuses on the study of 2D phase transitions in thin tungsten ditelluride (WTe_2).

In Chapter 2, I will introduce studies of phase transitions in monolayer WTe_2. It was suggested that monolayer 1T'-WTe_2 could have a nontrivial Z_2 topological phase. I will talk about transport measurement and microwave impedance microscopy probing this property. Both confirm that single layer 1T'-WTe_2 is a two-dimensional topological insulator, exhibiting a ground state with an insulating interior and conducting edges. Also, I will show that monolayer WTe_2 can superconduct at low temperatures, a property that can be switched with electrostatic doping. From these results, we construct a complete phase diagram showing the presence of both edge conduction and superconductivity.

The phase transition captured by this phase diagram hints at a possible BCS-like excitonic condensation in 1T'-WTe_2. In Chapter 3, I will discuss detailed studies of monolayer WTe_2 to shed further light on this possibility. That discussion starts with the field- and doping-dependent behavior of conductivity and the electron chemical potential in the interior bulk of monolayer WTe_2. I will show that the conductivity develops a sharp, V-shaped dependence of conductance on electrostatic doping, while the chemical potential develops a ~43 meV step at neutrality. Such

features are not possible in the independent-electron picture. In the latter part of Chapter 3, I will mainly discuss about our calculation from first principles to demonstrate the formation of excitons.

Chapter 4 is primarily about the ferroelectric and insulating states in bilayer WTe_2. Using top and bottom gate electrodes, two- or three-layer WTe_2 exhibits spontaneous out-of-plane electric polarization, which can be directly measured using graphene as electric field sensor. I will also introduce the further theoretical work and potential application after demonstrating the measurements. Lastly, I will show some measurements which indicate bilayer WTe_2 is another potential excitonic insulator candidate. That can be a promising direction to study bilayer WTe_2.

In Chapter 5, I will briefly talk about other work which enrich the library fabrication methods for study of layered two-dimensional materials, such as applying built-in strain, inducing superconductivity into other non-superconducting materials via proximity effect, and tunneling devices.

Chapter 2. 1L WTe_2 – 2D topological insulator and superconductor

A 2D QSHI can be identified by its helical edge modes[5,21–23]. Candidate topological insulator states have already been observed in two-dimensional systems of quantum wells in Hg/CdTe[24] and InAs/GaSb[25]. However, the evidence for the helical edge mode in two-dimensional topological insulators has been limited to very low temperatures (i.e., near liquid helium temperature). In the search for high-temperature topological insulators, substantial efforts have focused on a variety of atomically thin materials[26–30], which hold the promise of advancing the field of topological physics using the tools developed for two-dimensional crystals. Owing to structural or chemical instabilities[28,30–32], however, experimental observation of the quantum spin Hall effect (QSHE) in monolayer system has proven challenging.

Monolayer transition metal dichalcogenides (TMDs), materials that are either two-dimensional semiconductors or semimetals depending on their structural phase, is one of the proposals for atomically thin topological insulator. It is suggested that an inverted band gap, resulting in a nontrivial Z_2 topological phase[28,33], can develop in TMD monolayers in the 1T' structure. In particular, monolayer WTe_2 has been found to stabilize the 1T' structure and host a two-dimensional topological insulator state[34–37]. In the first half of this chapter, I introduce quantum spin Hall insulator studies of monolayer WTe_2, reproducing results, figures and discussions from our published works[34,38].

Superconductors with a topologically nontrivial band structure have been predicted to exhibit exotic properties. We have previously reported that monolayer WTe_2 can be made to superconduct at around 1K[39]. In the second half of this chapter, I will reproduce the results therefrom to discuss how in single layer WTe_2 the phase transition from a 2D topological insulator to a superconducting state occurs at such a low carrier density that it can be readily induced by a simple electrostatic

gate[39,40]. In the end, the phase diagram constructed from measurements hints the unusual nature of the bulk state, which will be fully discussed in the Chapter 3.

2.1 Monolayer WTe_2

Layered transition metal dichalcogenides (MX_2) comprise 3 atomic layers, X-M-X. In the 1H and 1T structures, the atoms in each atomic layer are arranged in a triangular lattice. Three atomic layers stack together in Bernal (ABA) order for 1H and rhombohedral (ABC) for the 1T structure. Perhaps the most studied MX_2 materials are the semiconductors with M = W or Mo, and X = S or Se, and naturally have 1H stacking. Monolayer WTe_2 is also an MX_2; however, monolayer WTe_2 stabilizes the 1T' structure, a distorted form of 1T. As shown in Fig. 2.1, monolayer 1T' WTe_2 contains an inversion center (indicated by the red dot), a *y*-*z* mirror plane (M), a two-fold glide screw rotational axis (*x*-axis) and a 1D zigzag tungsten chain along *x*-axis. The bands near the Fermi level are mainly from tellurium *p* orbitals and tungsten *d* orbitals. By introducing spin-orbit coupling, a fundamental gap can be opened. Monolayer WTe_2 has predicted to be a quantum spin Hall insulator (QSHI) in 2014[28]. This attracted great attention to this system, and several types of experiments have since evinced that monolayer WTe_2 is indeed a QSHI[34,35,37,38,41,42].

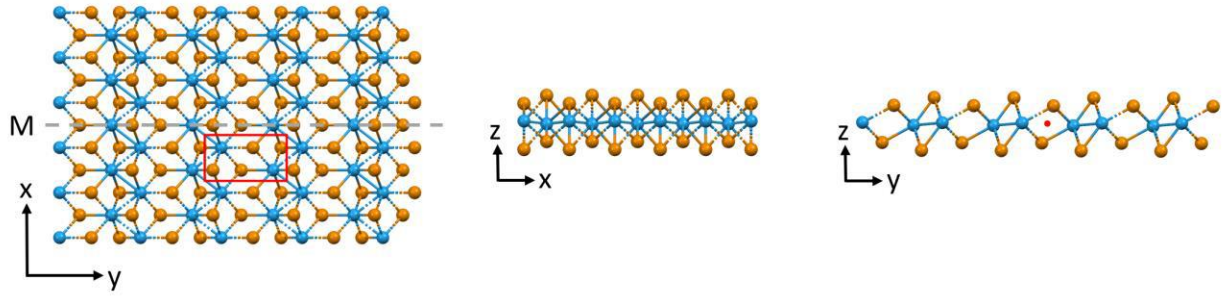

Figure 2.1 Crystal structure of monolayer WTe_2. Dashed grey line in *x*-*y* view is the *y*-*z* mirror plane. The red box indicates the unit cell. The inversion center is pointed by a red dot. Orange ball: Te atom; Blue ball: W atom.

2.1.1 Crystal growth

WTe_2 single crystals were grown via Te-rich self-flux with the following procedure[43]. Elemental W power and Te shot were loaded into alumina crucibles in the molar ratio 1:50 with a total charge of 3.5 g. The crucibles were loaded into quartz tubes and sealed under an evacuated argon atmosphere. The tubes were then placed in a box furnace and heated to 1000 ℃ over 12 hours, held at 1000 ℃ for 12 hours, cooled for 460 ℃ over 100 hours, and finally decanted at 460 ℃ via centrifuge. This procedure resulted in large, high quality single crystals of WTe_2 with ribbon-like morphology and typical dimensions 5 mm × 0.3 mm × 0.01 mm.

2.2 Edge conduction in 1L WTe_2

As previously mentioned, edge conduction in monolayer WTe_2 was first observed in this work of ours[34]. Figure 2.2 shows two-terminal conductance between adjacent contacts as a function of gate voltage V_g measured at a series of different temperatures. In the high doping regime, the conductance increased with decreasing temperature. In the low doping regime, the conductance initially decreased with cooling. Below 100 K, the conductance of the monolayer stopped dropping and instead broadened into a plateau of conductance, at ~16 μS in device MW1. To find the origin of the plateau, another monolayer device MW3 which employed a series of alternating pincer-shaped contacts overlapping a single straight edge of a monolayer flake was designed, as shown in the inset of Fig. 2.2b. The middle contact could be either floated or grounded to respectively pass or stop edge current. Hence, this geometry allowed us to measure the conductance including or excluding any contribution from the edge path. When the middle contact was grounded, only bulk current could pass and the plateau dropped to 0 conductance (blue curve in Fig. 2.2b). Hence

distinguishing the insulating bulk and metallic edge of monolayer WTe_2. We used a similar method to study the interior bulk of monolayer WTe_2, which will be fully discussed in Chapter 3.

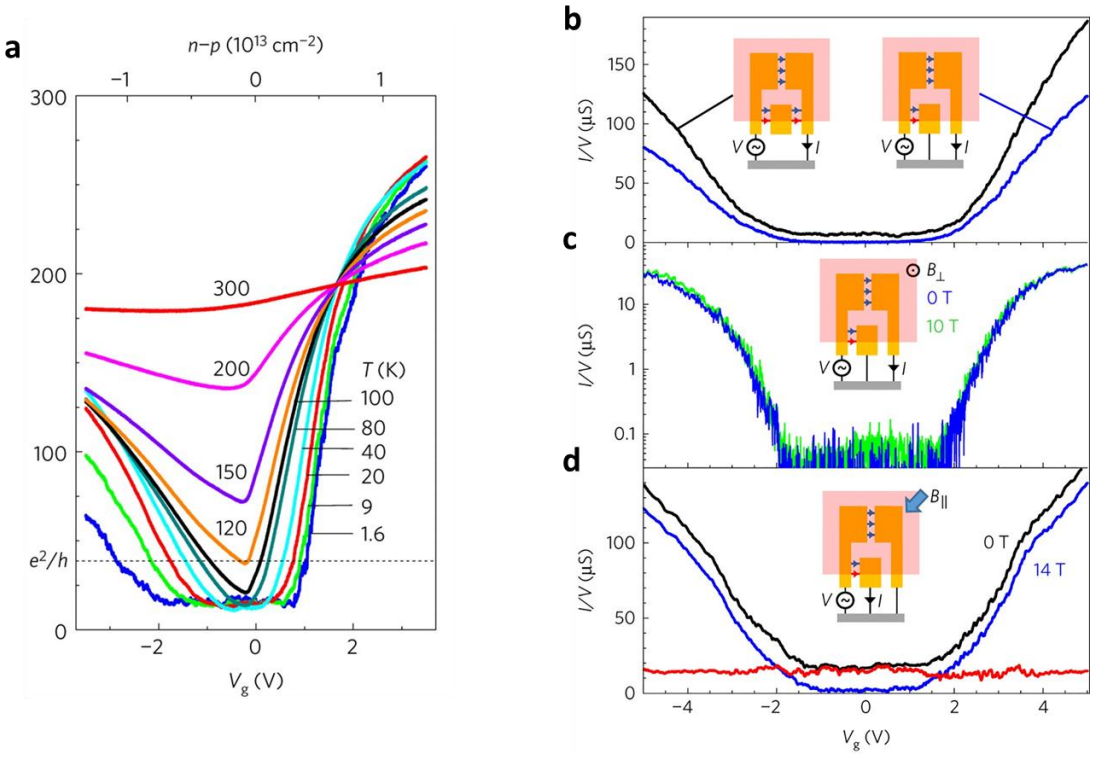

Figure 2.2 Edge conduction in monolayer WTe_2. (a) Two terminal conductance as a function of gate voltage (V_g) at different temperatures (Device MW1). (b-d) Measurements on device MW3 (the contact separation along the edge is 0.22 μm; the pincer spacing is 0.28 μm). (b) As indicated by the insets, the black trace is the two-terminal conductance between the outer contacts and the blue trace is I/V measured with the center contact grounded ($T = 10$ K). In the insets, red and blue arrows indicate edge and bulk current paths, respectively. (c) Same measurement as for the blue trace in (b) but at 1.6 K, on a logarithmic scale, showing the very weak effect of perpendicular magnetic field of 10 T. (d) Effect of in-plane magnetic field $B_{\parallel} = 14$ T on I/V between adjacent contacts ($T = 10$ K). The red trace is the magnitude of the decrease.

We also studied the difference of how magnetic field affects bulk and edge conduction. Fig. 2.2c shows measurements of the same quantity at 1.6 K, on a logarithmic scale, both with (green trace) and without (blue trace) a perpendicular magnetic field $B_{\perp} = 10$ T. Near charge neutrality

the bulk conductance was unmeasurably small at this temperature. In Fig. 2.2d, the black trace is a measurement at zero magnetic field between two adjacent contacts, using the configuration shown in the inset. The blue trace is the same measurement with an in-plane field $B_{\parallel}$ of 14 T. Since the bulk conductivity is almost independent of magnetic field, the decrease in I/V must be associated with the edge. Near $V_g = 0$, where the bulk is insulating, I/V drops nearly to zero. This implies that the edge conduction is strongly suppressed by the magnetic field. In addition, the magnitude of the drop is almost same at all V_g. Thus edge makes a roughly constant contribution to the conductance, independent of gate voltage and bulk conductivity.

2.3 Direct imaging of 1L WTe_2

In addition to transport measurements, we were able to directly image the local conductivity of monolayer WTe_2 and establish beyond doubt that conduction is indeed strongly localized to the physical edges at temperatures up to 77 K as reported in another previous work of ours[38]. To perform this, our collaborator Prof. Cui and his group used a recently developed mode of probe microscopy, microwave impedance microscopy (MIM). MIM probes local electromagnetic response (electrical conductivity and permittivity) of nano-scale material with spatial resolution of sub 100 nm. Since MIM is nondestructive, it can be utilized to probe a wide variety of materials, from insulators, semiconductors to metals.

Here I will briefly reproduce our reported results and discussion of MIM of WTe_2 of edges[38]. Later in Section 3.3.1, I will bring up MIM again – with the assistance of MIM, we will gain understanding of the unusual nature of the bulk state of monolayer WTe_2. The MIM technique probes the local conductivity by analyzing the imaginary and real parts of the complex admittance (MIM-Im and MIM-Re, respectively) between a sharp conducting tip and the sample (shown schematically in Fig. 2.3a). MIM-Im characterizes the amount of screening of the microwave

electric field at the tip by the sample, while MIM-Re characterizes the dissipation generated by the induced oscillating currents in the sample. MIM-Im increases monotonically as the resistivity decreases, while MIM-Re is strongly peaked at an intermediate resistivity value. Fig. 2.3b-e are optical and MIM-Im images of a large monolayer WTe_2 flake. The MIM maps highlight the physical edges of the flake as brighter and more conductive than the interior bulk.

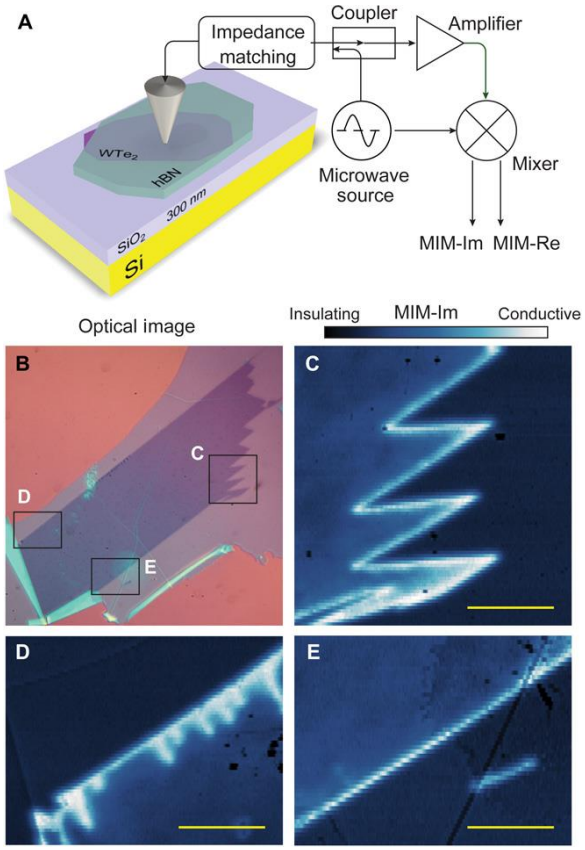

Figure 2.3 Imaging edge conductivity in monolayer WTe_2 (a) Schematics of the technique and device structure. (b) Optical image of a WTe_2 monolayer exfoliated onto SiO_2 and covered with a 10-nm-thick hBN. (c-e) Measured at $T = 8$ K and $B = 0$, MIM-Im images of the regions marked in (b) are plotted in white (conductive)-dark (insulating) color scale. Scale bars, 5 μm.

2.3.1 Additional conduction features observed by MIM

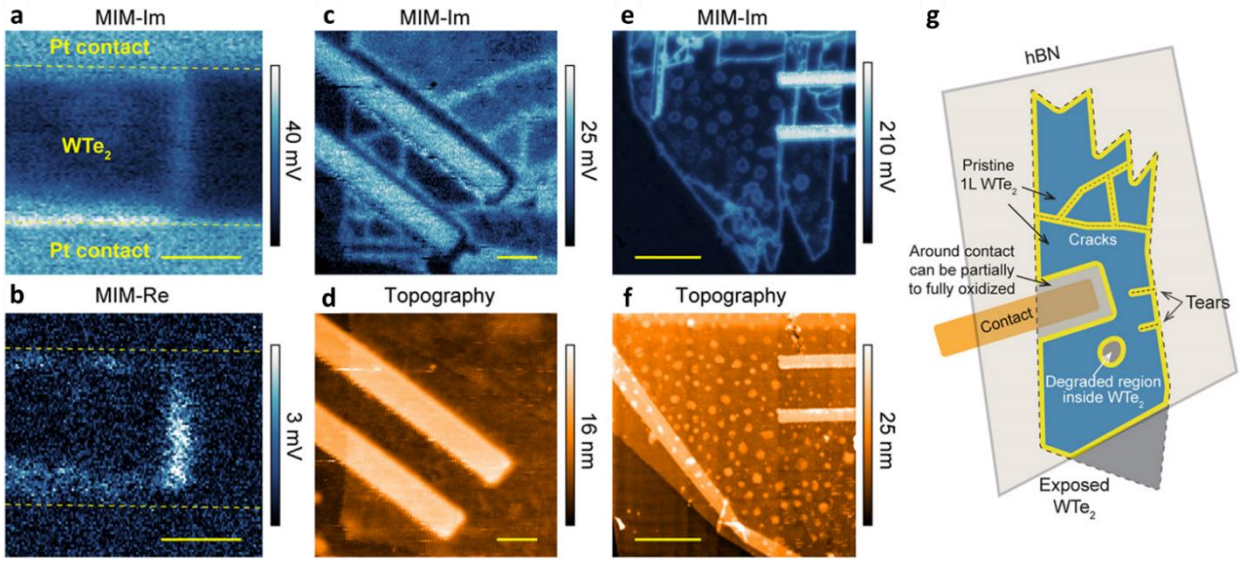

Figure 2.4 Conductivity features near contacts and around defects in monolayer WTe_2. (a and b) MIM-Im and MIM-Re images of part of a monolayer WTe_2 between two Pt contacts, measured at $T = 480$ mK, $V_g = 0$ V, and $B = 12$ T. Scale bars, 500 nm. (c and d) MIM-Im and topography images of part of a second monolayer WTe_2 device, measured at $T = 10$ K, $V_g = 3.3$ V and $B = 0$ T. Scale bars, 1 µm. (e and f) MIM-Im and topography images of part of a third monolayer WTe_2 device, measured at $T = 10$ K, $V_g = 0$ V and $B = 9$ T. Scale bars, 3 µm. (g) Cartoon illustrating various conductivity features observed in the experiments.

As shown in Figure 2.4, MIM mapping reveals additional details, which have important consequences for device fabrication and performance. It offers a roadmap to building clean devices for monolayer WTe_2, as well as for layered materials in general. Figure 2.4a and b show the MIM-Im and MIM-Re signals from monolayer WTe_2 in between two thin Pt contacts. A strip of enhanced conductivity was observed in the WTe_2 bulk adjacent to the contact edges. In contrast, a MIM-Im map near other contacts (Fig. 2.4c) reveals highly insulating (dark) regions around the contacts. This is despite the topography (Fig. 2.4d) appearing continuous and featureless. Additionally, in Figures 2.4c & d networks of conducting lines are observable that do not

correspond to any physical edge. Also, in Fig. 2.4e, there are small conducting rings, which match well with bubbles seen in a topographic scan (Fig. 2.4f). Fig. 2.4g schematically summarizes these various conductivity features.

2.4 QSHI in 1L WTe_2 – quantized edge conduction

The hallmark of quantum spin Hall insulator is to have quantized conductance of $\sim e^2/h$ per edge. While ours was the first report of edge conduction in 1L WTe_2, we only showed a conductance of $\sim e^2/2h$ from what should have been a single edge. More recently, edge conduction closer to e^2/h up to 100 K was been observed[37]. In that work, by measuring resistance change from a bulk-metallic state (doped) to a bulk-insulating state (undoped), the offset resistance $\Delta R = R(\text{doped}) - R(\text{undoped})$ shows the plateau of $h\backslash 2e^2$, which is the anticipated resistance of two helical edges. This offers a method to measure quantized conductance indirectly which we were able to reproduce using a similar geometry (Figure 2.5).

Indeed, we showed a plateau of $G \sim e^2/h$ at $T \leq 40$ K by measuring two-terminal conductance directly (Fig. 2.5a). We have already seen via MIM several different possible types of conductivity features which prohibits the measured conductance from reaching h/e^2. With this in mind, we employed mechanical cleaning[44] of the metal contacts on the hBN/graphite back gate before placement of the WTe_2 monolayer to remove residual contamination from the nanofabrication technique. Fig. 2.5 shows the conductance G vs. back gate voltage V_{bg} between the pair of two closest Pt contacts shown in the inset. As T cools down, the conductance shows the plateau of e^2/h along one single edge. Meanwhile, the conductance shows independence of electronic doping at T < 10 K, which is another hall mark of quantum spin Hall insulator. Limited by the resolution of MIM, we cannot clearly see the inside of channel. Due to the transfer process,

several internal conducting lines still exist. Hence, it needs further work to confirm the plateau of e^2/h conductance via direct two-terminal measurement.

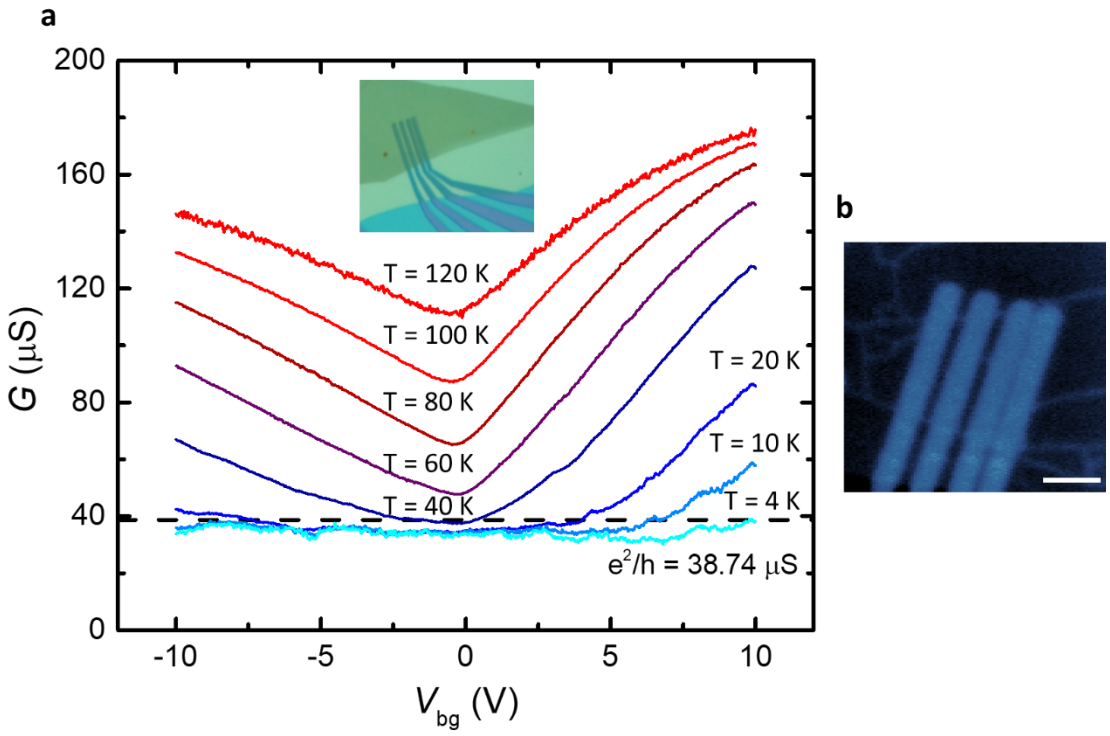

Figure 2.5 (a) Two-terminal conductance, showing the plateau of $G \sim e^2/h$ at low temperature, vs. gate voltage (V_g). Inset: optical image of the monolayer device MW9 (b) MIM-Im image of the monolayer device MW9, scale bar: 1 μm.

2.5 Superconductivity in monolayer WTe_2

As demonstrated in the previous sections, monolayer WTe_2 exhibits very different transport properties from its bulk and few layer counterpart at low doping levels. Fig. 2.3 shows the two-terminal transport characteristic for monolayer device MW1 at various temperatures, from 300 K to 1.6 K. When increasing the gate voltage above ~1.7 V, monolayer WTe_2 undergoes an insulator to metal transition, i.e., the conductance increases as T decreases.

Our previous work[39], done in collaboration with Prof. Joshua A. Folk's group, shows that monolayer WTe_2 becomes a superconductor in the interior with a large positive gate voltage when temperature drops to below 1 K. As shown in Fig. 2.6, the critical temperature was highly tunable with the electrostatic gate, from about 700 mK at 2×10^{13} cm^{-2} to below 200 mK at a low doping of 5×10^{12} cm^{-2}. For even lower doping levels, the 2D bulk becomes an insulator.

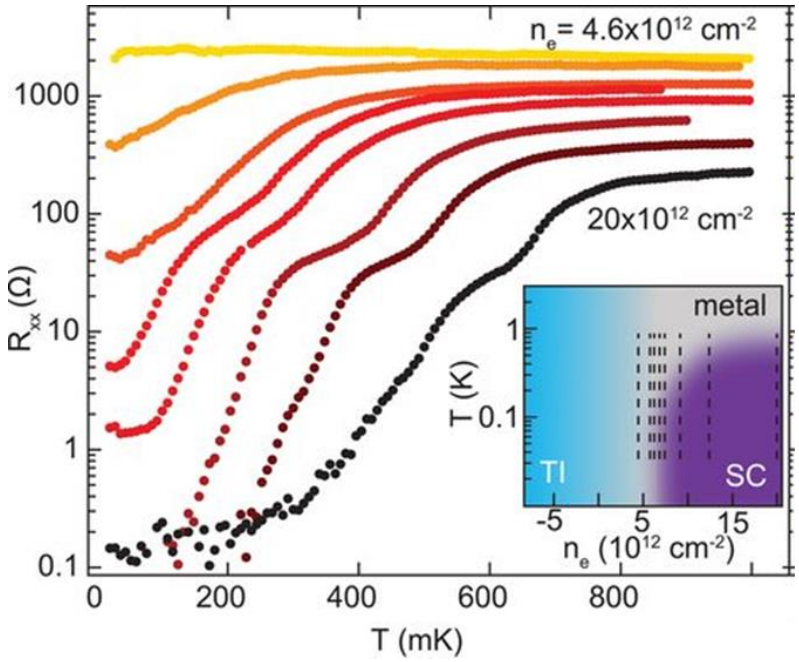

Figure 2.6 Resistance characterization of device M1 R_{xx} on log scale versus temperature T at a series of positive gate doping levels n_e [20, 12, 8.5, 6.7, 6.1, 5.6, 5, and 4.6×10^{12} cm^{-2}] showing a drop of several orders of magnitude at low T for larger n_e. Inset: Location of sweeps on the phase diagram.

2.6 Constructed phase diagram of 2D WTe_2

Figure 2.7 shows measurements of the conductance G between adjacent contacts in M2 as a function of gate doping n_e. The figure includes schematics indicating the inferred state of the edge (red for conducting), as well as the bulk state (colored to match the phase diagram). Consider first the black trace, taken at 200 mK and $B_\perp = 0$. At low n_e, the bulk was insulating, and edge

conduction dominated, albeit with large mesoscopic fluctuations. For $n_e > 2\times10^{12}$ cm^{-2}, G increased as bulk conduction began; then, once n_e exceeded n_{crit}, it increased faster as superconductivity appeared before leveling out at ~200 μS as a result of contact resistance. This interpretation is supported by warming to 1K (red dotted trace), which destroyed the superconductivity and so reduced G for $n_e > n_{crit}$, but enhanced the edge conduction at low n_e toward the ideal value of $e^2/h = 39$ μS. A perpendicular field $B_\perp$ of 50 mT (green trace) also destroyed the superconductivity, causing the conductance to fall for $n_e > n_{crit}$ but barely affecting it at lower n_e. High magnetic fields have been shown[34] to suppress edge conduction in the 2D TI state by breaking time-reversal symmetry. This effect can be clearly seen in the $B_\perp =$ 1T data (orange trace in Fig. 2.7) as G fell to zero at low n_e. Comparison of the green ($B_\perp = 0.05$ T) and orange ($B_\perp = 1$ T) traces shows that G fell by a similar amount at higher n_e, consistent with a scenario in which the edge conduction supplies a parallel contribution; this implies that helical edge states persist when $n_e > n_{crit}$ and at temperatures below T_c. The phase diagram of superconductivity to topological insulator hints the existence of BCS-like excitonic condensation. In the next chapter, I will focus on the discussion about the insulating state in the interior bulk of monolayer WTe_2

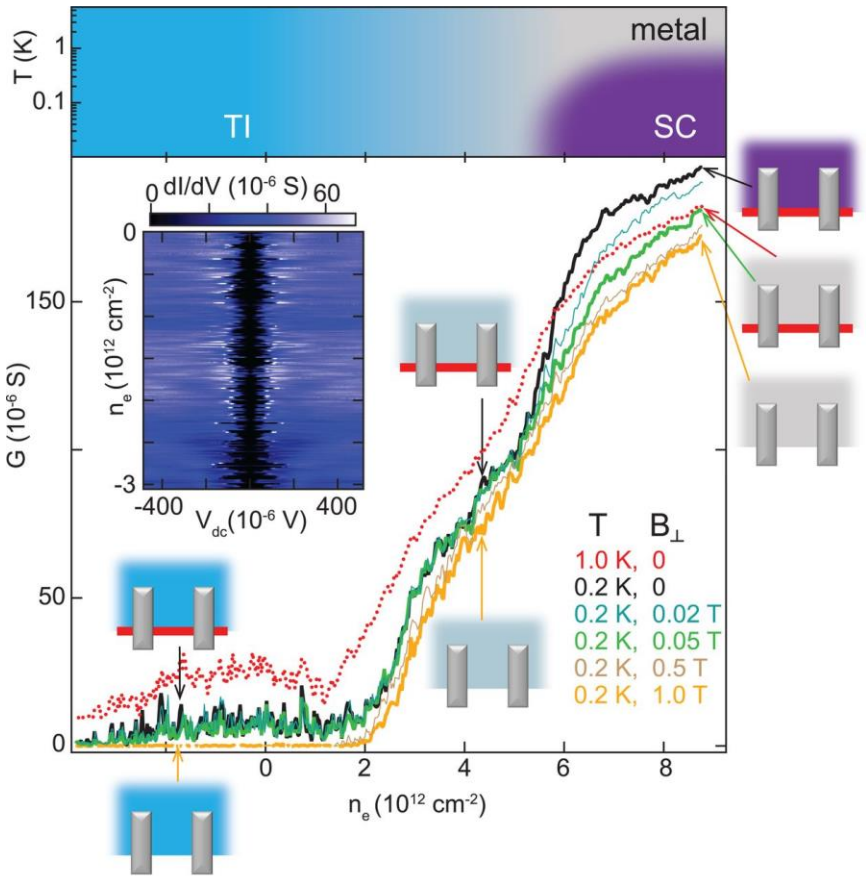

Figure 2.7 Constructed phase diagram of monolayer WTe_2 & evidence for the presence of both edge conduction and superconductivity. The main panel shows the linear conductance between two adjacent contacts versus gate doping at the temperatures and perpendicular magnetic fields noted. Schematics indicate the state of edge and bulk conduction at different points; the bulk is colored to match the phase diagram reproduced above, and red indicates a conducting edge state. Superconductivity occurs for $n_e > 5\times10^{12}$ cm^{-2} at $B = 0$. Edge conduction dominates for $n_e < 2\times10^{12}$ cm^{-2} but appears to be present at all values of n_e. Inset: Color-scale plot of different conductance versus dc voltage bias and doping level, revealing a gap of ~100 μeV that fluctuates rapidly as a function of doping level.

Chapter 3. Equilibrium excitons and exciton condensation in 1L WTe_2

We have shown in Chapter 2 that a single monolayer of the layered semimetal WTe_2 behaves as a two-dimensional topological insulator with helical conducting edge modes. These edge modes surround a bulk state that becomes insulating at low temperatures and superconducting when electrostatically doped. Here, we present evidence that this bulk state has a very unusual nature, containing quasiparticles of electrons and holes bound by Coulomb attraction – excitons – that spontaneously form in thermal equilibrium. On cooling from room temperature to 100 K the conductivity develops a sharp, V-shaped dependence on electrostatic doping, while the chemical potential develops a ~43 meV step at the neutral point. These features are much sharper than is possible in an independent-electron picture, but they can be largely accounted for by positing that some of the electrons and holes are paired in equilibrium. Our first principles calculations show that the exciton binding energy is larger than 100 meV and the radius as small as 4 nm, explaining their formation at high temperature and doping levels. Below 100 K more strongly insulating behavior is seen, suggesting that a charge-ordered state forms. The observed absence of charge density waves in this state appears surprising within an excitonic insulator picture, but we show that it can be explained by the symmetries of the exciton wave function. Monolayer WTe_2 therefore presents an exceptional combination of topological properties and strong correlations over a wide temperature range.

In this chapter, I present exitonic condensation studies of monolayer WTe_2, reproducing the discussion and results in work submitted, Sun, B. *et al.,* "Evidence for equilibrium excitons and exciton condensation in monolayer WTe_2".

3.1 Taking a second look at monolayer WTe_2

We have established that an exfoliated WTe_2 monolayer behaves[28,34,37] as a two-dimensional topological insulator, exhibiting helical conducting edge modes localized to its edges. These edge modes can coexist with an interior bulk that is either insulating or superconducting when electrostatically doped[39,40]. To better understand this behavior in the bulk, let us take a second look at the 1T' structure of monolayer WTe_2 (Fig. 3.1a). Its bands are spin degenerate due to inversion symmetry, and near the Fermi energy, E_F, there is a valence (v) band maximum at Γ flanked by two conduction (c) band minima located at $k_x = \pm k_\Lambda$. Some tunneling spectroscopy measurements[35], angle-resolved photoemission[35,45], and density functional theory (DFT) calculations[33,35,45,46] point to a positive band gap, E_g, of the order of the 50 meV, while others suggest overlapping bands[28,47]. Noting that in the photoemission spectra the v and c band photoemission features are broad enough that they overlap at least somewhat, we use thick lines in the sketch to signify this uncertainty in E_g.

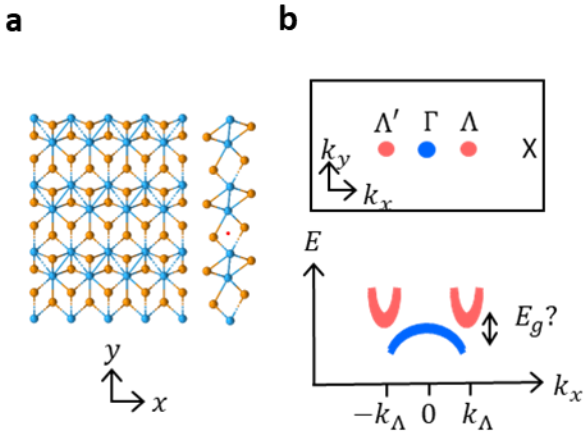

Figure 3.1 (a) 1T' structure of monolayer WTe_2. The x-axis is taken to be along the zigzag W chains. (b) Schematic Brillouin zone (above) and bands near E_F (below).

This band structure immediately suggests the possibility that exciton could occur in equilibrium in monolayer WTe_2, and therefore that the insulating state might not be a simple band insulator[48–51]. In the following sections, I will discuss the behavior of the conductivity (Sections 3.2 & 3.3) and the electron chemical potential (Section 3.4) in the interior bulk of monolayer WTe_2, and how even well above 100 K. This behavior cannot be reconciled with independent particle picture (Section 3.5). This strongly indicates the presence of excitons in the equilibrium state, a conclusion supported by our first-principles calculations of exciton dispersion and Bohr radius (Section 3.6). The insulating behavior below 100 K suggests a charge-ordered state, but while in an excitonic insulator one would normally expect charge density waves, no signs of which are seen in scanning tunneling microscopy or Raman spectroscopy. To explain this, we show that the entanglement of spin, orbital, and valley degrees of freedom hides the charge order, as the contributions to the density wave paired through time reversal cancel out.

3.2 Bulk conduction measurements on monolayer WTe_2

In this section, we study devices made from exfoliated monolayer WTe_2 flakes with platinum contacts, encapsulated by hBN, with graphite gates either above or below. To study the sheet conductivity while excluding edge conduction, we used the approach/device geometry illustrated in Fig. 3.2. As indicated in the insets, a bias V is applied to one contact and the current I flowing to ground through an opposite contact is measured. When the intervening side contacts are grounded this current must flow through the bulk. The edge current, which produces the plateau at low V_g, is thereby eliminated and the "partial conductance" $G_p \equiv I/V$ reflects the sheet conductivity, σ, via $G_p^{-1} \approx \beta/\sigma + R_c$, where β is a geometrical factor considerably larger than one and R_c is the contact resistance.

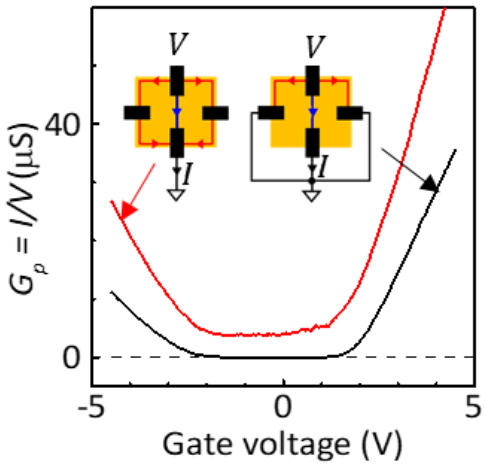

Figure 3.2 Technique used to exclude edge conduction: with the side contacts grounded, the measured current between top and bottom contacts must flow through the interior and the edge conduction plateau disappears. These measurements are taken on device MW2 at $T = 10$ K.

Figure 3.3 shows measurements of G_p vs. n_g and temperature T, where the gate-induced areal number density n_g is inferred from the voltages applied to the graphite gate(s) and the geometric capacitances. These characteristics are not measurably dependent on applied displacement field or a magnetic field (up to 14 T), thus confirming the rejection of edge conduction which is highly sensitive to magnetic field at low temperatures[52]. (Notably, a recent paper[53] reports surprising quantum oscillations at low n_g, but we have not seen these in any device). On cooling from room temperature to 100 K, G_p vs. n_p develops a sharp "V" shape centered close to $n_g = 0$. We have seen consistent behavior across a dozen devices, though the sharpness of the V varies, probably as a result of variable sample homogeneity. As shown in the inset, for positive n_g smaller than a value $n_{ce} \approx +5 \times 10^{12}$ cm^{-2}, G_p decreases monotonically on cooling, whereas for $n_g > n_{ce}$ it initially increases. For negative n_g (hole doping), a similar but less clear-cut transition occurs around $n_{cp} \approx -10 \times 10^{12}$ cm^{-2}. As indicated in a band below the figure, these values of n_{ce} and n_{cp} are

consistent with the threshold for metallic behavior reported in previous work where it was found that the metallic state at $n_g > n_{ce}$ becomes superconducting below about 0.8 K (Section 2.5).

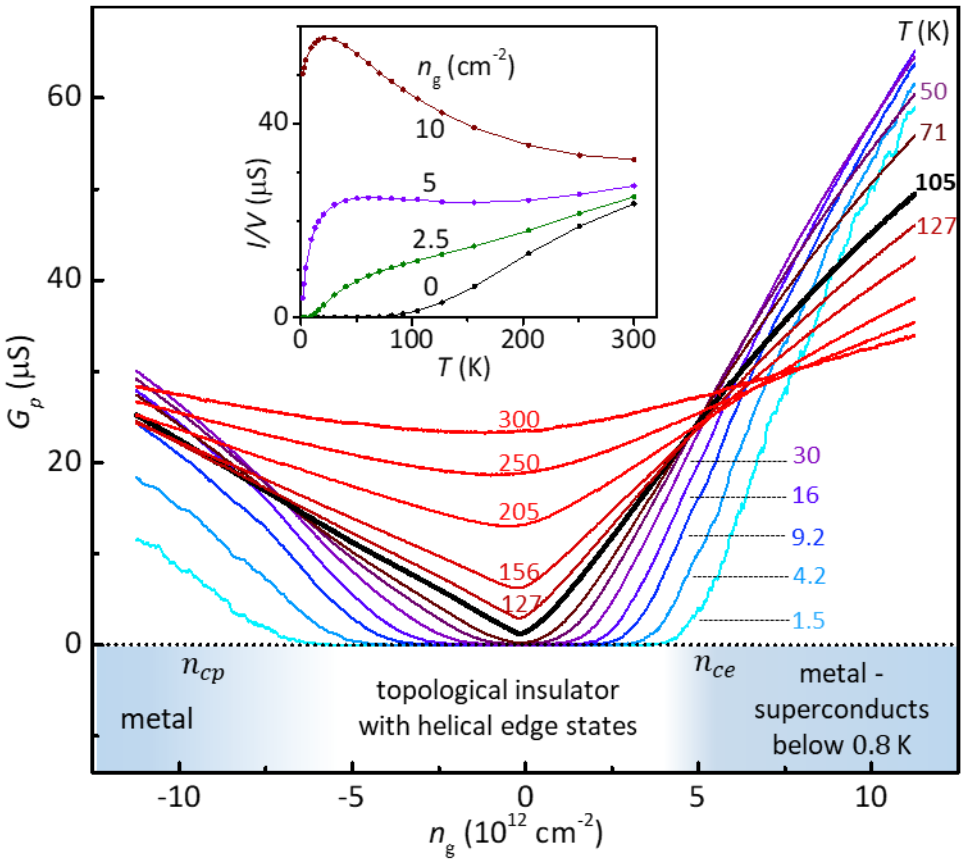

Figure 3.3 G_p vs. gate-induced density n_g at a series of temperature T on the same device. Inset: Temperature dependent at positive values of n_g. Below: regimes of insulating, metallic and superconducting behavior identified in the previous work (Section 2.6).

3.3 Local conductivity imaging and anisotropy

As T decreases below 100 K, G_p collapses over an increasingly wide range of n_g. This insulating behavior allows the edge conduction to dominate in normal geometries. We used microwave impedance microscopy[38] on devices with no top gate to confirm that this is not a contact effect, as well as to detect any internal lines of conductions (as discussed in Section 2.3.1) in the monolayer

WTe_2. We interpret these features as physical cracks in the flake which could invalidate the measurements. Fig. 3.4a is a MIM image of device MW10 at 11 K. Red dashed lines mark the edges of the monolayer WTe_2 flake, and the wiggly bright lines are cracks. Fig. 3.4b shows the MIM-derived conductivity, σ_{MIM}, measured in the center of the white dashed square. Like G_p, it collapses over a range of n_g that grows as T falls, indicated by the dotted white contour which is drawn at $\sigma_{MIM} \approx 0.1$ μS. The drop-off of G_p at low temperatures even at large n_g, evident in Fig. 3.3, can be explained by the fact that the monolayer adjacent to the metal contacts is partially screened from the gates and so is less doped and remains insulating. In addition, the contact in MW10 was aligned with the crystal axes, as determined by Raman spectroscopy (Fig. 3.4a inset), allowing us to compare conductivities along the *x*- and *y*-axes (Fig. 3.4c). We see that there is substantial gate-dependent anisotropy, with the conductivity occurring for p-doping parallel to the *x*-axis. This is consistent with the direction in which the valence band edge has a larger effective mass.

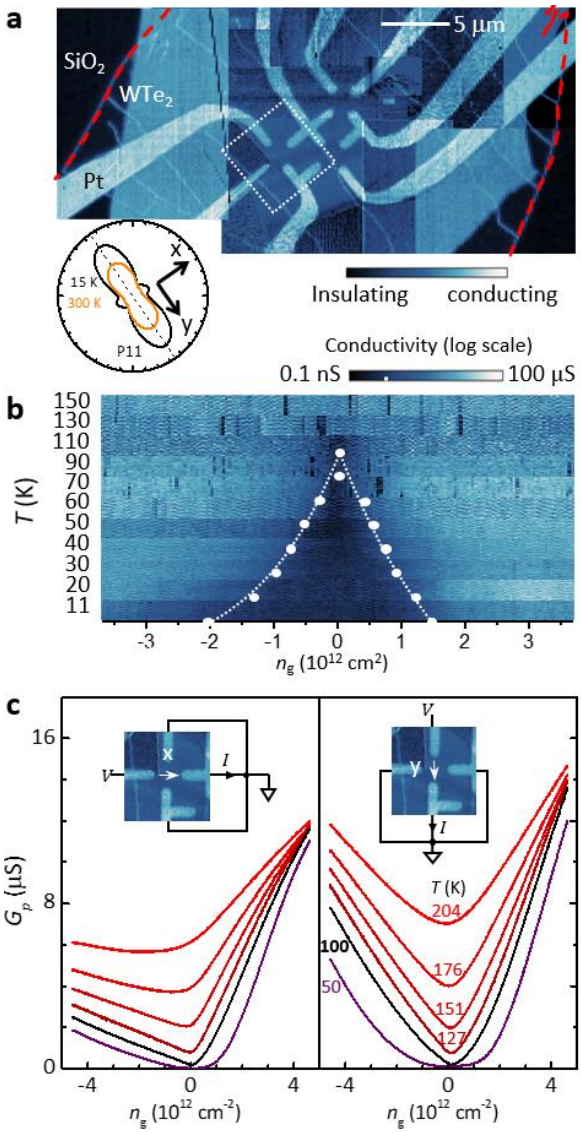

Figure 3.4 (a) Microwave impedance microscopy (MIM) image of device MW10. Here the uncalibrated imaginary MIM signal is plotted for the purpose of identifying conducting features. Multiple conducting cracks are seen running from upper left to lower right. Inset: polar plot of the Raman peak P11 (210 cm^{-1}) intensity, used to determine the crystal axes. (b) Conductivity vs. n_g and T at 2 GHz deduced from MIM measurements in the center of the white dotted square in (a). (c) Partial conductance parallel to the *x*-axis (left panel) and *y*-axis (right), measured in the white dotted square using the configuration shown in the insets.

3.3.1 Raman spectroscopy measurements

Raman spectroscopy measurement (Fig. 3.5c & Fig. 3.6b-c) were performed by our collaborators in Prof. Xu's group. To perform Raman, a sample was excited at normal incidence by a 632.8 nm excitation laser in backscattering geometry. The laser power was kept below 400 μW to prevent sample degradation. The scattered light was collected and dispersed by a 1200 mm^{-1} groove density grating and detected by a cooled charge-coupled device (CCD) with an integration time of 5 minutes. BragGrate™ notch filters were used to reject Rayleigh scatter down to 5 cm^{-1}. A linear polarizer and half-wave plate (HWP) placed between the notch filter and the sample allow the detection of Raman features that are co-linear with the excitation laser. For angle dependence, the HWP is continuously rotated by 5° through a full 360° rotation.

3.3.1.1 Determination of crystal axes

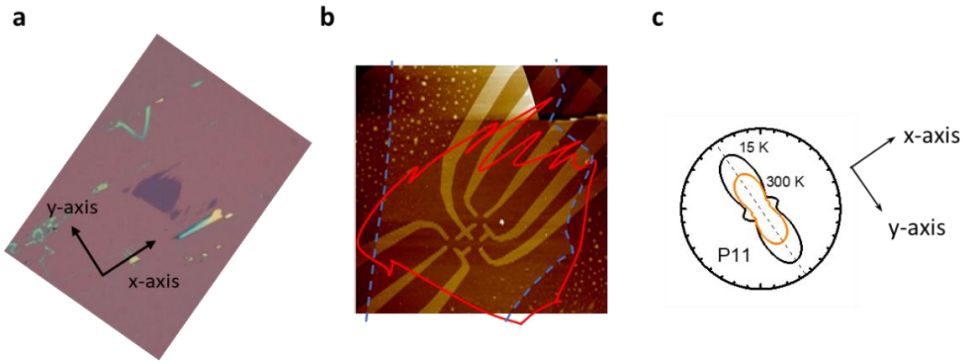

Figure 3.5 (a) Optical image of exfoliated monolayer WTe_2. The nearby bulk WTe_2 crystal and the shape of tape residue hint the identifiable crystal axes. (b) AFM scanning image of device MW10: the shape of monolayer WTe_2 is outlined in red and the bottom gate is outlined in blue. (c) Polar plot of the Raman peak P11 (210 cm^{-1}) intensity, used to determine the crystal axes.

Before assembling a device, the *x*-axis (W-chain axis) of the monolayer WTe_2 could be guessed from the orientation of nearby larger flakes and tape residue (Fig. 3.5). Polarization-

resolved Raman spectroscopy was later used on the completed device to confirm the alignment. The Raman spectrum of a WTe_2 monolayer is shown in Fig. 3.6. The peaks near 160 cm^{-1} and 210 cm^{-1} are labeled P10 and P11. In the colinear configuration described above, both are strongest along the *y*-axis in the monolayer, as seen in the Fig. 3.6, and bulk samples[54]. We therefore used several bulk WTe_2 flakes with easily identifiable crystal axes to calibrate and verify the alignment between the optical image and incident light polarization.

3.3.1.2 Search for charge density waves (CDWs)

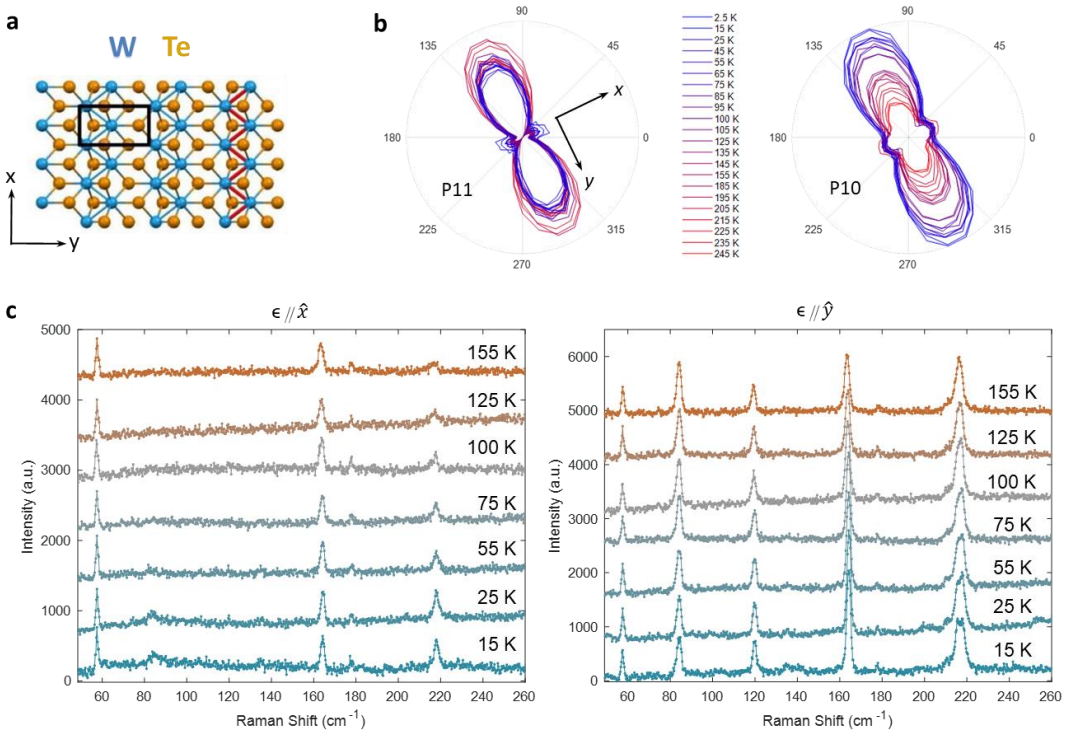

Figure 3.6 Raman Spectroscopy. (a) Structure of 1L WTe_2 seen from above; the *x*-axis is taken along the W chains. (b) Anisotropy of peaks P11 (210 cm^{-1}) and P10 (160 cm^{-1}) for colinear polarization at a series of temperature. (c) Raman intensity for polarization parallel to *x*-axis and *y*-axis at a series of temperatures, showing no distinct changes across the entire temperature range that could indicate CDW formation.

Normally, distinct changes in Raman spectrum of a layered sample provide a signature of CDW formation due to the associated symmetry change (for example, 1T-$TiSe_2$[55]). Our detailed study of the temperature dependence of the spectrum of 1L WTe_2 from room temperature down to 15 K (Fig. 3.6c), well below the appearance of the insulating state, reveals no such changes. This is consistent with the fact that no clear signs of CDWs have been observed in STM[35,42,47].

3.3.1.3 Notes on anisotropy measurements

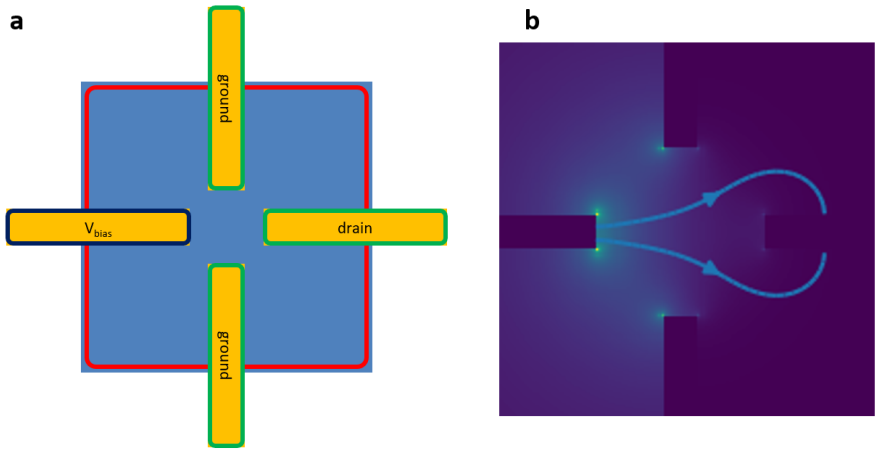

Figure 3.7 (a) Contact and boundary geometry for a current distribution simulation. Red line: boundary of 1L WTe_2 (assumed to be a uniform 2D conductor), where normal current density vanishes (and we neglect edge conduction). Blue line: equipotential at $V = V_{bias}$. Green line: equipotential at $V = 0$. (b) Current streamlines enclosing 95% of the current flowing from the left to the right contact.

Here we briefly provide more discussion of the measurements shown in Fig. 3.4c. Since the edges of monolayer WTe_2 conduct, and there are often cracks present which effectively produce internal edges, we use the "empty cross" contact pattern sketched in Fig. 3.7a to minimize the effect of such features. In devices with no top gate, such as MW10, MIM can be used to identify empty crosses where there are no cracks nearby. We then apply a bias to one contact and collect

the current to ground from the opposite contact with the other two contacts directly grounded. Most of the collected current then passes only through the central region of the cross, flowing roughly parallel to the line joining the contacts, hence probing the conductivity in this direction. We confirmed this by simulating the current flow for a uniform conducting sheet with contacts in this shape using finite-element analysis, corresponding to solving an anisotropic Laplace equation with mixed boundary conditions. Taking the conductivity to be isotropic, Fig. 3.7b shows that the simulated region encapsulating 95% of the current is indeed localized to the cross's central corridor.

3.4 Electron chemical potential measurements on monolayer WTe_2

To measure the chemical potential, we study a device including a separately contacted graphene sheet in parallel with the WTe_2 monolayer, as illustrated in Fig. 3.7a. Briefly, the WTe_2 is approximately an equipotential since it has finite conductivity and carries no current. With both the graphene and bottom gate grounded, a voltage V_g is applied to the top gate relative to the WTe_2 and the voltage V_W on the WTe_2 is adjusted to bring the graphene conductance to a minimum. This keeps the graphene neutral and maintains zero electric field beneath the WTe_2.

The electrostatic potential in the WTe_2 is thus in effect fixed to that of the graphene, so the change in V_W is due to the change in chemical potential, $\Delta\mu = -e\Delta V_W$, associated with the gate-induced charge density $-en_g = \epsilon_r\epsilon_o V_g/d$. From V_W vs. V_g we thereby obtain $\mu(n_g)$, choosing the zero of μ at each temperature for convenience. Figure 3.7b shows measurements of both μ (black) and G_p (red) vs. n_g made on the device MW12. As usual, G_p forms a sharp V as a function of n_g at 100 K. Meanwhile, μ exhibits a step at the center of the V which grows with cooling, saturating

at ~40 meV in height below about 50 K. The same behavior was seen in two devices, MW12 and MW15. (Section 3.4.1)

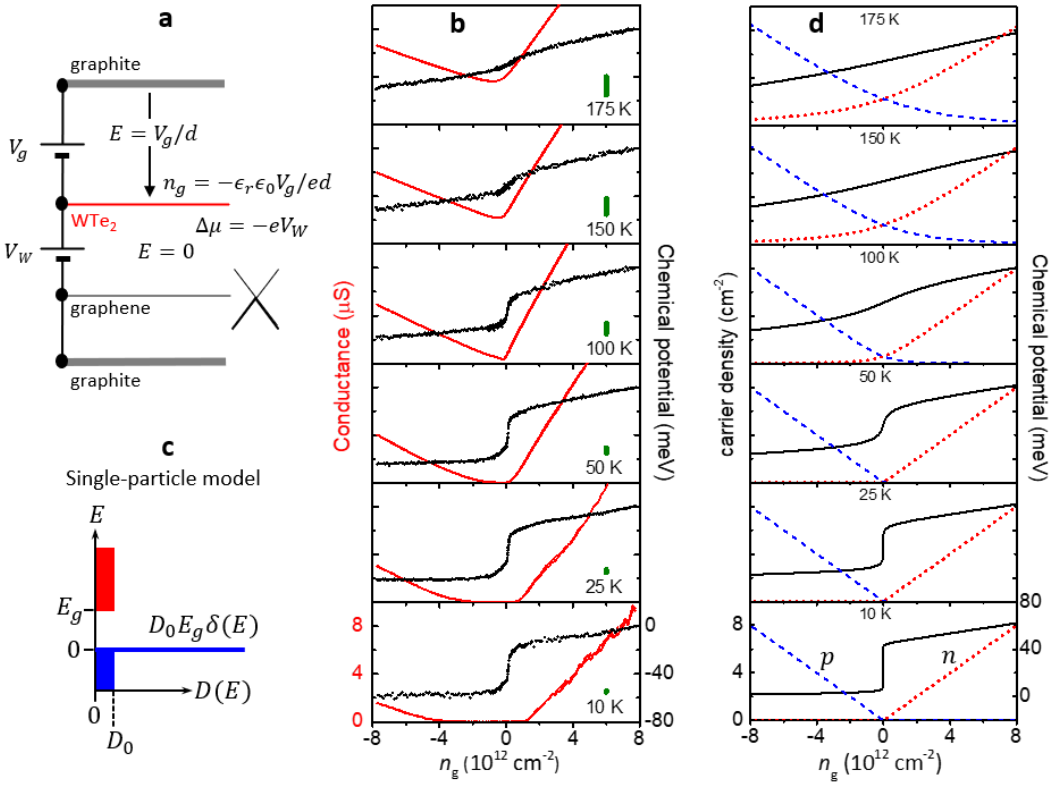

Figure 3.8 Chemical potential measurements and comparison with single particle model. (a) Schematic of the device structure used to measure the chemical potential vs. doping. In parallel with (below) the monolayer WTe_2 is a graphene sheet which is maintained at its Dirac point so that the electric field beneath the WTe_2 is zero. Doping n_g and the chemical potential μ are then obtained from the voltages as shown. The hBN dielectric between the layers is not shown. (b) Measurements of μ (black) and conductance G_p (red) vs. n_g on monolayer WTe_2 device MW12. The length of green bars indicates the thermal energy, kT. (c) Single-particle density of states $D(E)$ that reproduces the low-temperature $\mu - n_g$ behavior. (d) Calculated μ (black), electron density n (red dotted line), and hole density p (blue dashed line) using this $D(E)$ at the same temperatures as the measurements.

Let us attempt to account for our observations with a single-particle picture. In this framework, μ and n_g are related by $n_g = n_0 + \int_{-\infty}^{+\infty} D(E)\, f(E)\, dE$, where $D(E)$ is the total electron density of states, $f(E) = [1 + exp\,\{(E-\mu)/kT\}\,]^{-1}$, and n_0 is a constant. To match the variation of μ with n_g at low temperatures, $D(E)$ must have roughly the form shown in Fig. 3.8c: a constant value D_0 in the conduction band to give a uniform slope for $n_g > 0$; a gap, E_g; and a δ-function-like peak at the valence band edge ($E = 0$) to make μ flat for $n_g < 0$. In Fig. 3.8d we plot the chemical potential calculated at the same temperatures as the measurements in Fig. 3.8b, using this $D(E)$ with best-fit parameters $D_0 = 3.7 \times 10^{11}$ cm^{-2}meV^{-1} and $E_g = 43$ meV. At 150 K the step is washed out: in fact, no choice of $D(E)$ can yield a distinct step in μ whose height is less than kT as is needed to match the measurements at $T \geq 150$ K. In particular, the addition of states in the gap will only further smear the step. We also plot (dotted lines) the calculated populations of electrons in the conduction band, n, and holes in the valence band, $p = n_g - n$, to contrast their thermally smeared dependence of n_g with the sharp V-shape seen in the conductance when $T \geq$ 100 K. Clearly, the measured variations of G_p and μ with n_g cannot be reconciled with a single-particle picture.

3.4.1 Signs of excitons at 300 K

Measurements on device MW12, presented in Fig. 3.8, are compared with similar measurements on similar device MW15 in Fig. 3.9. Their behavior is consistent, except that in MW15 the step in μ is not as steep and the "V" in the conductance is more rounded. It is likely that this is a result of greater sample inhomogeneity in MW15. The measurements on MW15, however, extend to 300 K and show that some residual step is present in the chemical potential at the neutral point even at

300 K, even though the step height is much less than kT (green bar), suggesting that excitonic effects are relevant up to room temperature.

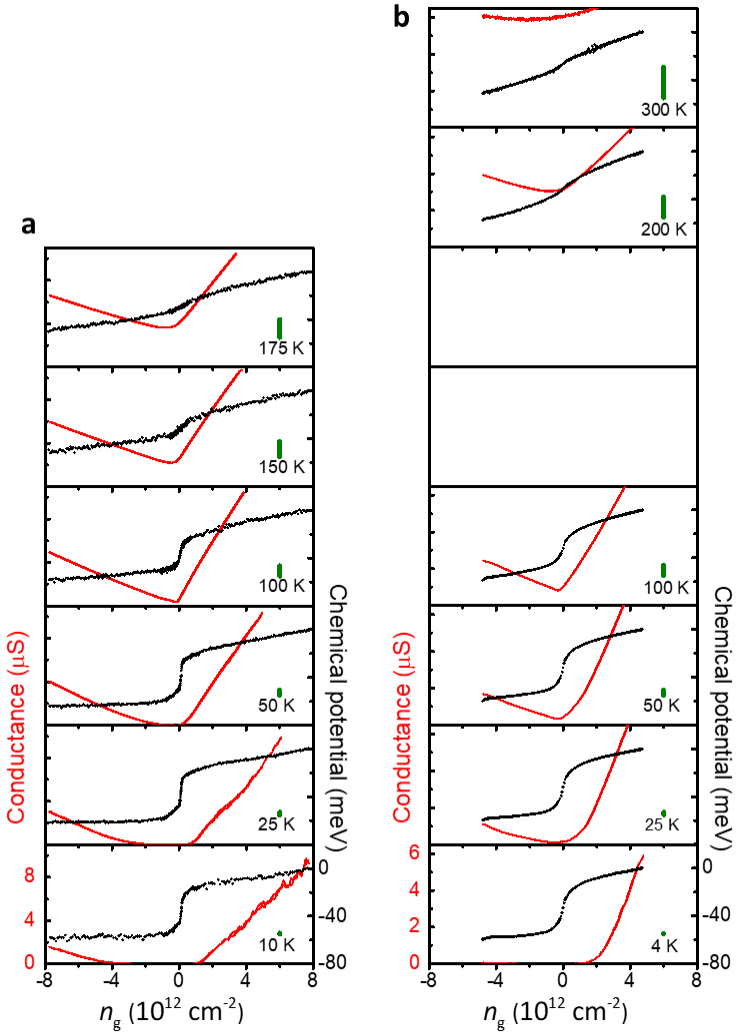

Figure 3.9 (a) Measurements of chemical potential μ (black) and conductance G_p (red) vs. gate doping n_g on 1L WTe_2 device MW12, reproduced from Fig. 3.8b. (b) Comparable measurements on device MW15. The zero of is chosen arbitrarily at each temperature.

3.4.2 Fabrications of devices to measure chemical potential μ

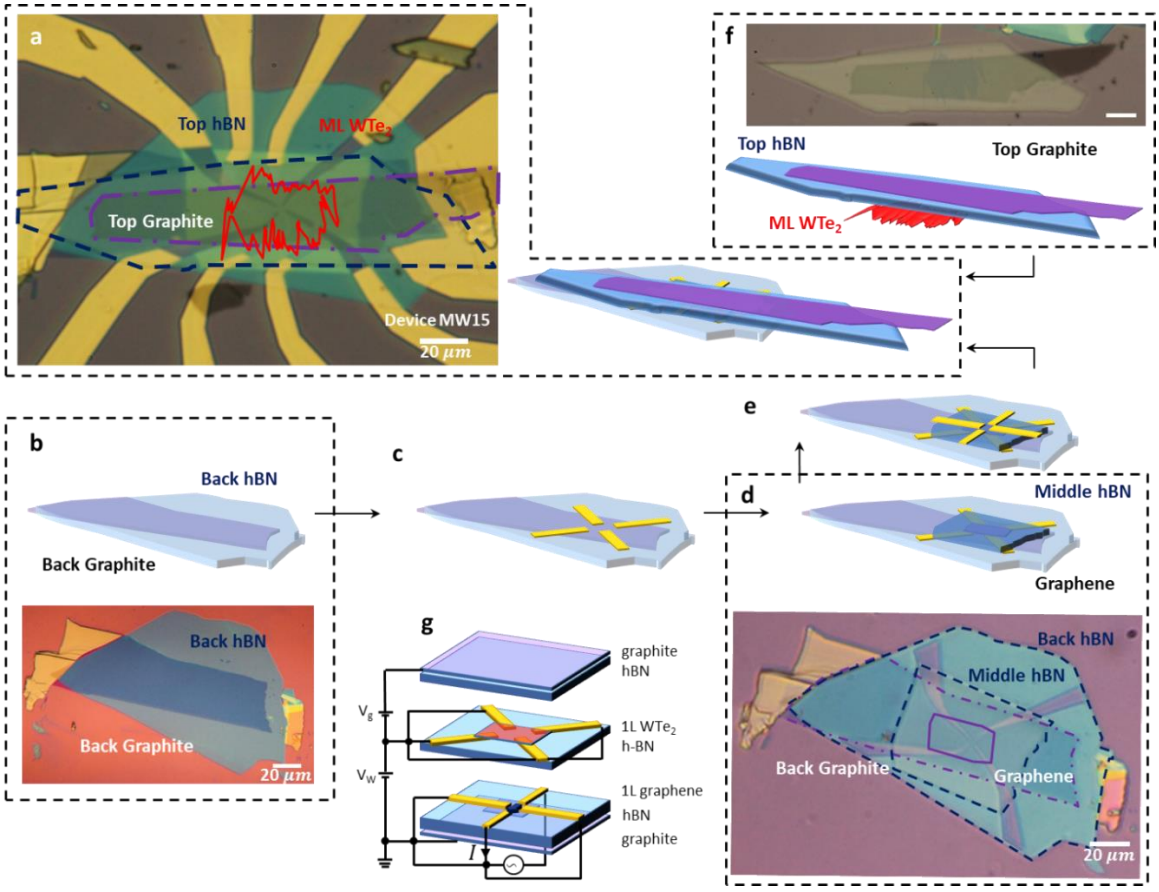

Figure 3.10 Example of sample fabrication and measurement setup: device MW15. (a) Optical image of device MW15. The monolayer WTe_2 is outlined in red. (b) Bottom hBN and graphite stack preparation. (c) Patterning of metal contacts (7 nm Pt) electrodes for graphene on bottom layer hBN. (d) Transfer of the middle layer hBN and graphene; optical image shows the transfer in progress. (e) Deposition of metal contacts electrodes (7 nm Pt) for monolayer WTe_2 on middle layer hBN. (f) Picking up top graphite/top hBN/monolayer (1L) WTe_2: the optical image shows the pick-up in progress. After transferring the top stack to the prefabricated bottom part, we end up with the device MW15 shown in (a). (g) Setup used with this device to measure μ vs n_e (See Fig. 3.8). We use a "current-focusing" geometry employing four electrodes in each layer, as shown.

To illustrate details of 1L WTe_2 as an excitonic insulator, measurements on five monolayer WTe_2 devices with somewhat different configurations are presented in this chapter. Devices MW2 and MW3 have top graphite gate and bottom SiO_2/silicon substrate gate. Device MW10 has bottom graphite gate and no top graphite gate, to allow MIM measurements to be performed. Devices MW12 and MW15 have an additional graphene layer with multiple contacts in parallel with the WTe_2 allowing chemical potential measurements. Measurements on bilayer WTe_2 devices BW4 and B2 will be discussed about in Chapter 4.

The basic fabrication process of a typical device is essentially as follows. First, graphite and hBN crystals are mechanically exfoliated onto a SiO_2/Si substrate. Using the van der Waals (vdW) transfer technique with polycarbonate/polydimethylsiloxane (PC/PDMS) "stamp"[56], the few-layer graphite bottom gate is covered by an hBN flake (bottom hBN). After dissolving the PC polymer in chloroform, the hBN/graphite is annealed at 400 ℃ for 2h for cleaning. Next, Pt metal contacts (∼7 nm) are patterned on the hBN by standard e-beam lithography and lift-off. Then, WTe_2 crystals are exfoliated in a nitrogen-filled glovebox (O_2 and H_2O concentrations below 0.5 ppm) and monolayers or bilayers are optically identified. A stack of top-gate graphite on hBN, or just hBN, is moved into the glovebox on a stamp, the WTe_2 is picked up under it, and the result is placed down on the Pt contacts on hBN. After the PC polymer is dissolved, another step of e-beam lithography, metallization (∼7 nm V, ∼70 nm Au) and lift-off is used to define wire-bonding pads and connections to the Pt contacts and the top/bottom graphite gates. For devices MW12, MW15 and B2, an extra round of e-beam lithography/metal film deposition/vdW transfer was performed to add the additional graphene layer with its own contacts. Steps in the fabrication of MW15 are shown in Fig. 3.10. The device capacitance parameters are summarized in Tables 3.1 and 3.2. These are purely geometric capacitances, but corrections of finite density of states (quantum

capacitance effects) are at the percent level in all cases. This can be deduced from the measurements shown in Fig. 3.9: the total measured variation of the chemical potential μ in the WTe_2 (~60 meV) is two orders of magnitude smaller than the applied gate voltage (~5 V).

Device	WTe_2	Top hBN (nm)	Bottom hBN (nm)	C_{tg} (10^{12}e/cm^{2}V)	C_{bg} (10^{12}e/cm^{2}V)
MW2	Monolayer	9.2	17.5	2.4	Si gate
MW3	Monolayer	11.4	14	1.94	Si gate
MW10	Monolayer	N/A	18	N/A	0.92
BW4	Bilayer	10	20.7	2.2	1.07

Table 3.1 Thickness of the top and bottom hBN and corresponding areal geometric capacitances C_{tg} and C_{bg} between adjacent conductors. The gate-induced electron density is $n_g = C_g V_g/e$, where $C_g = \epsilon_{hBN}\epsilon_0/d_{hBN}$. The effective dielectric constant of hBN is known to depend somewhat on the hBN thickness[41,57]. We used this way for some adjustment to make the critical density n_{ce} for the insulator-metal transition consistent between devices, requiring $\epsilon_{hBN} = 4$ in devices MW2, MW3, BW4 and $\epsilon_{hBN} = 3$ in device MW10.

Device	WTe_2	Top hBN (nm)	Middle hBN (nm)	Bottom hBN (nm)	C_{tg} (10^{12}e/cm^{2}V)	C_{mg} (10^{12}e/cm^{2}V)	C_{bg} (10^{12}e/cm^{2}V)
MW12	Monolayer	15	9	N/A	1.1	1.84	N/A
MW15	Monolayer	27	20	11	0.61	0.83	1.51
B2	Bilayer	25	8	N/A	0.89	2.76	N/A

Table 3.2 Thickness of the top/middle/bottom hBN and corresponding areal geometric capacitances C_{tg}, C_{mg}, C_{bg} for devices including a graphene layer for chemical potential measurements, where $C_g = \epsilon_{hBN}\epsilon_0/d_{hBN}$ and C_{mg} is between the graphene and the WTe_2.

3.4.3 Chemical potential measurement in graphene

As was done for the chemical potential in 1L WTe_2, we can also measure the $\mu(n_e) \sim T$ for graphene by swapping the roles of the graphene and WTe_2 in the same device, MW15. Tuning voltage V_G on graphene and V_{bg} on back gate graphite, we measure the conductivity of 1L WTe_2 under different combinations of (V_G, V_{bg}). The conductivity contour indicates where the potential

difference stays constant between 1L WTe_2 and graphene, as shown in Fig. 3.11a. By tracking the contour line, we see $\mu(n_e)$ for graphene. At low temperature ($T = 25$ K), this can be fitted to $E_F = \hbar v_F \sqrt{\pi n_e}$ to yield $v_F \sim 10^6$ m/s. This value is in good agreement with the literature[58].

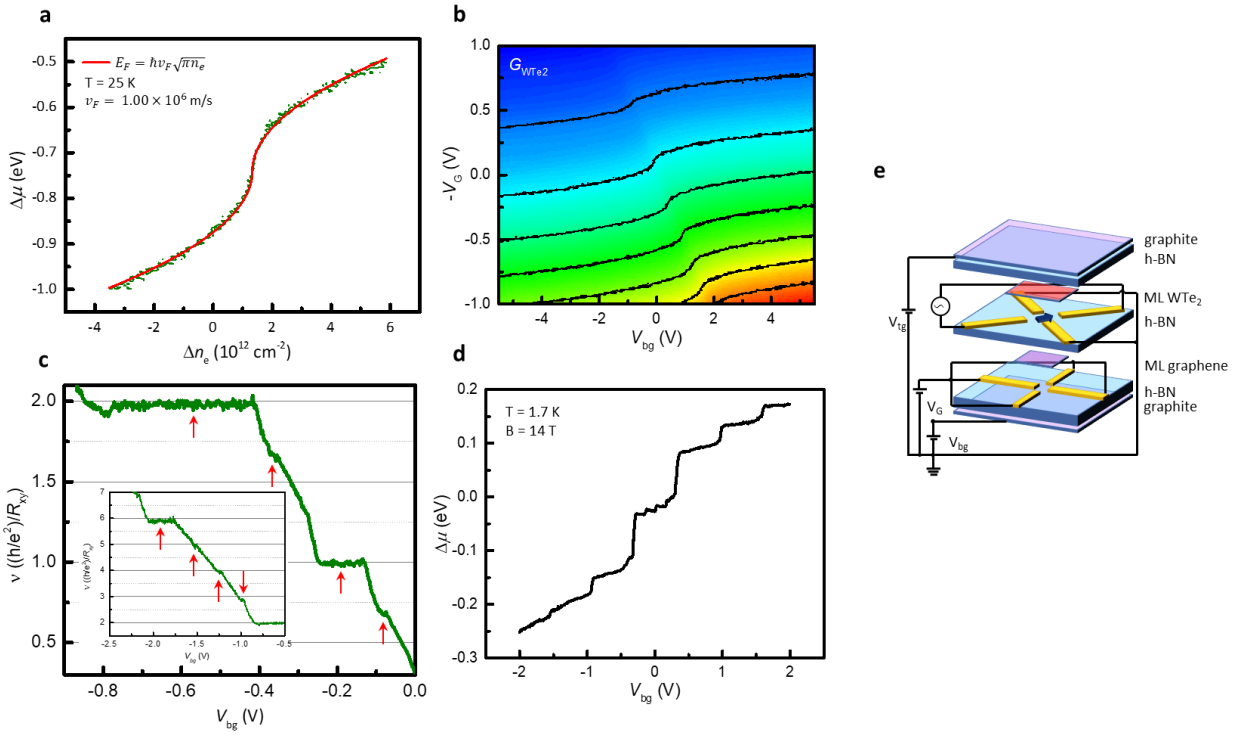

Figure 3.11 Chemical potential measurement in graphene with/without magnetic field (Device MW15) (a) Chemical potential of graphene $\mu(n_e)$ fitted with $E_F = \hbar v_f \sqrt{\pi n_e}$. (b) 2D map of conductance of 1L WTe_2 G_{WTe_2} vs. V_G and V_{bg}. (c) R_{xy} of graphene measured at $B = 14$ T, $T = 1.7$ K shows fractional Landau level at $\nu = 2/3$, 5/3 and lifted 4-fold degeneracy at $\nu = 1$. Inset: more lifted 4-fold degeneracies ($\nu = 3$, 4, 5) shown with higher back gate voltage. Landau levels are highlighted by the red arrows. (d) Chemical potential of graphene $\mu(n_e)$ under $B = 14$ T. Zero Landau level lifts 4-fold degeneracy. (e) Circuit setup to measure chemical potential of graphene.

Furthermore, because the conductivity of the interior bulk in 1L WTe_2 is not sensitive to magnetic field $B_\perp$ (Section 2.2), we can also measure graphene in the quantum Hall regime. With well-defined quantized Landau-filling factor, $\nu = N_e/N_B = n_e h/eB$, the effective dielectric

constant of hBN ϵ_{hBN} can be calibrated from $n_e = cV_{bg} = \epsilon_0\epsilon_{hBN}V_{bg}/d_{hBN}$, to yield $\epsilon_{hBN} \sim 3$. In the region of QHE, the lifted 4-fold degeneracy at zero Landau level can be clearly seen in both the transport measurements and the chemical potential measurements. At base temperature and high magnetic field (B = 14 T), fractional quantum Hall orders ν = 2/3, 5/3 are also observed. This offers an extra use of the monolayer WTe_2, as a probe of compressibility of other 2D layers in magnetic fields.

3.5 Electron-hole pairing and conductivity

The disagreement between the single-particle picture and the observed dependence of μ and G on n_g and T can be largely resolved simply by positing that some electrons and holes are bound as neutral excitons with density n_x so that the conductivity is $\sigma = \mu_e e(n - n_x) + \mu_h e(p - n_x)$, as the sum of the contributions of $n - n_x$ free electrons and $p - n_x$ free holes with respective mobilities μ_e and μ_h. In Fig. 3.12 we compare predictions based on this equation with data from Fig. 3.8 (more details will be introduced in Section 3.5.1). When $n_x = 0$ we just have $\sigma = \mu_e en + \mu_h ep$, which is thermally smeared for any choice of $D(E)$.

To illustrate this, in Fig. 3.12a we plot p and n calculated using the same $D(E)$ shown in Fig. 3.8c, at 100 K, and in Fig. 3.12b we plot the calculated σ for $n_x = 0$ (blue dotted), using a mobility ratio chosen to obtain the best match to the measured conductance at 100 K (black line). However, when n_x takes its maximal value, determined by the number of minority carriers $n_x = \min(n, p)$, then for $n_g > 0$ we have $\sigma = \mu_e e(n - p) = \mu_e en_g$ while for $n_g < 0$ we have $\sigma = \mu_h e(p - n) = -\mu_h en_g$. The result is a sharp, asymmetric "V" shape (red dashed line) which matches the measurements much better. Note that in this limit, where only the unbalanced gate-induced charge is free to move, the detailed form of $D(E)$ becomes immaterial.

As T is increased from 100 K, the conductance at $n_g = 0$ rises and sides of the "V" become shallower. This is illustrated in Fig. 3.12c, where we replot the measured conductance at 150 K (black line). The behavior remains incongruous with the single-particle model ($n_x = 0$, blue dotted), and is more similar to the calculation for the case of maximal n_x with slightly decreased mobilities (red dashed). However, there is now a discrepancy in the form of a vertical shift, equivalent to an extra gate-independent contribution to the conductance. The vertical shift cannot be accounted for by varying n_x: to illustrate this we also plot (green dash-dotted) the result of allowing n_x to vary with gate voltage according to a chemical equilibrium condition, $n_x = K(n - n_x)(p - n_x)$, where K is an equilibrium constant. It also cannot be reproduced by using a single-electron spectrum, e.g. with overlapping bands. A more sophisticated treatment of the correlated-electron system may therefore be needed to understand this aspect of the behavior (Section 3.6).

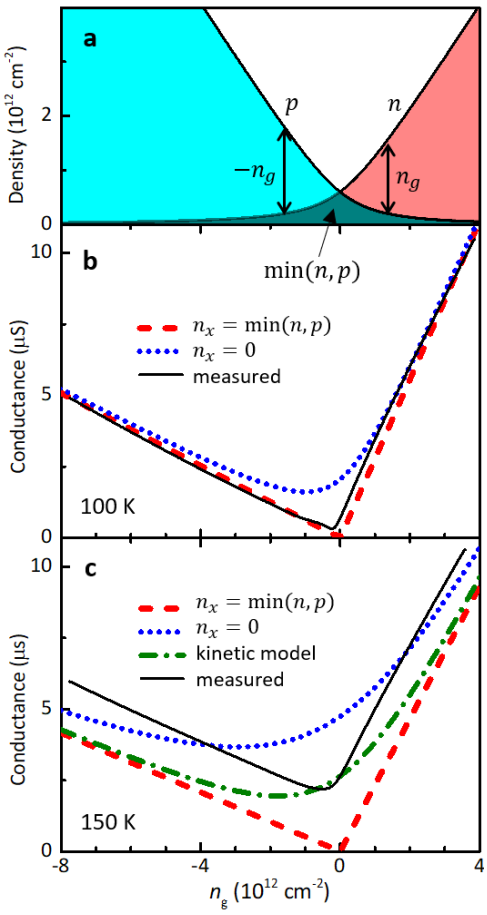

Figure 3.12 Electron-hole pairing and conductivity. (a) Total electron (n) and hole (p) densities calculated for $T = 100$ K using the single-particle density of states $D(E)$ shown in Fig. 3.8c. Here $n - p = n_g$ and the shaded region labeled $\min(n, p)$ is the maximum possible density n_x of noninteracting equilibrium excitons. (b) Measured conductance of device MW12 (black, solid line) at 100 K compared with calculated conductance for $n_x = \min(n, p)$ (red, dashed line) and for no excitons, $n_x = 0$ (blue, dotted line). (c) Same at 150 K. The additional green dash-dotted line is obtained by allowing n_x to vary in a kinetic equilibrium (discussed further in Section 3.5.1).

3.5.1 Notes on modeling the "V": mobility, band overlap, and chemical equilibrium

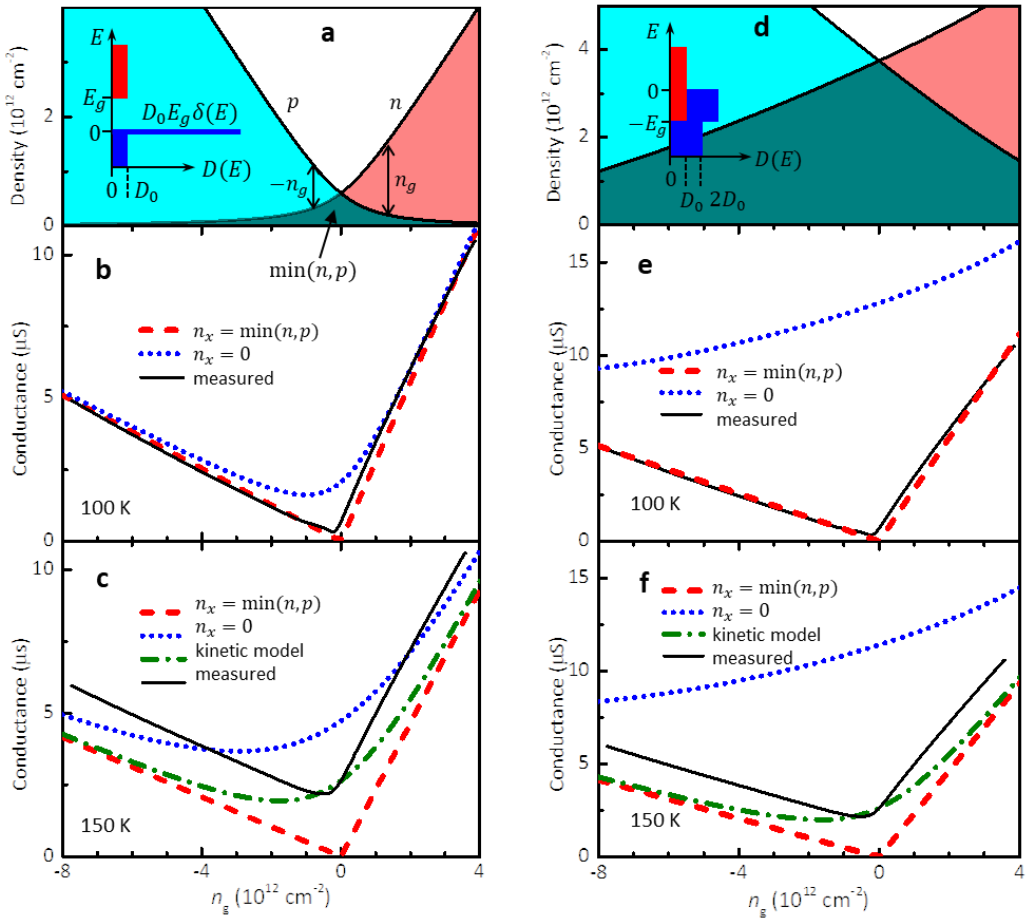

Figure 3.13 (a-c) Same as Fig. 3.11, using the gapped density of states shown in Fig. 3.8 and in the inset to (a). (d-f) Corresponding graphs using overlapped bands, as shown in the inset to (d).

Mobility. In our argument that electron-hole pairing helps explain the sharp "V", we compared the conductance data at 100 K (black trace in Fig. 3.12b) with the simple model where all minority carriers are bound, $n_x = \min(n,p)$ (red dashed trace). Then, (neglecting contact resistance R_c because G_p is small near zero doping), $G_p = \beta^{-1}\sigma = \beta^{-1}\mu_e e n_g$ for $n_g > 0$ and $G_p = -\beta^{-1}\mu_h e n_g$ for $n_g < 0$. Since the geometric factor β is unknown, we cannot determine the absolute mobilities accurately. In addition, we know the conductivity is anisotropic but we do not

know the orientation of the current relative to the axis in this device. This is unimportant, however, as our objective is simply understanding the linear "V" shape. We therefore treat $\beta^{-1}e\mu_e$ and $\beta^{-1}e\mu_h$ as parameters to achieve the best fit at each temperature; their values are unimportant but for completeness at 100 K they are $\beta^{-1}e\mu_e = 2.72 \times 10^{-12}$ μS·cm^2 and $\beta^{-1}e\mu_h = 0.64 \times 10^{-12}$ μS·cm^2; at 150 K they are $\beta^{-1}e\mu_e = 2.33 \times 10^{-12}$ μS·cm^2 and $\beta^{-1}e\mu_h = 0.52 \times 10^{-12}$ μS·cm^2.

Effect of overlapping bands. The blue dotted lines in Figs. 3.12b and c are plots of $\sigma = \mu_e n + \mu_h p$, where $n = \int_{-\infty}^{+\infty} D_c(E) f(E) dE$ and $p = \int_{-\infty}^{+\infty} D_v(E)(1 - f(E)) dE$ calculated using the gapped single particle spectrum shown in the left inset taking $E_g =$ +43 meV. To illustrate the effect of modifying $D(E)$, in Figs. 3.13d-f we show the result of doing the same calculations but with the *c* and *v* bands overlapping, i.e., with a negative gap $E_g = -40$ meV, as shown in the right inset. Here we have no δ-function at the *v* band edge and set $D_v/D_c = 1/2$ simply because $n_{ce}/n_{cp} \sim 2$. Although n and p are now much larger (Fig. 3.13d), and without excitons the model conductance varies smoothly with n_g (Fig. 3.13e) at odds with the data, if we assume again that $n_x = \min(n, p)$ then naturally we get the same "V" shape, matching the data at 100 K (red dashed), as when using the gapped spectrum.

Chemical equilibrium considerations. As mentioned in the previous section, one may also ask whether the observed behavior above 100 K could be explained by a variation of the exciton density with n_g. To make it clear that this is not feasible, we consider a variation based on simple chemical equilibrium between the excitons and free particles, i.e.,

$$n_x = K(n - n_x)(p - n_x),$$

where K is an equilibrium constant[59]. For simplicity we assume K is independent of n_g for a given temperature. Solving for n_x gives

$$n_x = \frac{1}{2}\left[n + p + \frac{1}{K} - \sqrt{\left(n + p + \frac{1}{K}\right)^2 - 4np}\right].$$

The green dash-dotted lines in Fig. 3.13c and Fig. 3.13f are plots of $\sigma = \mu_e(n - n_x) + \mu_h(p - n_x)$ using the above expression for n_x with K chosen to match the measured conductance at $n_g = 0$ and using the same $\beta^{-1}\mu_{e,h}$ values as before. The agreement with the data remains poor, irrespective of the single-particle spectrum. The chemical equilibrium condition does not prevent thermal smearing, and also it causes to n_x to approach $\min(n, p)$ as $|n_g|$ increases, making the calculated conductance too small at high gate voltages.

3.6 Calculated exciton properties

Excitons that persist in equilibrium at 100 K and at doping levels above 10^{12} cm^{-2} must have binding energy much larger than the thermal energy of $\sim$10 meV and small size to survive screening by free charges. To see if this is plausible, our collaborator, Massimo's group, solved the exciton (Bethe-Salpeter) equation of motion from first principles, building on the DFT band structure (Fig. 3.14a) and including spin-orbit effects in a non-perturbative way (Section 3.6.2). The resulting excitation energy vs. momentum $\boldsymbol{q}$ is shown in Fig. 3.14b. Since the binding energy only weakly depends on E_g because the gap is indirect[9,16], and the value of E_g is uncertain, the DFT hybrid functional is tuned to make E_g vanish. The dielectric function was evaluated in the random phase approximation, and the uncertainty induced by the numerical discretization of $\boldsymbol{k}$ space is shown by the error bars. The excitation energy is negative for all $\boldsymbol{q}$, ranging from -100 meV for direct excitons at $q = 0$ to a minimum of -330 meV for indirect excitons made of a hole at Γ and an electron at Λ. In Figs. 3.14c&d, the spatial profile of an exciton is plotted in the center-of-mass frame. The exciton radius is as small as 4 nm. This is comparable with the typical electron

separation at the critical doping, $n_{ce}^{-1/2} = 4.5$ nm, suggesting that excitons could play a role in the insulator-metal transition at n_{ce}.

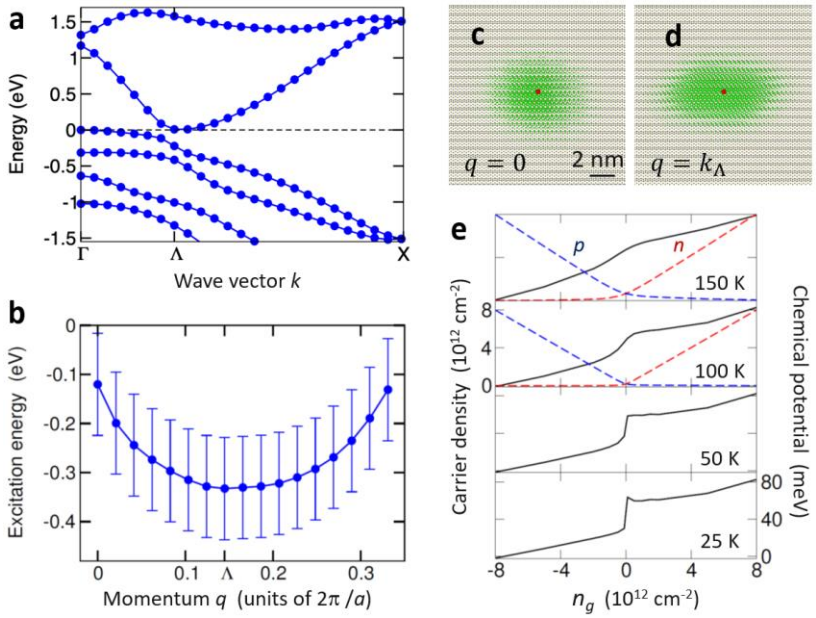

Figure 3.14 Calculated exciton properties. (a) Band structure along $\Gamma - \Lambda - X$ in Fig. 1b, obtaining from first principles (DFT-PBE0 level). Lines are guides to the eye. (b) Excitation energy of the lowest exciton vs. center-of-mass momentum $\boldsymbol{q} = (q, 0)$ along the same cut, calculated by solving the Bethe-Salpeter equation. The thick curve is a guide to the eye. The excitation energy is negative over the whole range of q, implying instability of the ground state to the spontaneous generation of excitons. Error bars are estimated by extrapolating of Brillouin zone sampling (Section 3.6.2, Fig. 3.15). (c-d) Wavefunction of the lowest exciton with $q = 0$ and $q = k_\Lambda$, respectively. The plot shows the conditional probability distribution of the electron for the hole located at the red dot. The plot in panel d is an average over three degenerate states. (e) Simulated behavior of μ vs. n_g (black solid line) for an excitonic insulator within the spinful two-band model (Section 3.6.3). The density of free electrons (red dashed) and holes (blue dashed) is computed self-consistently as the population of the *c* and *v* bands, respectively, which are renormalized by the presence of the condensate.

In interpreting the situation below 100 K in terms of an excitonic insulator, formed by condensation of the excitons, there are two problems to face.

First, at low temperatures insulating behavior sets in over a wide doping range, approaching $n_{cp} < n_g < n_{ce}$. Conventional neutral excitonic insulator theory provides no mechanism for localizing the unbalanced charge. Nevertheless, it seems possible that the Coulomb interaction, which has a long range for these doping values, could stabilize both the excitonic phase[16] and Wigner crystallization of unbound carriers, whose effective mass is enhanced by the opening of a many-body gap.

Second, the exciton condensate is naively expected to exhibit a charge density wave (CDW) with wave vector k_Λ, but CDWs are not seen in tunneling microscopy[35,42,47] and our detailed temperature-dependent Raman spectra show no evidence of any CDW transition (Section 3.3.1.2). One possible explanation is that the condensate is made of direct excitons having $\boldsymbol{q} = 0$, as predicted[48] for the T' phase of monolayer MoS_2. We have checked that this leads to no significant symmetry breaking, due to the anisotropic character of the WTe_2 band structure (Section 3.6.3). However, this state would have higher energy than a condensate made of indirect excitons with finite $\boldsymbol{q}$. A more likely possibility is that the peculiar symmetries of excitons with $q = \pm k_\Lambda$ prevent the condensate from exhibiting charge order.

From the solution of Bethe-Salpeter equation we find that the lowest-energy exciton with $q = k_\Lambda$ (or $-k_\Lambda$) is three-fold degenerate and separated by 20 meV from a nondegenerate first-excited state. This energy splitting is due to residual exchange interaction, present despite the strong spin-orbit coupling. These excitons are made of electrons and holes that populate respectively the lowest *c* and highest *v* band, with momentum $\boldsymbol{k}$ lying the ΓΛ line. Along this high-symmetry line, both *c* and *v* Bloch spinors, each doubly degenerate, may be chosen as the eigenstates of the two-fold

screw-axis rotation, which has complex conjugated values as irreducible representations. We label these Bloch spinors as $\zeta = \pm i$ and use them to write explicitly the exciton wave functions within a minimal two-band model, which includes both spin and orbital degrees of freedom (Section 3.6.3). In addition to the rotational symmetry, we may classify the excitons according to their triplet- or singlet-like character, i.e., whether they respectively maximize or minimize the electron-hole spatial overlap. In fact, Bloch states labeled by ζ transform like spins polarized along the *x* axis under the two-fold rotation, even if their actual spin polarization away from Γ is zero. Specifically, the exciton wave functions that are even with respect to the screw-axis rotation are:

$$|\pm\rangle = \frac{1}{\sqrt{2}} \sum_{k_x,k_y} \psi^{\pm}(\boldsymbol{k}) \left[c_i^{\dagger}(k_x + k_\Lambda, k_y) v_i(\boldsymbol{k}) \pm c_{-i}^{\dagger}(k_x + k_\Lambda, k_y) v_{-i}(\boldsymbol{k}) \right] |0\rangle,$$

where $+/-$ stands for singlet/triplet-like symmetry, $c_\zeta^{\dagger}(\boldsymbol{k})$ [$v_\zeta(\boldsymbol{k})$] creates [destroys] an electron of momentum $\boldsymbol{k}$ and screw-axis symmetry ζ in the *c* [*v*] band, $|0\rangle$ is the noninteracting ground state with all *v* states filled and *c* states empty, and ψ is the exciton wave function in reciprocal space in the center-of-mass frame, which is nodeless and even in k_y (and, approximately, in k_x): $\psi(k_x, k_y) = \psi(k_x, -k_y)$.

In the excitonic insulator phase, the condensate is macroscopically occupied by excitons, hence the expectation value of the operator that creates an electron-hole pair, $\langle c_\zeta^{+} v_{\zeta'} \rangle$, has a finite magnitude, $\phi_{\zeta\zeta'}$, and an arbitrary phase, $\theta_{\zeta\zeta'}$, i.e., the complex wave function of the condensate is $\phi_{\zeta\zeta'} \exp(i\theta_{\zeta\zeta'})$ (here $\langle ... \rangle$ is the average over the many-body ground state). As excitons with $\boldsymbol{q} = (k_\Lambda, 0)$ and $(-k_\Lambda, 0)$ are degenerate, they may separately condense, hence the wave function of the condensate has two valley components of equal magnitude, whose respective phases are related by time-reversal symmetry[16]. Furthermore, both condensate and exciton wave functions share the same screw-axis and spin-like symmetries[7], as well as the same parity in $\boldsymbol{k}$ space. These

fundamental constraints relate all components of the condensate to a unique wave function magnitude, $\phi(\boldsymbol{k})$, and phase, θ. If the excitonic ground state has triplet-like symmetry, one has:

$$\left\langle c_{\zeta}^{\dagger}\left(k_x \pm k_{\Lambda}, k_y\right) v_{\zeta'}(\boldsymbol{k}) \right\rangle = \pm(-1)[\sigma_z]_{\zeta\zeta'} \exp(\pm i\theta)\, \phi^{-}(\boldsymbol{k}).$$

For the singlet-like ground state, one replaces the 2×2 Pauli matrix σ_z with the identity matrix **1**, the right-hand side of the equation then reading $\mathbf{1} \exp(\pm i\theta)\, \phi^{+}(\boldsymbol{k})$. The charge/spin density wave of the excitonic insulator is dictated by the interband contribution to the expectation value of the corresponding density operator, which is proportional to the left-hand side of the above equation. Therefore, we may assess the occurrence of charge order in the excitonic phase without actually computing $\phi^{\pm}(\boldsymbol{k})$, which is given by a gap equation[16] that depends on E_g. Indeed, ϕ only provides the intensity of the density modulation, whereas θ rigidly shifts the density wave with respect to the frame origin. After a lengthy but straightforward analytical calculation, the results are as follows.

There is no CDW with momentum $q = k_{\Lambda}$, regardless of the triplet- or singlet-like ground state. In fact, the contributions to the CDW induced by excitons that are time-reversal partners cancel out exactly, due to the entanglement of degrees of freedom: were the spin-orbit interaction negligible, these contributions would sum up instead. In brief, the charge order is hidden by the combined effect of time-reversal symmetry and spin-orbit interaction, which is ultimately related to the topological properties of WTe_2[28]. The CDW may be unveiled by breaking time reversal symmetry: practically, one may split the hole states that sustain the density wave through Zeeman coupling with the magnetic field, as the hole spin is polarized along *x* (the ζ eigenvalue reduces to the spin projection close to Γ). Finally, the ground state exhibits a spin density wave of momentum $q = k_{\Lambda}$, plus a weak charge modulation of period $q = 2k_{\Lambda}$. These feature were also found by adding an intervalley scattering term to the two-band model[51], in the absence of which different

ordered states would have been degenerate. In contrast, the hidden order we predict here is inherent to both triplet- and singlet-like symmetries of the condensate, and hence robust.

Last, we consider the behavior of μ vs. n_g. We start by putting forward the following heuristic argument. At low temperatures ($T \lesssim 50$ K), where every minority carrier is paired, for $n_g < 0$ when an electron is added to the system it pairs with a hole, reducing the addition energy by the exciton binding energy and leading to diverging compressibility and self-consistent pinning of μ (in the charge-ordered state). For $n_g > 0$, the added electron does not pair and so μ is not affected by the binding energy; the result is a step in μ at $n_g = 0$ whose height is related to the binding energy. The decrease in the height of the step for $T \gtrsim 100$ K could be because the exciton binding weakens due to screening by the free carriers.

This scenario is supported by simulating the behavior of an excitonic insulator in the presence of free charge carriers (Fig. 3.14e), with both μ and the many-body gap being computed self-consistently. Here the gap has a purely excitonic origin, as the starting noninteracting phase is a semimetal. The step in μ remains clearly visible up to 100 K, in contrast with the smeared profile of the independent-electron model (Fig. 3.8d). This is a peculiar consequence of exciton condensation, as electrons injected for $n_g > 0$ fill in the lowest *c* states blockading the formation of *e*-*h* pairs – an effect due to Pauli exclusion principle and suppressed with temperatures[60]. At even higher T and step is smeared anyway since the condensate is depopulated by thermal excitations and the excitonic gap melts. Whereas the simulation of Fig. 3.14e was done for direct excitons for the sake of illustration[48], indirect excitons will exhibit the same qualitative features.

To conclude, examination of the conductivity and thermodynamics of the monolayer topological insulator WTe_2 leads to the remarkable conclusion that neutral excitons are present in equilibrium, not only in an insulating charge-ordered state at low temperatures but also at

temperatures above 100 K when the conductivity is substantial. The fact that this binding energy is close to the apparent band gap inferred from spectroscopy suggests that the latter might be best interpreted as a many-body gap. We note that we have seen similar characteristics in bilayer WTe_2 though at lower temperatures[61] (Section 4.2.1), indicating that excitons with about five times weaker binding are also present in the bilayer. The low-temperature insulating many-body state of the monolayer, which isolates the helical edge modes in this 2D topological insulator, therefore probably has excitonic insulator character, and may compete with the superconducting state that becomes the ground state above a critical electron doping level.

3.6.1 Ground state calculations from first principles

The ground-state electronic structure within density functional theory (DFT) is obtained with a plane wave basis set, as implemented in the Quantum Espresso package[62]. We fixed a kinetic energy cutoff of 80 Ry for the wave functions and used fully relativistic norm-conserving pseudopotentials[63] to include the spin-orbit interaction. We optimized the lattice parameters and atomic positions using the PBE exchange-correlation functional, the final cell parameters being $a = 3.52$ Å and $b = 6.29$ Å. We set the cell side along z to 15 Å. We obtained the band structure using a PEB0 pseudopotential, for which we considered a small fraction of exact exchange, 2%.

3.6.2 Excitation energies and exciton wave functions from first principles

The excitation energies of excitons are calculated as well as the dispersion of the lowest-energy exciton within the framework of many-body perturbation theory[64–66], by solving the Bethe-Salpeter equation through the Yambo code[67,68] and including spin-orbit interaction in a non-perturbative way[69]. We considered the PBE0 electronic structure as a starting point and calculated the static screening in the direct term within the random phase approximation, with inclusion of

local filed effects; we employed the Tamm-Dancoff approximation for the Bethe-Salpeter Hamiltonian. To avoid spurious interactions among layers, we employed a truncated Coulomb cutoff technique[70]. We obtained converged excitation energies considering respectively two valence and two conduction bands in the Bethe-Salpeter matrix, the irreducible Brillouin zone being sampled up to a $48 \times 24 \times 1$ $\boldsymbol{k}$-point grid. We extrapolated the excitation energy of the lowest excitation with momentum $\boldsymbol{q} = 0$ to the limit of a dense $\boldsymbol{k}$-point grid, as shown in Fig. 3.15.

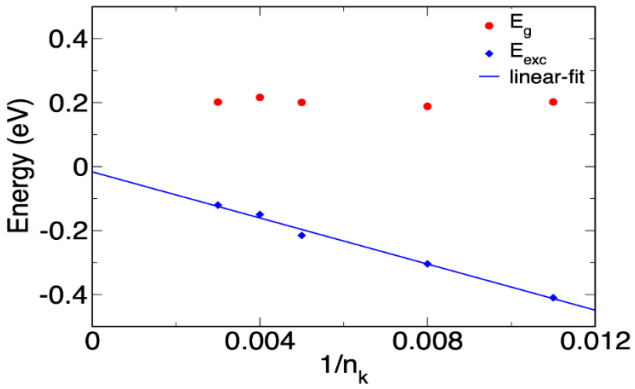

Figure 3.15 Scaling of excitation energy of lowest direct exciton with inverse number of $\boldsymbol{k}$ points, n_k. Plot of the direct band gap (E_g, red dots; not to be confused with the absolute, indirect band gap) and excitation energy of the lowest exciton with momentum $\boldsymbol{q} = 0$ (blue diamonds, E_{exc}), versus inverse number of irreducible $\boldsymbol{k}$ points, $1/n_k$. The solid line is the linear regression of the excitation energy of $1/n_k$. The difference between the energy extrapolated for $1/n_k = 0$ and the value obtained for the largest implemented sampling is 100 meV, which is the uncertainty induced by the numerical discretization of $\boldsymbol{k}$-space, shown by the error bars in Fig. 3.14b.

3.6.3 Spinful two-band model

The spinful two-band model provides the noninteracting, doubly degenerate *c* and *v* Bloch states of crystal momentum $\boldsymbol{k}$ that comply with the symmetry group of monolayer WTe_2 (the T' structure is centrosymmetric and nonsymmorphic). Within the four-dimensional spin/orbital space, the

Hamiltonian is a 4×4 Hamiltonian matrix, $H_{QSH}(\boldsymbol{k})$, whose off-diagonal elements are the spin-orbit interactions terms. Here are the orbital degree of freedom identifies the *c* and *v* Bloch states at Γ, whose energies are "inverted" with respect to the usual order of bulk semiconductors. These two states have been variously identified in the literature as a pair of orbitals having either opposite[28,48] or like[52,71] parities under spatial inversion, leading to two different forms of the spin-orbit interaction: we label the corresponding model Hamiltonians respectively as $H_{QSH,1}(\boldsymbol{k})$ and $H_{QSH,2}(\boldsymbol{k})$. We find that the charge order is hidden in the condensate of indirect excitons regardless of the model. The reason is that the screw-axis rotation (around the W atom chain direction) maintains the same form within the spin/orbital space, entangling the degrees of freedom of its eigenstates, labelled by $\zeta = \pm i$. This is pivotal to the discussion of the previous section.

In the following we detail the Hamiltonians $H_{QSH,1}(\boldsymbol{k})$ and $H_{QSH,2}(\boldsymbol{k})$. To use a notation consistent with the reference[48], throughout this section and the next (but nowhere else) we swap the *x* and *y* cartesian axes with respect to the reference frame used in the previous section. The first model, $H_{QSH,1}(\boldsymbol{k})$, is taken from references[28,48] with minor adjustments. The Hamiltonian reads:

$$H_{QSH,1}(\boldsymbol{k}) = \frac{1}{2}\left[\epsilon_u(\boldsymbol{k}) + \epsilon_g(\boldsymbol{k})\right] 1_\tau \otimes 1_\sigma + \frac{1}{2}\left[\epsilon_u(\boldsymbol{k}) - \epsilon_g(\boldsymbol{k})\right] \tau_z \otimes 1_\sigma + \hbar v_2 k_y \tau_x \otimes \sigma_x,$$

where v_2 is the spin-orbit coupling parameter, τ_x, τ_y, τ_z and σ_x, σ_y, σ_z are 2×2 Pauli matrices in orbital and spin space, respectively, and the 2×2 unit matrices are 1_τ and 1_σ. The diagonal matrix elements, $\epsilon_l(\boldsymbol{k})$ with $l = u, g$, are the band energies in the absence of spin-orbit interaction, which are inverted at Γ and cross at the points $\pm k_\Lambda$ of the ΓY line in the Brillouin zone. The energies $\epsilon_l(k_x, k_y)$ are even with respect to both k_x and k_y axes. The corresponding Bloch states transform like p_y and d_{yz} orbitals at Γ. The functional dependence of ϵ_l on $\boldsymbol{k}$ differs from the effective-mass expression given in the reference[48], but its precise form is irrelevant to the discussion of the previous section, solely based on symmetry arguments. We discard the off-

diagonal spin-orbit term linear in σ_y considered in the reference[48], the total Hamiltonian being now even in k_x, $H_{QSH,1}(k_x, k_y) = H_{QSH,1}(-k_x, k_y)$. This choice agrees with the evidence that the spin-orbit field lies in the *xz* plane[52]. Furthermore, we find that the spin-orbit term proportional to σ_x provides a good matching with the strongly anisotropic DFT bands, as we checked through comparison with our own first-principles calculations. In the spin/orbital space, the inversion operator reads $\boldsymbol{I} = -\tau_z \otimes 1_\sigma$ and the screw-axis rotation around the y axis is $\boldsymbol{C}_{2y} = i\tau_z \otimes \sigma_y \exp(ik_y a/2)$, with a being the lattice constant in the direction parallel to the W chains.

The second model, $H_{QSH,2}(\boldsymbol{k})$, is taken from our previous work[52] and builds on the four-band tight-binding Hamiltonian proposed in the reference[71] to improve the matching between model and DFT bands. The *c* and *v* orbital states are Wannier functions, respectively an antibonding combination of $d_{x^2-y^2}$-type orbitals localized on W atoms [energy $\epsilon_W(\boldsymbol{k})$] and a bonding superposition of p_y-type orbitals localized on Te atoms [energy $\epsilon_{Te}(\boldsymbol{k})$]. These Wannier functions have the same parities under inversion but opposite parities under the screw axis two-fold rotation, like the Bloch states at Γ of our own DFT calculations. The Hamiltonian is:

$$H_{QSH,2}(\boldsymbol{k}) = \frac{1}{2}[\epsilon_W(\boldsymbol{k}) + \epsilon_{Te}(\boldsymbol{k})]1_\tau \otimes 1_\sigma + \frac{1}{2}[\epsilon_W(\boldsymbol{k}) - \epsilon_{Te}(\boldsymbol{k})]\tau_z \otimes 1_\sigma + \lambda_{SO}\tau_y \otimes \sigma_x \,,$$

where $\lambda_{SO} > 0$ is the spin-orbit coupling parameter, which is independent from $\boldsymbol{k}$. For the sake of simplicity, here we have neglected the spin-orbit term proportional to σ_z proposed by the reference[52]. Within the envelop function approximation, the band energies $\epsilon_W(\boldsymbol{k})$ and $\epsilon_{Te}(\boldsymbol{k})$ are provided by the tight-binding calculation of the reference[71] and are even with respect to both k_x and k_y axes. The inversion operator now reads $\boldsymbol{I} = 1_\tau \otimes 1_\sigma$ whereas the screw-axis rotation around the *x* axis is again $\boldsymbol{C}_{2y} = i\tau_z \otimes \sigma_y \exp(ik_y a/2)$.

3.6.4 Eigenstates of the screw-axis rotation

The eigenvectors of $H_{QSH,1}(\boldsymbol{k})$ that were explicitly given in the reference[48] are spin polarized along the direction perpendicular to the W atom chains. Here we use the notation $|\boldsymbol{k},\lambda\rangle$ to identify these eigenvectors, which belong to either the *c* or *v* band and have spin polarization $\lambda = \uparrow,\downarrow$. In the Section 3.6, we introduced an alternative, equally legitimate set of eigenvectors, which are simultaneous eigenstates of $H_{QSH,1}(\boldsymbol{k})$ and $\boldsymbol{C}_{2y}$ (the latter with eigenvalues $\zeta = \pm i$), by applying a unitary rotation of the basis for any wave vector $\boldsymbol{k}$. Explicitly, $|\boldsymbol{k},\zeta = -i\rangle = \frac{i|\boldsymbol{k},\uparrow\rangle + |\boldsymbol{k},\downarrow\rangle}{\sqrt{2}}$, $|\boldsymbol{k},\zeta = +i\rangle = \frac{-i|\boldsymbol{k},\uparrow\rangle + |\boldsymbol{k},\downarrow\rangle}{\sqrt{2}}$, with $\boldsymbol{C}_{2y}|\boldsymbol{k},\zeta = -i\rangle = -i\exp(ik_y a/2)\,|\boldsymbol{k},\zeta = -i\rangle$ and $\boldsymbol{C}_{2y}|\boldsymbol{k},\zeta = +i\rangle = i\exp(ik_y a/2)\,|\boldsymbol{k},\zeta = +i\rangle$, as may be checked by direct substitution. Importantly, the states $\zeta = \pm i$ are not spin polarized (except at $\boldsymbol{k} = 0$), since the spin and orbital degrees of freedom are now entangled. Note that $|\boldsymbol{k},\zeta = -i\rangle$ and $|-\boldsymbol{k},\zeta = +i\rangle$ are time-reversal mates, with $\Theta|\boldsymbol{k},\zeta = -i\rangle = i|-\boldsymbol{k},\zeta = +i\rangle$, the time-reversal operator being $\Theta = i1_\tau \otimes \sigma_y K$ (K is the complex conjugation operator).

The simultaneous eigenvectors of $H_{QSH,1}(\boldsymbol{k})$ and $\boldsymbol{C}_{2y}$ that we use to build the excitonic insulator ground state (within the envelope function approximation) are as follows. The *c* band state with $\boldsymbol{k} = (0, k_\Lambda)$ and $\zeta = +i$ is $(-1+i)/(2\sqrt{2})[-i, i, 1, 1]$; the *v* band state with $\boldsymbol{k} = 0$ and $\zeta = +i$ is (approximately) $\left(1/\sqrt{2}\right)[0, i, 0, 1]$. The states with $\zeta = -i$ as well as those with $\boldsymbol{k} = (0, -k_\Lambda)$ are obtained through time reversal and inversion transformations. Here the first and third (second and fourth) components of the four-dimensional vector, $[u_{W,\uparrow}, v_{Te,\uparrow}, u_{W,\downarrow}, v_{Te,\downarrow}]$, correspond to a spinor whose orbital part is a Wannier function localized on W(Te) atoms in the crystal unit cell.

3.6.5 Condensate of indirect excitons and charge/spin order

We assess the charge (spin) order of a permanent condensate of indirect excitons of momentum $\boldsymbol{q} = (\pm k_\Lambda, 0)$ within the multivalley framework developed in the reference[16]. This approach, in turn, relies on the scheme to decouple the equations of motion for Green functions[72]. The theory, which deals with spinless electrons, may be straightforwardly generalized to spinors labeled by the screw-axis symmetry $\zeta = \pm i$. Indeed, for any given electron and hole species ζ and ζ', the structure of the equations of motion for Green functions that govern the condensate component $\langle c_\zeta^+ \, v_{\zeta'} \rangle$ remains the same, since ζ electrons pair with ζ' holes only: as far as pairing is concerned, ζ spinors behave as if they were spinless fermions. Therefore, the $\boldsymbol{k}$-dependent spinless Bogoliubov-Valatin-like creation operator that defines the excitonic insulator ground state in equations 20 and 21 of the reference[16] is simply replicated for $\zeta = \pm i$, provided one specializes equation 21 to the present case of two valley components and chooses the condensate phases as shown in the Section 3.6. Finally, we compute the expectation value of the charge (spin) density operator over the excitonic ground state, after making the spin/orbital structure of ζ Bloch states (given in the previous section) explicit, the derivation being lengthy but straightforward. As discussed in the main text, in order to simply assess the occurrence of charge (spin) order without computing the density wave modulation intensity, it is not necessary to evaluate explicitly the coherence coefficients u_k^0 and v_k^0 that occur in equation 21 of the reference[16].

3.6.6 Condensate of direct excitons and simulation of Fig. 3.14e

We obtain the results shown in Fig. 3.14e within the spinful two-band model $H_{QSH,1}(\boldsymbol{k})$ described above, the band energies $\epsilon_l(\boldsymbol{k})$ being parametrized through comparison with our own DFT calculations ($l = u, g$). The noninteracting ground state, in the absence of spin-orbit interaction, is

taken to be a semimetal with a band overlap of 38 meV. The energy parametrization relies partly on the tight-binding model of the reference[71] (Table III therein) and partly on an ad-hoc parameters. In detail, we correct the tight-binding energies by adding the terms $2(t_l' - t_l'')\cos 2k_x + 2t_l''\cos 2|\boldsymbol{k}|$, with $t_g' = 0.149$ eV, $t_u' = 0.075$ eV (see reference[46]), $t_g'' = 0.049$ eV, and $t_u'' = 0.055$ eV. The spin-orbit parameter is $v_2 = 10^{14}$ Å$/s$, and the strength of Coulomb interaction is fixed by the two-dimensional polarizability, $\alpha_{2D} = 5.5$. In order to compute the chemical potential μ vs. charge density n_g in the many-body excitonic phase, we adapt the theory of the reference[48], which deals with a condensate of direct excitons in an intrinsic semiconductor, to the case of a doped system, by means of a fully-self consistent calculation of both the excitonic order parameter, $\Delta_X(\boldsymbol{k})$, and μ. Furthermore, we assume that the Coulomb interaction remains long ranged for any doping value, which is supported by the evidence that charge carriers localize in a wide doping interval at low T. The free carriers populating the renormalized bands of the excitonic insulator are conventionally taken as noninteracting, which is the origin of the unphysical behavior of μ for small, positive values of n_g at $T = 25$ K ($d\mu/dn_g$ is negative close to the axis origin in Fig. 3.14e)

We have checked that the observable effects related to the breaking of inversion symmetry, due to the condensation of excitons with $\boldsymbol{q} = 0$, are negligible for WTe_2, contrary to the case of 1T'-MoS_2. This is related to the limited extent of the excitonic order parameter, $\Delta_X(\boldsymbol{k})$, along the Brillouin zone direction perpendicular to the ΓΛ line, which is in turn caused by the strong anisotropy of the noninteracting *c* and *v* bands close to Λ (compare Fig. 3.14 with Fig. 3.16). In particular, the real part of $\Delta_X(\boldsymbol{k})$ is negligible; hence the *c* and *v* bands, renormalized by electron-hole pairing, each remain doubly degenerate.

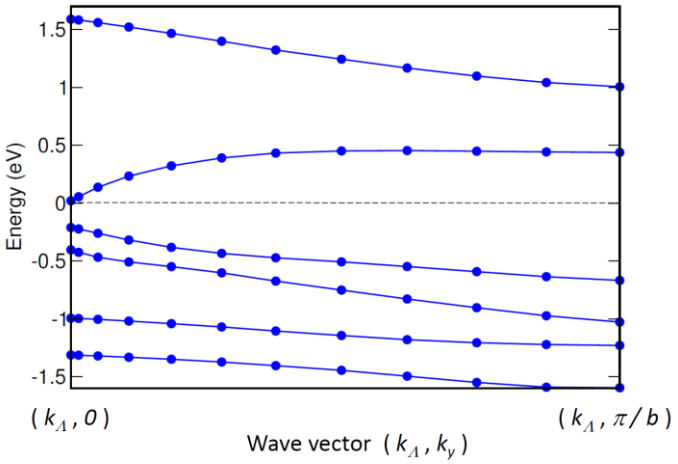

Figure 3.16 Band dispersion perpendicular to ΓΛ cut of the Brillouin zone. Calculated bands from first principles (DFT-PEB0 level) along the cut of the Brillouin zone parallel to Γ*Y* and intersecting the Λ point. The plot is a companion to Fig. 3.14 which is along the Γ*X* cut.

Chapter 4. 2L WTe_2 – Ferroelectric switching and potential excitonic insulator candidate

A ferroelectric is a material with a polar structure whose polarity can be reversed (switched) by applying an electric field[73,74]. In metals, itinerant electrons screen electrostatic forces between ions, which explains in part why polar metals are very rare[75–79]. Screening also excludes penetrating external electric fields in such a metal, apparently ruling out the possibility of ferroelectric switching. In principle, however, a thin enough polar metal could be sufficiently penetrated by an electric field to have its polarity switched. It is shown that the topological semimetal WTe_2 provide an embodiment of this principle. Although monolayer WTe_2 is centrosymmetric and thus non-polar, the stacked structure is polar even in the bilayer. Indeed, we found that two- or three-layer WTe_2 exhibits spontaneous out-of-plane electric polarization that can be switched using gate electrodes (Section 4.1.1). This polarization can be directly detected and quantified using graphene as an electric field sensor[80] (Section 4.1.2). Further theoretical work predicted an out-of-plane electric polarization that reverses on a shift of stacking order, which modifies the crystal symmetry (Section 4.1.3). This structural origin of the ferroelectricity agrees with our observations that the temperature at which polarization vanishes exceeds 350 K, a property which is retained even when the WTe_2 is sandwiched between graphene layers. This demonstrates a robustness suitable for applications in combination with other two-dimensional materials.

As discussed in the Chapter 2, bilayer WTe_2 develops a strong V_g dependence with a sharp minimum near $V_g = 0$, while becoming insulating at low temperature. Inspired by what was found in monolayer WTe_2, we measured the chemical potential and found a similar behavior of $\mu(n_e)$ in the bilayer WTe_2 (Section 4.2.1). We also measured transport characteristics of bilayer WTe_2 on directly on substrates of $SrTiO_3$, a quantum paraelectric (Section 4.2.2). Due to the dielectric

screening effect, bilayer WTe_2 becomes metallic, which hints that the insulating state is driven by electron-electron interaction.

In the first half of this chapter, I will present ferroelectricity found in bilayer WTe_2, reproducing the results and discussion from our previous work[61], and propose potential applications. In the second half of this chapter, I will introduce the evidence for bilayer WTe_2 being another potential excitonic insulator candidate.

4.1 Ferroelectricity in bilayer WTe_2

The three-dimensional 1T'-WTe_2 stacks in T_d order, which is orthorhombic and has a polar space group $Pmn2_1$[79]. It remains metallic down to three layers when undoped[81], or to a monolayer when electrostatically doped[34]. As shown in Fig. 4.1, the 1T' structure with T_d stacking contains a *y*-*z* mirror (M) plane and an *x*-*z* glide plane. Because a polar axis must be parallel to two symmetry planes, the only allowed axis is the *z*-axis which is perpendicular to the layers[79].

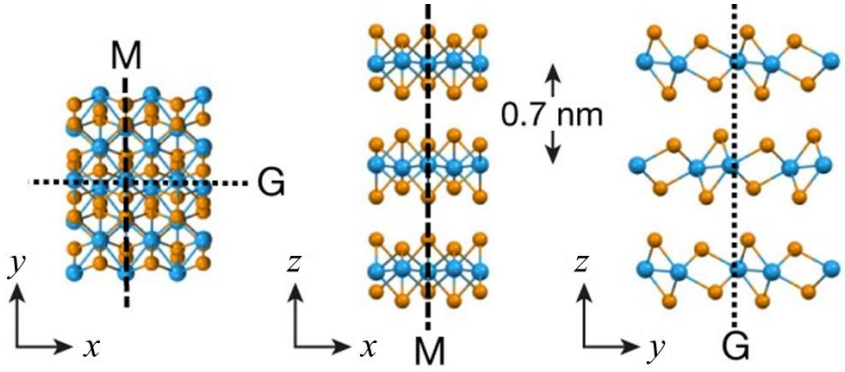

Figure 4.1 Crystal structure and symmetries of T_d WTe_2. M and G are (*y*-*z*) mirror plane and (*x*-*z*) glide plane, respectively. Orange balls, Te atoms; blue balls, W atoms.

4.1.1 Transport measurement

An electric field along the polar axis can be applied by using the device geometry indicated in the Fig. 4.2 wherein a thin WTe_2 flake contacted by Pt electrodes is sandwiched between two hBN dielectric sheets, with the thickness d_t (top hBN) and d_b (bottom hBN). Above and below the hBN are gate electrodes, to which gate voltages V_t and V_b can be applied. The average electric flux density passing upwards through the WTe_2 flake when it is grounded is defined by

$$E_\perp = \left(-\frac{V_t}{d_t} + \frac{V_b}{d_b}\right)/2$$

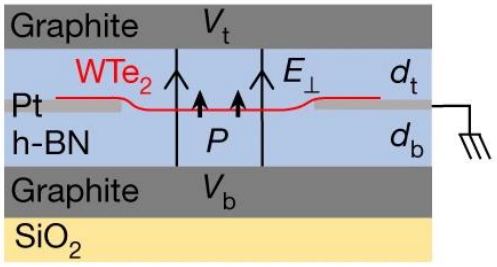

Figure 4.2 Cross-section of a device with dual graphite gates. Perpendicular electric field is applied to a thin WTe_2 flake by changing top gate voltage (V_t) and bottom gate voltage (V_b).

Measurements of four-terminal conductance G as a function of $E_\perp$ in tri-, bi- and mono-layer WTe_2 devices are shown in the Fig. 4.3. External doping of the WTe_2 flake is zero when $V_t/d_t = -V_b/d_b$. Bistability of G was only observed in trilayer and bilayer devices near $E_\perp = 0$ at all temperatures T between room temperature and 4 K. However, no bistability was observed in the monolayer device. This is consistent with monolayer WTe_2 being centrosymmetric and therefore nonpolar. This is not only evidence of ferroelectric switching in bilayer and trilayer WTe_2, but it also rules out instabilities involving charge injection into the hBN. Note that a larger field is required to switch the trilayer than the bilayer WTe_2.

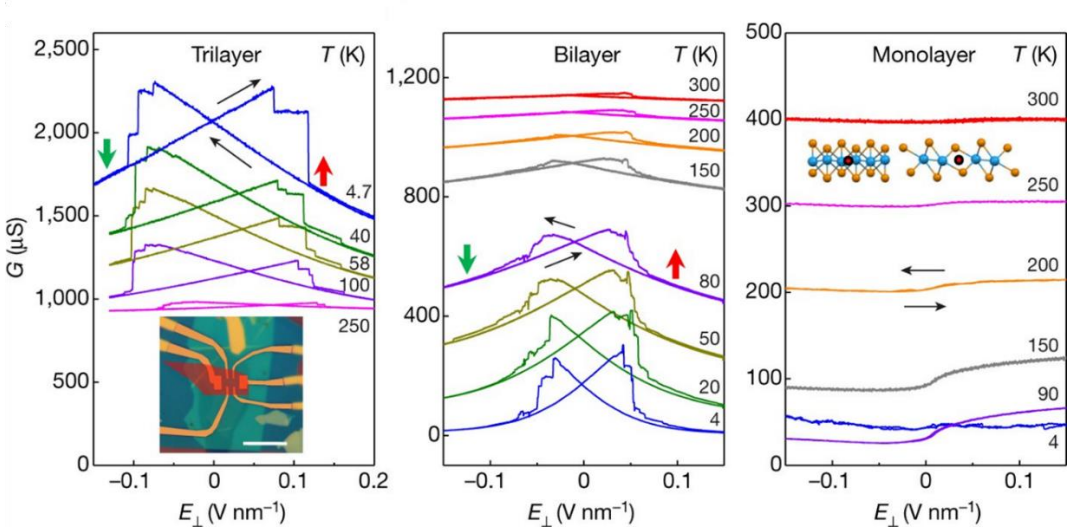

Figure 4.3 Conductance G of updoped tri-, bi- and mono-layer WTe_2 as $E_\perp$ is swept in both directions. Black arrows show sweeping direction of $E_\perp$ and green and red arrows show the direction of polarization. (Left) Bistability of trilayer WTe_2 device TW1. G of the trilayer WTe_2 increases with cooling, a metallic temperature dependence. While $E_\perp$ is swept, G shows bistability consistent with flipping of up and down electrical polarization, which occurs at all temperatures from 300 K to 4 K. Inset: microscope image of device, scale bar: 10 μm. (Middle) Bistability of bilayer WTe_2 device BW5. Though G of the undoped 2L WTe_2 shows an insulating temperature dependence, it is still bistable. (Right) The same measurement on 1L WTe_2 device MW1, showing no bistability. Insets: atomic models of 1L WTe_2 showing center of symmetry (red circles).

4.1.2 Detecting the out-of-plane polarization

The conventional methods of detecting polarization switching in insulating ferroelectrics are measurements of either P–E curves or displacement current. However, these measurements are challenging with few-layer WTe_2 since both the polarization density and device area are small. To overcome this limitation, we developed a technique using a graphene electric field sensor on top similar to the geometry we introduced to measure chemical potential in Ch. 3. Fig. 4.4 shows an optical image and schematic cross-section of one such device, BW2. The conductivity of graphene G_{gr}, which can be measured directly, is sensitive to the electric field E_t beneath it.

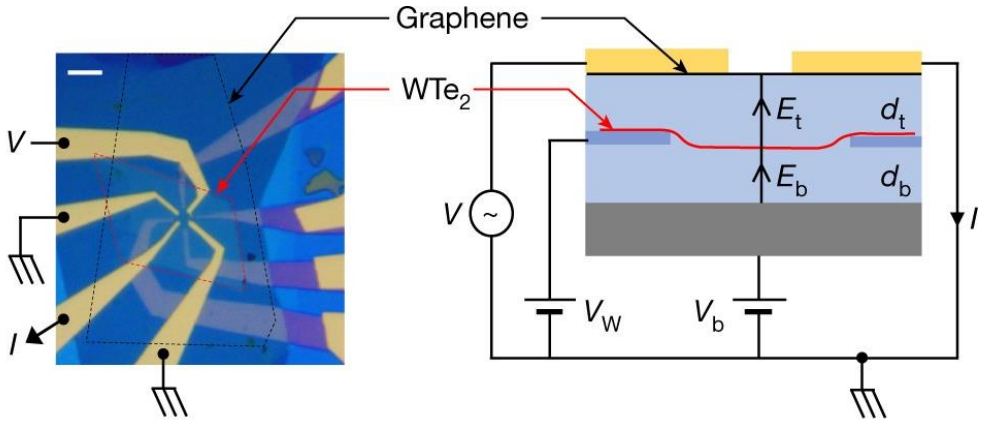

Figure 4.4 Optical image and schematic cross-section of a bilayer device BW2, scale bar: 5 μm. This device has a separately contacted graphene top gate.

Fig. 4.5 presents measurements on a bilayer WTe_2 device BW2 with multiple gold contacts to the top graphene. When the top graphene was grounded, the bilayer WTe_2 conductance showed a bistability as the bottom gate voltage V_b is swept up and down. Because V_b changes both the perpendicular electric field and doping of the bilayer WTe_2, the changes in G spanned a bigger range as compared with Fig. 4.3b. Here, the bilayer WTe_2 itself can be used to gate the graphene.

In the device BW2, the graphene extends over regions with no WTe_2 underneath. Consequently, care was taken to measure G_{gr} with maximal sensitivity to only a central region of graphene that overlaps the WTe_2. To achieve this, G_{gr} was measured by passing current through opposite contacts while the two side contacts are grounded to minimize parasitic current flowing through the part of the top graphene, not screened from the bottom gate by the bilayer WTe_2. However, due to finite contact resistances, a small portion of this current still flowed through graphene not above the WTe_2. To remove this parasitic component, we set the WTe_2 voltage V_W such that the graphene is at its Dirac-point minimum in the region over the WTe_2. Because the minimum is quite broad, the graphene over the WTe_2 is then insensitive to V_b and any measured

dependence on V_b can come from only the parasitic component and thus, it can be subtracted out. Note that removing it has no effect on the magnitude of the hysteresis.

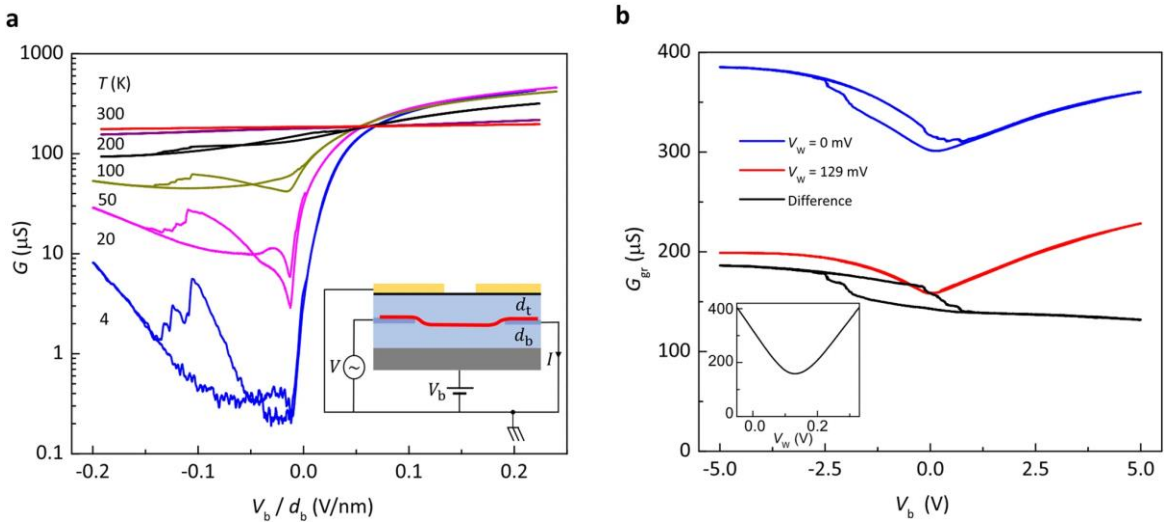

Figure 4.5 (a) Conductance G versus V_b for the bilayer WTe_2 in device BW2, with the top graphene grounded. Note that both n_e and $E_\perp$ change when V_b is swept. The inset shows a schematic configuration of the measurement. (b) Graphene conductance G_{gr} at 220 K as a function of V_b with the voltage V_W on the bilayer WTe_2 at 0 mV (blue) and 129 mV (red). The black curve is the difference between the blue and red curves. This subtraction removes most of the V_b dependence of the parasitic current that flows through the top graphene, which is not screened from the bottom gate by the WTe_2. Inset, graphene conductance showing the minimum at $V_W =$ 129 mV.

Fig. 4.5b illustrates this procedure at 220 K. As shown in the inset, we determined that the graphene above the WTe_2 is at its Dirac point at $V_W = 129$ mV (with the back gate grounded). The red curve shows the conductance of the graphene G_{gr} when $V_W = 129$ mV wherein a "V"-shaped V_b dependence is from only the parasitic contribution. As shown in the blue curve of Fig. 4.5b we also measured G_{gr} at $V_W = 0$ mV, when the graphene is most sensitive to changes in the electric field in the top h-BN E_t, yet also contains the parasitic conductance. The difference between these

two curves, shown in black, helps us detect and quantify the polarization. It shows that the hysteresis remains, whereas the "V" shape is mostly removed.

Using this procedure we also observed such behavior at different temperatures as shown in Fig. 4.6a. From 4 K to 300 K, clear hysteresis loops were seen in G_{gr} as V_b was swept up and down with the WTe_2 bilayer grounded. At each temperature, the back gate could be grounded instead and G_{gr} measured as a function of V_W, as shown in Fig. 4.6b for $T = 4$ K. In this configuration, V_W has a one-to-one relationship to E_t, $V_W \sim d_t E_t$, and so $G_{gr}(V_W) \propto G(E_t)$ is continuous. To illustrate the effect of out-of-plane polarization in the WTe_2 on G_{gr}, a sketch of the potential landscape is drawn in Fig. 4.6c for the simplified case where $d_t = d_b$ and the bottom gate, bilayer WTe_2 and graphene are all grounded. The red and green curves show the electrical potential for polarization up and down, respectively. Though the potential at the center of bilayer WTe_2 must be zero, spontaneous polarization causes the two layers to be at opposite potentials. For the up polarization state, a positive electric field is applied to the graphene. Conversely, it is negative for the down polarization state of the bilayer.

δE_t is the change of electric field at the graphene due to the switching polarization. To measure δE_t, the dependence of G_{gr} on V_b (with $V_W = 0$) is compared to its dependence on V_W (with $V_b = 0$). In the former, the approximately stable values of G_{gr} on either branch of the loop correspond to specific values of E_t. These stable values of G_{gr} have corresponding values of V_W in the latter measurement which, as mentioned earlier, relates G_{gr} to E_t via V_W. This relationship is made exact when taking differences. Therefore, the difference in corresponding V_W gives exactly the change in E_t due to the polarization flip, $\delta V = d_t \delta E_t$. This result is plotted as a function of temperature T in Fig. 4.6d. It decreases roughly linearly with T with 60 K to 300 K,

extrapolating to zero at roughly 450 K, which provides a rough estimate for Curie temperature of bilayer WTe_2. Note that from this we can also extract the areal polarization density $P = \varepsilon_0 \delta V$.

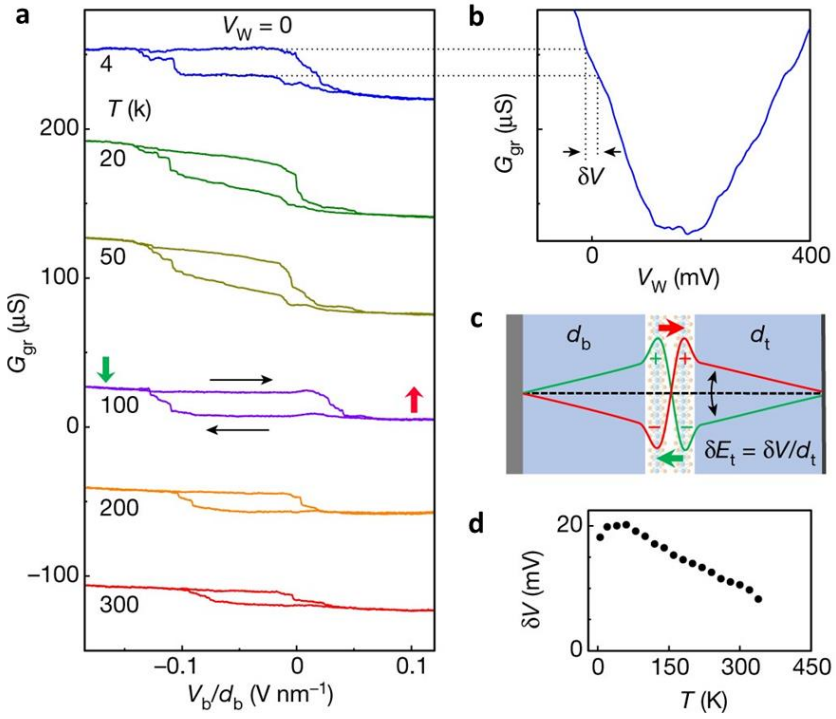

Figure 4.6 Temperature dependence of polarization in bilayer WTe_2. (a) G_{gr} as a function of V_b after removing parasite conductance at $V_W = 0$ at a series of temperatures. Black arrows show sweeping direction of V_b. The two conductance states seen for sweeping up and down are associated with different out-of-plane polarization (red and green arrows). (b) G_{gr} versus V_W with y-axis having the same scale with panel, providing a mapping to the difference $\delta E_t = \delta V/d_t$ in E_t between the two cases. (c) Sketch showing how switching polarization of bilayer WTe_2 changes E_t and the electrostatic potential (from red to green). (d) δV, which is proportional to the polarization, mapped out by panel (a) and (b) as a function of temperature.

4.1.3 Mechanism of ferroelectric order in >2L WTe_2 – stacking order

Above we established how room-temperature vertical ferroelectricity was experimentally shown in bilayer WTe_2. However, this ferroelectric switching is not produced by vertical ionic displacements. Following our experimental findings, an explanation for this behavior was

proposed via first-principles calculation[82]. This predicted a finite out-of-plane polarization stemming from an uncompensated interlayer vertical charge transfer that depends on in-plane translation of one of the layers relative to another which can be switched upon interlayer sliding. Recall that WTe_2 has a corrugated 1T' monolayer structure which causes adjacent layers to stack with an offset, as shown in Figure 4.7. Shifting of one of the layers flips the orientation of this offset. As this transformation is equivalent to mirroring the entire structure, it can thus flip the polarization vector (Fig. 4.7b). This work also explained how the in-plane rigidity of WTe_2 layer gives rise to the high Curie temperature despite its small ferroelectric switching barrier and polarization. This phenomenon is generic to layered structures and recently was demonstrated in artificial bilayer boron nitride made via van der Waals assembly with small angle twist[83].

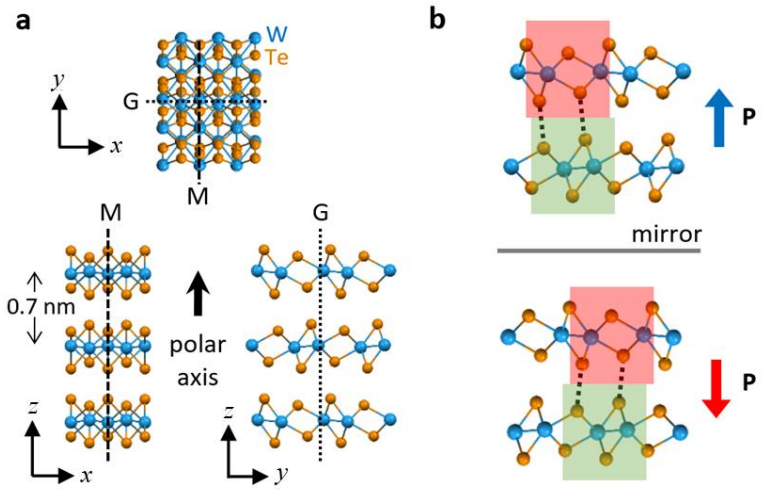

Figure 4.7 Crystal structure of WTe_2. (a) Structure and symmetries of 3L WTe_2, reproduced from Fig. 4.1. (b) Reflecting the crystal in the (*x*-*y*) plane of the layers reverses the polar axis, which is physically equivalent to a small change in alignment of the layers: the pink cell is shifted relative to the green cell. In 2- and 3-layer WTe_2 films we inferred an out-of-plane polarization P which can be flipped by electric field which, by this argument, causes such a stacking transition.

The intrinsic bistability in a thin sheet of the layered semimetal WTe_2 suggests a new physical property leveraged for in nonvolatile memory: the stacking alignment between the layers in a

layered van der Waals material. Because such “stacking order” ferroelectricity persists to room temperature while preserving metallicity for some materials (e.g. trilayer WTe_2), it paves the way for potential ultrathin nonvolatile memory applications.

Switching between the states in WTe_2 is readily achieved using an electric field. Uniquely, as the first true ferroelectric metal it is metallic in the plane while being polarized out of the plane. Critically, its conductivity depends on the polarization state (Fig. 4.3), enabling a direct means of reading the polarization state. These unusual qualities, in combination with those of graphene and other layered materials or thin films, merit investigation for their potential to make a novel, compact and very stable room-temperature nonvolatile memory based on electrically addressable van der Waals stacking (Fig. 4.8).

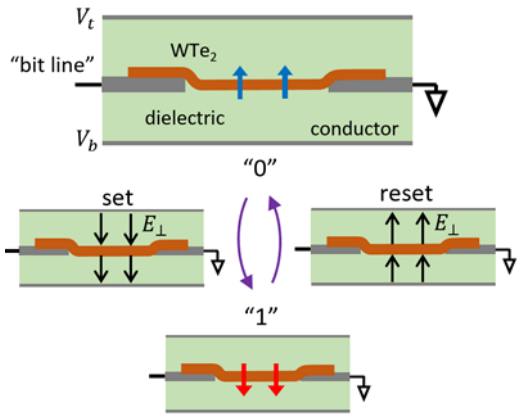

Figure 4.8 The basic idea of electrically addressed van der Waals stacking-based memory. For memory, one could write by switching the state of the WTe_2 and read by measuring conductance, with or without an applied gate bias.

4.2 Bilayer WTe_2 as an excitonic insulator candidate

4.2.1 Chemical potential measurement

Beyond ferroelectricity, transport and chemical potential measurements on bilayer WTe_2 as shown in Fig. 4.9 show striking similarities to those on monolayers discussed in Chapter 3. It should be

noted that while in bilayer it is more straightforward to measure conductance because it lacks edge conduction, ferroelectric switching[61] complicates measurements of the chemical potential.

For the former measurement, a sharp "V" consistently develops in conductance vs. gate voltage measurements in bilayer WTe_2 at the neutral point at around 20 K (Fig. 4.9a). This is similar to what was seen with monolayer WTe_2, though the bilayer "V" does not evolve into a plateau with further cooling. For the latter, a ~10 meV step in the chemical potential (Fig. 4.9b) can be seen starting at around 75 K that is fully developed below 20 K. This suggests that similar excitonic physics is at play in the bilayer but at a ~5 times smaller energy scale than that in the monolayer.

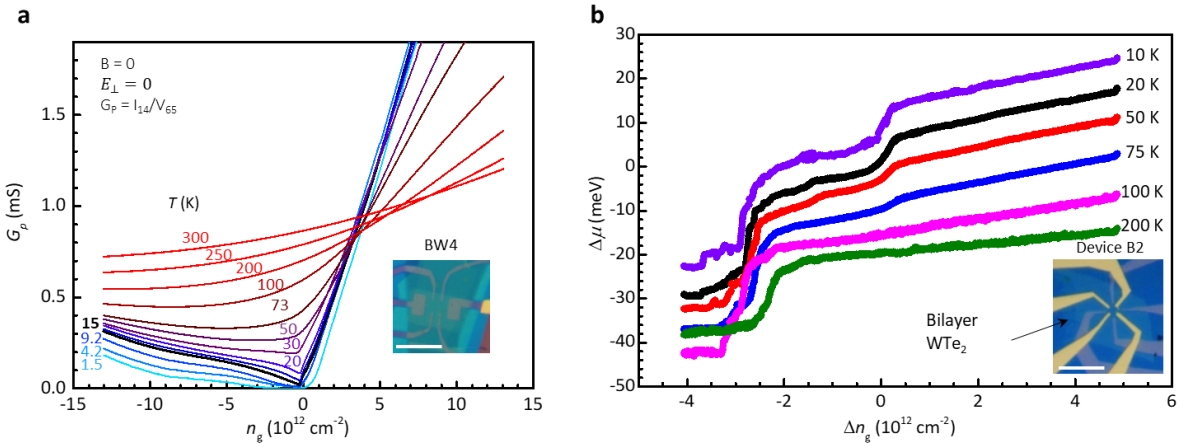

Figure 4.9 (a) Conductance (inverse 4-terminal resistance) characteristics of 2L WTe_2 device BW4 (for zero displacement field). Inset: microscope image of device, scale bar: 2 μm. (b) Chemical potential: ferroelectric switching in the bilayer limits the range of the chemical potential measurement: these measurements are all performed sweeping n_g downwards in a single polarization state. The jump of $\Delta\mu$ at non-zero doping level originates from ferroelectric switching. Inset: microscope image of device, scale bar: 10 μm.

4.2.2 Metallic state of bilayer WTe_2 on strontium titanate ($SrTiO_3$)

When a monolayer or few-layer two-dimensional semiconductor is placed a solid substrate, interfacial interactions between the layered materials and substrate must be considered. Done with care, changing substrates can introduce additional parameters for study, such as engineering of the dielectric environment of the material of interest. In this section, I will briefly discuss about how we did exactly this to tune the phases of bilayer WTe_2.

Specifically, we studied bilayer WTe_2 on substrates of strontium titanate, or $SrTiO_3$. $SrTiO_3$ has an indirect band gap of 3.25 eV and a direct gap of 3.75 eV[84]. Synthetic $SrTiO_3$ has a very large dielectric constant (ε_0 = 300) at room temperature. It has resistivity exceeding 10^9 Ω-cm for very pure crystals. At $T_{AFD} = 150$ K, $SrTiO_3$ undergoes a cubic-to-tetragonal structural transition (to space group 14/mcm), with a small distortion c/a = 1.00056[85]. This is known as an antiferrodistortive (AFD) transition, since the positions of the Sr and Ti atoms remain fixed, while the oxygen octahedra rotate about one of the cubic axes, with opposite rotation in adjacent cells. Interestingly, it has been shown that the dielectric susceptibility in $SrTiO_3$ first grows rapidly with cooling from room temperature, as would be seen in a ferroelectric, until at $T \sim 10$ K when this growth slows and ultimately saturates at $T = 4$ K with $\varepsilon_0 \approx 2\times10^4$. This indicated that this material is a quantum paraelectric, wherein the dielectric susceptibility diverges as the material approaches a ferroelectricity instability with cooling until the temperature is sufficiently low for quantum fluctuations to cancel out the ferroelectricity[86].

As a band insulator with high dielectric constant, $SrTiO_3$ can serve both as a high-dielectric constant environment and a back gate dielectric for a 2D material placed on it. It has also been used to screen (weaken) electron-electron interaction in graphene[87]. In graphene, ferromagnetic phase have been experimentally observed[88,89] using extremely large applied in-plane magnetic

field, exceeding 30 T. In this regime, the Zeeman energy overcomes the other interaction terms. Similar behavior has also been seen using misaligned graphene bilayers with two layers hosting different quantum Hall states of opposite charge-carrier types[90]. By adding $SrTiO_3$ nearby (as a substrate), it was observed that spin-polarization terms become dominant and a ferromagnetic phase is induced by modifying the effects of the lattice-scale interaction via screening.

Thinking along these lines, we studied a similar device geometry with bilayer WTe_2 (Fig. 4.10b & c) on 500 μm thick $SrTiO_3$ (100) substrates. The surfaces of these substrates were prepared with atomically flat terraces via annealing in air at $T \sim 1000$ ℃ and cleaning in water. Au was deposited at the back of the substate to serve as a back gate electrode. Top graphite/hBN/bilayer WTe_2 heterostructures were made from exfoliated flakes using the standard van der Waals pick-up[56]. Top graphite was used as top gate. Inner Pt contacts and outer Cr/Au contacts were patterned by electron-beam lithography and metallized by e-beam evaporation.

Two-terminals measurements were performed with a standard low-frequency lock-in amplifier technique in voltage-bias configuration by applying an ac bias voltage. Unlike bilayer WTe_2 on hBN, the conductivity is very high (~40 μS) even at $T = 10$ mK. With sweeping of the top gate voltage, the conductance reaches its minimum around $V_{tg} = 0$ V, indicating the high conductivity does not result from unexpected electron doping (inset of Fig. 4.10a)). Meanwhile, the conductivity at neutral point increases at $T = 4$ K. At this temperature, the dielectric constant of $SrTiO_3$ should have reached to 2×10^4, substantially screening Coulomb interactions in the bilayer WTe_2. This further evinces that the insulating state of bilayer WTe_2 is driven by electron-electron interaction and supports its candidacy as an excitonic insulator.

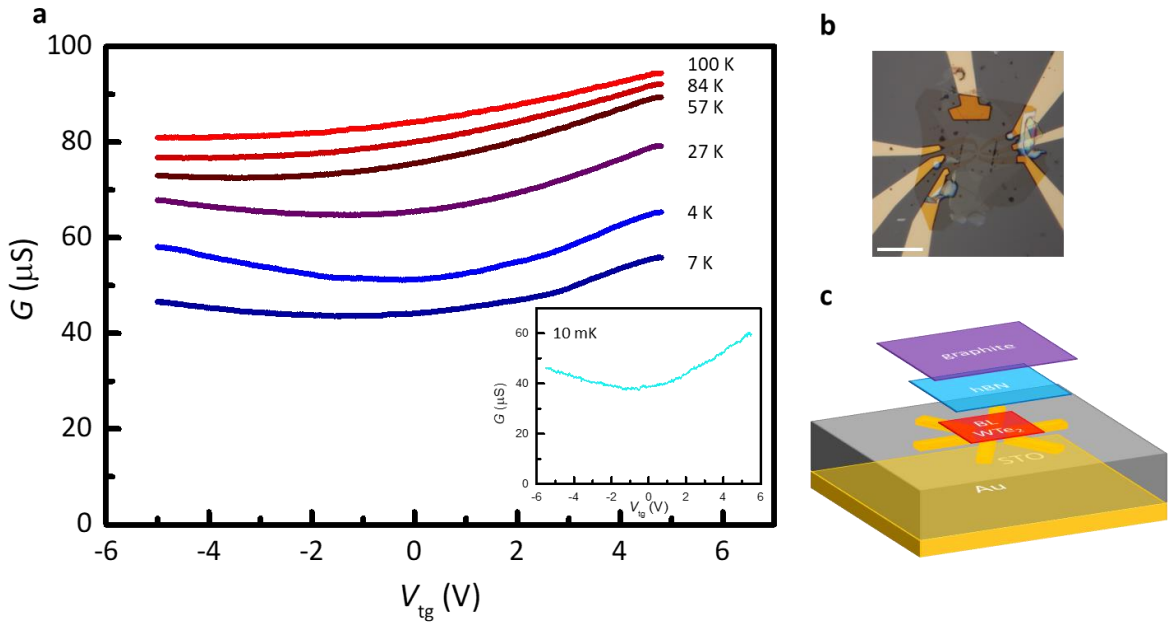

Figure 4.10 (a) Conductance characteristics of bilayer WTe_2 device on $SrTiO_3$. Here the inverse 4-terminal resistance is plotted. (b) Optical image of device, scale bar: 15 μm. (c) Schematic of the hBN-encapsulated bilayer WTe_2 placed on a $SrTiO_3$ (STO) substrate that serves both as a high-dielectric constant environment and a back-gate dielectric. Owing to the considerable dielectric constant ($\epsilon_r \sim 20{,}000$) of the $SrTiO_3$ substrate at low temperatures, Coulomb interaction in the bilayer WTe_2 should be substantially screened, thus explaining the high conductance at 10 mK, as shown in the inset of (a).

Chapter 5. Other attempts to fabricate nanoscale devices

In the previous chapter, I have mainly talked about how we fabricate devices to perform transport measurement, MIM measurement, and chemical potential measurement. In this chapter, I will briefly talk about other works which enrich the library of fabrication methods for study of layered two-dimensional materials, such as applying built-in strain, inducing superconductivity into other non-superconducting materials via proximity effect, and tunneling devices.

5.1 Applying built-in strain

As we discussed in Chapter 1, the versatility of layered two-dimensional materials extends beyond tunability by electronic doping, magnetic field, and temperature – parameters we have already considered in detail. Another parameter that has recently proven effective, if challenging to implement, is pressure. For example, it was shown to tune the magnetic order in the two-dimensional magnet CrI_3 by changing the interlayer coupling[91,92]. Similarly, strain can also play an important role in manipulating the electronic and optical properties of two-dimensional materials. In this part, I will briefly introduce a method how to apply built-in strain using quasi-2D nanobeams of VO_2 as an example.

5.1.1 Introduction to VO_2

Over the past decades, elucidation of the physical properties of strongly correlated systems has been one of the most challenging subjects in both theoretical and experimental condensed matter physics. The vanadium-oxide system could be one of the most attractive environments for this pursuit as many of its members exhibit a metal-to-insulator phase transition (MIT) the mechanism of which remains controversial to date. Vanadium dioxide (VO_2) is perhaps the most interesting

compound in the family, not only for its relative chemical simplicity but also because its transition temperature is easily accessible at very nearly room temperature. As reproduced in Fig. 5.1, VO_2 has multiple different structural phases which differ by the degree of dimerization, metallicity, and optical contrast. It was Dr. Jae Park, a former graduate of our group, that proved that VO_2 has a triple point of its metallic and insulating phases, constructing a detailed phase diagram of VO_2[93], as reproduced in Fig. 5.2.

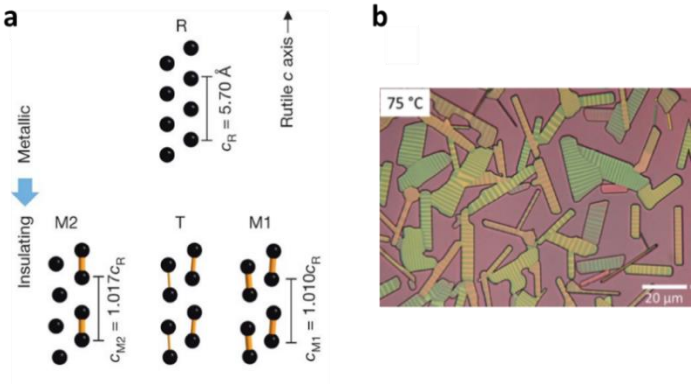

Figure 5.1 (a) Arrangement of vanadium ions in the phases involved in the MIT, indicating their different vanadium chain periods and dimerization (yellow). (b) Alternation of metallic and insulating domains. At 75 ℃, substrate-pinning combined with a mismatching thermal expansion produces coexistence of the insulating (yellow, brighter) and the metallic (green, darker) phases. (Figure adapted from reference[93])

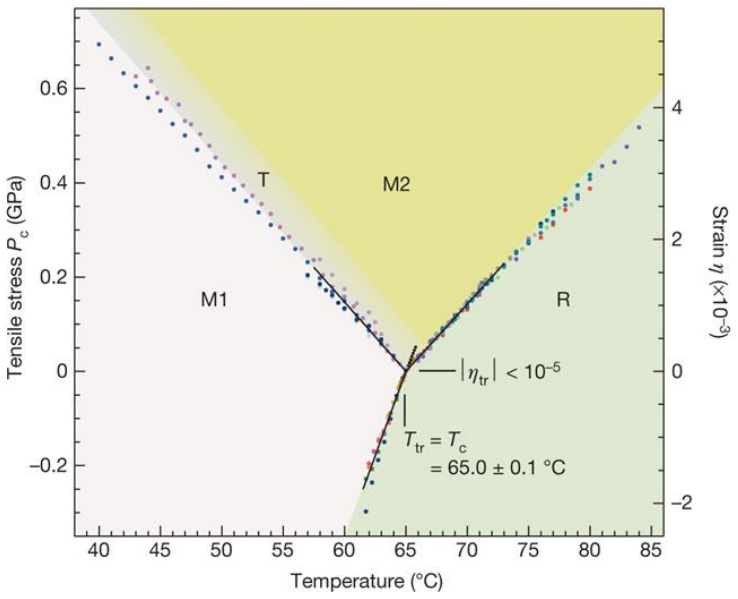

Figure 5.2 Constructed phase diagram of VO_2 nanobeam as a function of temperature and tensile strain from measurements. (Figure reproduced from reference[93])

5.1.2 Process to apply strain

The process to apply strain is shown in Fig. 5.3a. A material of interest is mounted across a slot in a silicon chip. The width of the slot gap is tuned and strain applied to the nanobeam by pressing on a particular side of the chip. A VO_2 nanobeam can be placed thusly across the slot using a probe needle and affixed on both sides using UV-cure epoxy. Using a homebuilt strain platform, we narrow the slot before placing and fixing the samples, thereby applying tensile strain when the compression of the slot is released. By measuring the gap width change, we can estimate the amount of applied strain. These 2×2 mm^2 chips are fabricated using photolithography (PL) and deep reactive ion etching (DRIE) and have spring-like mechanism to facilitate the compression. Different spring geometries are shown in Fig. 5.3c. More details on these topics are presented below.

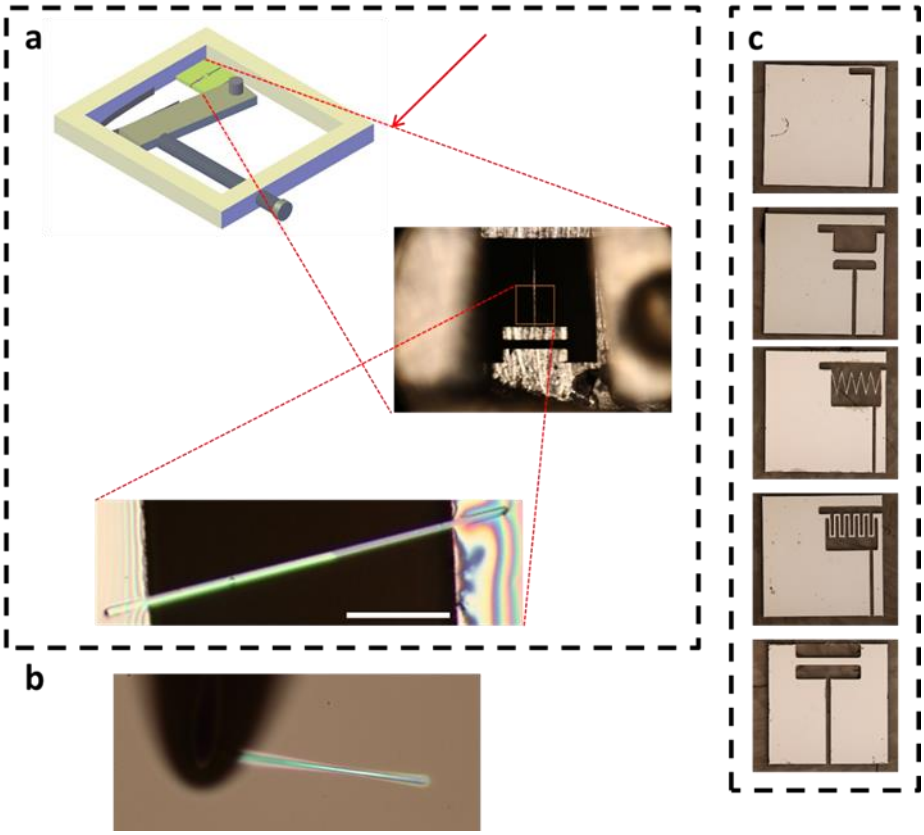

Figure 5.3 (a) Process to apply built-in strain: (top) 3D model of platform; (middle) Si chip with squeezed slot before VO_2 was transferred across the slot; (bottom) slot with mounted nanobeam. With built-in strain, the nanobeam demonstrates coexistence at the phase transition (dark. green: metallic, light, yellow: insulating), scale bar: 20 μm. (b) Microscope images of a nanobeam being picked up due to a van der Waals attraction, using a probe needle. (c) Fabricated Si chips (2×2 mm^2) with different designs of the spring mechanism with which to squeeze the slot.

5.1.2.1 Transfer VO_2 nanobeam

A given large crystal of VO_2 may develop multiple twinned domains. However, each domain is limited to a certain characteristic size. If a crystal has a dimension comparable or smaller than this size, it is unlikely that multiple domains will develop in that direction. Therefore, in a sufficiently thin nanobeam domain structure is only possible along the length of the nanobeam. In order to realize an even simpler system, it is desirable to avoid domain structure from substrate pinning so that the nanobeam remains a singly domain though a phase transition. To this end, a systematic

approach to studying the MIT is best exemplified in a suspended VO_2 nanobeam that allows superior control of the strain and other parameters.

This is achieved by suspending our VO_2 nanobeam across a slot. To transfer a VO_2 nanobeam, our extensively used method is direct manipulation of a single VO_2 nanobeam using a 3-axis stepper-controller motorized manipulator. The manipulator is mounted on a microscope stage for in-situ transferring. Since these VO_2 nanobeams are grown using CVD and consequently pinned to the oxide substrate surface they must first be loosened with a light BOE etching. A nanobeam is then picked up due to a van der Waals attraction (See. Fig. 5.3b) using a probe needle (usually a tungsten needle from Quarter Research) attached to the manipulator.

5.1.2.2 Adhesion

To study the different types of domain boundaries in a nanobeam without access to in-situ tuning of the strain (as we had intended to do), it is necessary to prepare the suspended sample pre-strained. This strain is applied after releasing the gap with VO_2 nanobeam fixed on both sides. Good adhesion is naturally necessary for this to work. Here, we use epoxy to fix the VO_2 nanobeam. Norland NEA121, a UV curable epoxy, is an ideal candidate for several reasons. (i) It was chosen for its appropriate viscosity (300 cps, comparable to a motor oil). (ii) There is no need to mix with a resin. (iii) It is not solvent based and so its viscosity does not change before curing. (iv) The curing process can be initiated by either UV light or heat and allows plenty of time for application and other sample processing. (v) The epoxy is optically clear. This allows visual inspection of the domains under epoxy.

5.1.2.3 Fabrication of Si chip and platform

To apply pre-strain, we first squeeze the slot by pressing on a side of the chip and causing it to bend. To make this feasible, we used a 250 μm Si wafer which is thin enough to be bent but thick enough to be a rigid substrate. Fabricated Si chips (2×2 mm^2) are shown on Fig. 5.3c. Different designs of the compliant spring mechanism let us find the most appropriate to best control strain. Masks were prepared (Heidelberg μPG 101) for photolithography (AB-M Contact Aligner). The bulk of the wafer was etched quickly and uniformly with DRIE (Bosch process).

5.2 Inducing superconductivity into 2D materials

Inducing superconducting correlations via the proximity effect into a 2DEG has attracted renewed attention due to its promise for realizing non-Abelian zero modes. It has been proposed that the proximity effect between an *s*-wave superconductor and the surface states of a strong topological insulator can result in a two-dimensional state resembling a spinless $p_x + ip_y$ superconductor without breaking time reversal symmetry which supports Majorana bound states at vortices[94]. To try to achieve this, we started with making lateral Josephson junctions of $NbSe_2$/graphene/$NbSe_2$.

$NbSe_2$ is a superconductor with a critical temperature $T_c = 7.2$ K[95]. The critical temperature drops when the $NbSe_2$ layers are intercalated by other atoms, or when the sample thickness decreases, with T_c being ~ 1 K in a monolayer[96]. Like other layered transition metal dichalcogenides, $NbSe_2$ can be mechanically exfoliated into single crystalline layers, which makes it compatible with 2D materials fabrication and techniques. Reportedly, vertical stacked $NbSe_2$/graphene/$NbSe_2$ has been fabricated[97]. To make it compatible with electrostatic doping, we designed a lateral Josephson junction geometry (Fig. 5.4).

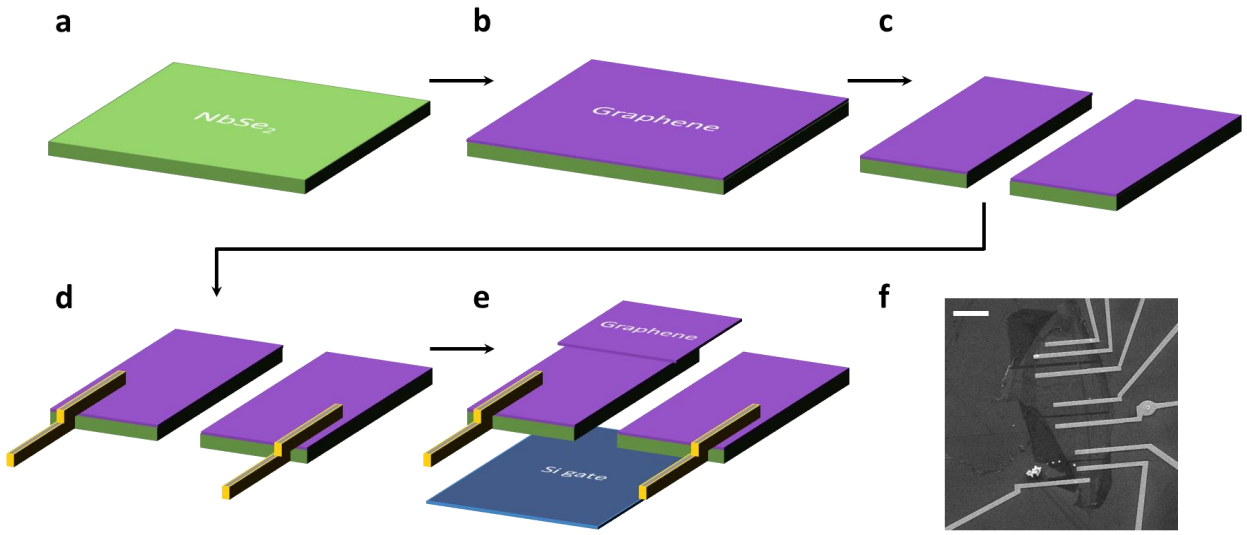

Figure 5.4 Schematic process to make lateral Josephson junction of $NbSe_2$/graphene/$NbSe_2$ (a) Exfoliation of thin flakes of $NbSe_2$ (~10 nm). (b) To protect $NbSe_2$ from being oxidized, a piece of graphene is covered on top. (c) ~ 200 nm wide slot is made on the stack of graphene/$NbSe_2$ using a process combining electron beam lithography and reactive ion etching with CHF_3 and O_2 mixture. (d) Evaporate Pt contacts. (e) Graphene is transferred across the slot, and the junction has been made. The junction is being made on the substrate of SiO_2/Si, hence the Si gate can be used for electrostatic doping (f) SEM image of the lateral Josephson junction, scale bar: 10 μm.

Using this device, we studied transport at temperatures where the Josephson supercurrent was observable (slightly below $T_c = 5.3$ K). Fig. 5.5 shows the junction forward current biasing current-voltage characteristics without gating. Fig. 5.6a-c shows these over a range of T from 1.6 K to 7.0 K, gate voltage from 0 V to 6 V, and out-of-plane magnetic field B from 0 T to 1.5 T. The low-bias transition occurred at the critical current $I_c = 73$ μA, $T = 1.6$ K. Above I_c, the normal resistance, R_N, is tunable by Si gate. Supercurrent can still be observed at $B_\perp = 1.5$ T.

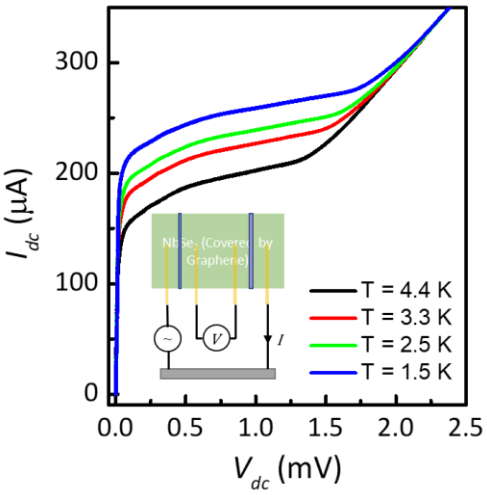

Figure 5.5 Current-voltage characteristics of $NbSe_2$ between 1.5 K and 4.4 K. Inset: circuit setup.

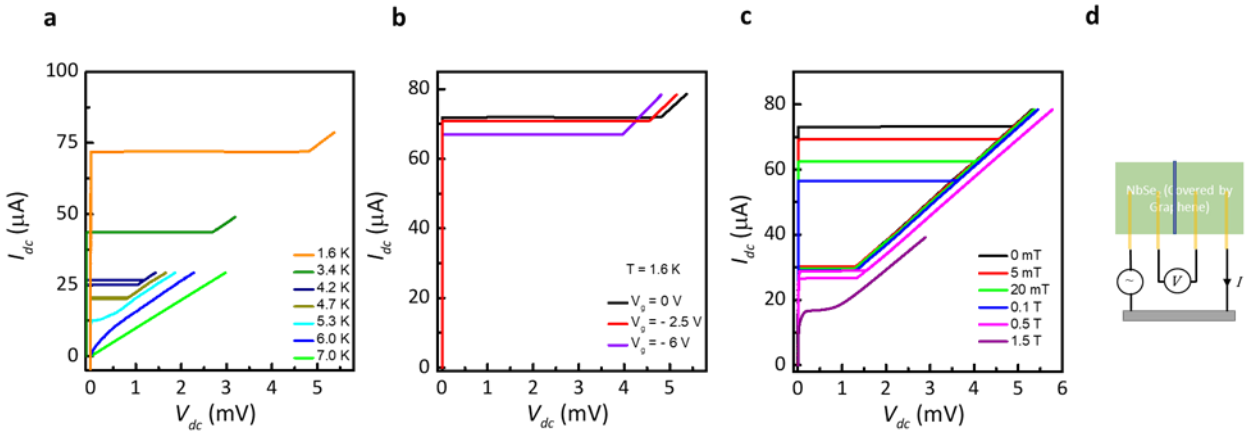

Figure 5.6 (a-c) Current-voltage characteristic of Josephson junction measured at different temperatures, gate voltage, and magnetic field. (d) Circuit setup.

We successfully prepared a lateral junction of $NbSe_2$/graphene/$NbSe_2$ with a workable approach. The clean interface between $NbSe_2$ and graphene produced a highly transparent, short-ballistic proximity-type Josephson coupling with a robust critical current. Constructing transparent Josephson junctions using $NbSe_2$ and graphene represents an efficient and promising route to

building coherent hybrid systems if we replace graphene to other 2D materials. This will open an exciting route to explore exotic quantum phenomena at the atomic scale.

5.3 Electron tunneling through ultrathin hBN

Since h-BN is chemically and thermally stable and free of dangling bonds and surface charge traps, it is universally used as a substrate for graphene electronics, in which the mobility, FET performance and chemically stability get improved. Crystals of hBN thicker than six layers are known to act as high-quality insulating layers in most of the 2D materials devices. A single atomic layer of h-BN on the other hand acts as an effective tunnel barrier and the transmission probability of the h-BN barrier decreases exponentially with the number of atomic layers. This property offers us another method to study the interior bulk of monolayer WTe_2.

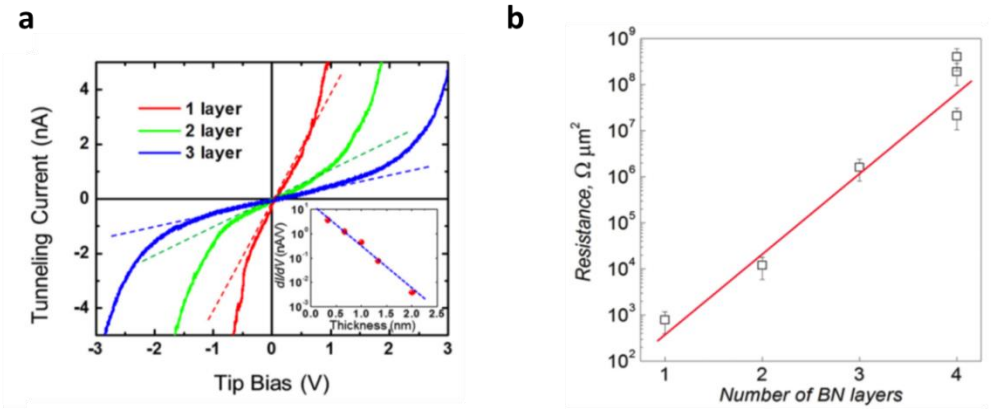

Figure 5.7 (a) Current-voltage curves of mono-, bi-, and tri-layer h-BN. Inset: log-scale tunnel conductance in the linear regime. (b) Exponential dependence of zero-bias resistance on the thickness hBN separating graphite and gold electrodes (1-4 layers of hBN, 0.3-1.3 nm). Resistance is normalized to the area, which ranged from 2 to10 μm^2 (Figures adapted from reference[98,99])

As Ch. 2 might have shown, we need to differentiate the current contributions from edges and the interior bulk. Here, we used the device design shown in Fig. 5.8c to try to limit tunneling

current to coming from the interior. In this way, by measuring tunneling current we can figure out the density of states we are interested in. hBN etched by RIE with CHF_3 and O_2 mixture can be picked up via vdW transfer technique. However, it proved challenging to make electron tunneling devices as 1L hBN is especially fragile and can easily be broken during transfer.

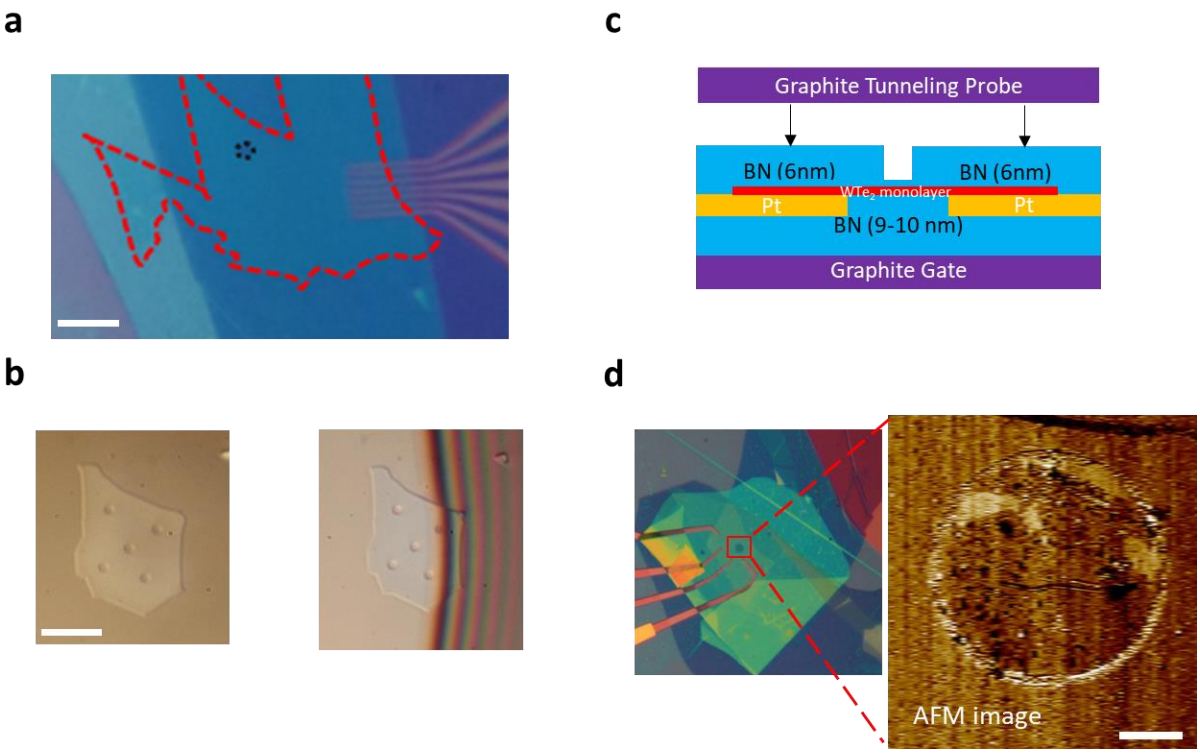

Figure 5.8 Process to make electron tunneling devices for monolayer WTe_2 (a) Microscope image of device. Read dashed line outlines the boundary of monolayer WTe_2, and the black dashed line highlight the position which the monolayer hBN cover, scale bar: 10 μm. (b) Transfer process of etched hBN, scale bar: 10 μm. (c) Cross-sectional diagram of devices. Graphite on top is used as electron tunneling probe. (d) Challenge of using thin hBN: 1L hBN is fragile and can be broken during the transfer. Scale bar of AFM image: 1 μm.

Chapter 6. Outlook

Over the last decade, discovery of various two-dimensional materials and rapid development of controllable fabrication methods make it possible of us to build various device with extraordinary performance. These techniques led us to discover and confirm the quantum spin Hall insulator (QSHI) state of 1L WTe_2. It allows QSHI to exist independently of quantum well in nature. Subsequently, superconductor state was found 1L WTe_2 and ferroelectricity was found 2L WTe_2. These reflects the great potential of two-dimensional materials.

The constructed phase diagram of 1L WTe_2 makes us reconsider the ground state of 1L WTe_2. In this thesis, I mainly discuss about the nature of electronic states and excitonic condensation in 1L WTe_2. The further understanding of the ground state in 1L WTe_2, where the interplay between excitonic insulator phase, topology and superconductivity, may open a new avenue for exploring correlated topological states. And at the same time, 2L WTe_2, as an excitonic insulator candidate, makes this research more challenging since ferroelectricity needs to be incorporated in this theoretical frame.

From an application perspective, the richness of phases in 1L and 2L WTe_2 create more possibilities of electronics. As discussed in Ch. 3 and 4, combination of ferromagnet, superconductor and QSHI is proposed to realize Majorana mode. Ferroelectricity of 2L WTe_2 paves the way for potential ultrathin nonvolatile memory applications. In the last chapter, I briefly introduce attempts to enrich fabrication methods to study nanomaterials. Driven by more techniques to fabricate and more dimensions to study, the interest in two-dimensional and layered materials continues to expand. There are a lot of opportunities for us to explore uncharted scientific territory and to discover technologically useful 2D materials.

BIBLIOGRAPHY

1. Ng, K. K. & Sze, S. *Physics of Semiconductor Devices*.
2. Girvin, S. & Yang, K. *Modern Condensed Matter Physics*.
3. Cao, Y. *et al.* Correlated insulator behaviour at half-filling in magic-angle graphene superlattices. *Nature* **556**, 80–84 (2018).
4. Cao, Y. *et al.* Unconventional superconductivity in magic-angle graphene superlattices. *Nature* **556**, 43–50 (2018).
5. Kane, C. L. & Mele, E. J. Quantum spin Hall effect in graphene. *Phys. Rev. Lett.* **95**, 226801 (2005).
6. Kane, C. L. & Mele, E. J. Z_2 Topological order and the quantum spin Hall effect. *Phys. Rev. Lett.* **95**, 146802 (2005).
7. Jérome, D., Rice, T. M. & Kohn, W. Excitonic insulator. *Phys. Rev.* **158**, 462–475 (1967).
8. Keldysh, L. & Kopaev, Y. Possible instability of semimetallic state toward Coulomb interaction. *Sov. Phys. Solid State* **6**, 2219–2224.
9. Cloizeaux, J. D. Exciton instability and crystallographic anomalies in semiconductors. *Journal of Physics and Chemistry of Solids* **26**, 259–266 (1965).
10. Halperin, B. I. & Rice, T. M. Possible anomalies at a semimetal-semiconductor transition. *Rev. Mod. Phys.* **40**, 755–766 (1968).
11. Rohwer, T. *et al.* Collapse of long-range charge order tracked by time-resolved photoemission at high momenta. *Nature* **471**, 490–493 (2011).

12. Kogar, A. *et al.* Signatures of exciton condensation in a transition metal dichalcogenide. *Science* **358**, 1314–1317 (2017).
13. Lu, Y. F. *et al.* Zero-gap semiconductor to excitonic insulator transition in Ta_2NiSe_5. *Nature Communications* **8**, 14408 (2017).
14. Werdehausen, D. *et al.* Coherent order parameter oscillations in the ground state of the excitonic insulator Ta_2NiSe_5. *Science Advances* **4**, eaap8652 (2018).
15. Varsano, D. *et al.* Carbon nanotubes as excitonic insulators. *Nature Communications* **8**, 1461 (2017).
16. Ataei, S. S., Varsano, D., Molinari, E. & Rontani, M. Evidence of ideal excitonic insulator in bulk MoS_2 under pressure. *PNAS* **118**, (2021).
17. Eisenstein, J. P. & MacDonald, A. H. Bose–Einstein condensation of excitons in bilayer electron systems. *Nature* **432**, 691–694 (2004).
18. Nandi, D., Finck, A. D. K., Eisenstein, J. P., Pfeiffer, L. N. & West, K. W. Exciton condensation and perfect Coulomb drag. *Nature* **488**, 481–484 (2012).
19. Li, J. I. A., Taniguchi, T., Watanabe, K., Hone, J. & Dean, C. R. Excitonic superfluid phase in double bilayer graphene. *Nature Physics* **13**, 751–755 (2017).
20. Liu, X., Watanabe, K., Taniguchi, T., Halperin, B. I. & Kim, P. Quantum Hall drag of exciton condensate in graphene. *Nature Physics* **13**, 746–750 (2017).
21. Bernevig, B. A. & Zhang, S.-C. Quantum spin Hall effect. *Phys. Rev. Lett.* **96**, 106802 (2006).
22. Hasan, M. Z. & Kane, C. L. Colloquium: Topological insulators. *Rev. Mod. Phys.* **82**, 3045–3067 (2010).
23. Qi, X.-L. & Zhang, S.-C. Topological insulators and superconductors. *Rev. Mod. Phys.* **83**, 1057–1110 (2011).

24. König, M. *et al.* Quantum spin Hall insulator state in HgTe quantum wells. *Science* **318**, 766–770 (2007).
25. Knez, I., Du, R.-R. & Sullivan, G. Evidence for helical edge modes in inverted InAs/GaSb quantum wells. *Phys. Rev. Lett.* **107**, 136603 (2011).
26. Murakami, S. Quantum spin Hall effect and enhanced magnetic response by spin-orbit coupling. *Phys. Rev. Lett.* **97**, 236805 (2006).
27. Xu, Y. *et al.* Large-gap quantum spin Hall insulators in tin films. *Phys. Rev. Lett.* **111**, 136804 (2013).
28. Qian, X., Liu, J., Fu, L. & Li, J. Quantum spin Hall effect in two-dimensional transition metal dichalcogenides. *Science* **346**, 1344–1347 (2014).
29. Zhou, J.-J., Feng, W., Liu, C.-C., Guan, S. & Yao, Y. Large-gap quantum spin Hall insulator in single layer bismuth monobromide Bi_4Br_4. *Nano Lett.* **14**, 4767–4771 (2014).
30. Wang, L. *et al.* Tuning magnetotransport in a compensated semimetal at the atomic scale. *Nature Communications* **6**, 8892 (2015).
31. Cao, Y. *et al.* Quality heterostructures from two-dimensional crystals unstable in air by their assembly in inert atmosphere. *Nano Lett.* **15**, 4914–4921 (2015).
32. Ye, F. *et al.* Environmental instability and degradation of single- and few-layer WTe_2 nanosheets in ambient conditions. *Small* **12**, 5802–5808 (2016).
33. Zheng, F. *et al.* On the quantum spin Hall gap of monolayer 1T′-WTe_2. *Advanced Materials* **28**, 4845–4851 (2016).
34. Fei, Z. *et al.* Edge conduction in monolayer WTe_2. *Nature Physics* **13**, 677–682 (2017).
35. Tang, S. *et al.* Quantum spin Hall state in monolayer 1T'-WTe_2. *Nature Physics* **13**, 683–687 (2017).

36. Jia, Z.-Y. *et al.* Direct visualization of a two-dimensional topological insulator in the single-layer 1T'-WTe_2. *Phys. Rev. B* **96**, 041108 (2017).

37. Wu, S. *et al.* Observation of the quantum spin Hall effect up to 100 kelvin in a monolayer crystal. *Science* **359**, 76–79 (2018).

38. Shi, Y. *et al.* Imaging quantum spin Hall edges in monolayer WTe_2. *Science Advances* **5**, eaat8799 (2019).

39. Sajadi, E. *et al.* Gate-induced superconductivity in a monolayer topological insulator. *Science* **362**, 922–925 (2018).

40. Fatemi, V. *et al.* Electrically tunable low-density superconductivity in a monolayer topological insulator. *Science* **362**, 926–929 (2018).

41. Zhao, W. *et al.* Magnetic proximity and nonreciprocal current switching in a monolayer WTe_2 helical edge. *Nature Materials* **19**, 503–507 (2020).

42. Lüpke, F. *et al.* Proximity-induced superconducting gap in the quantum spin Hall edge state of monolayer WTe_2. *Nature Physics* **16**, 526–530 (2020).

43. Wu, Y. *et al.* Temperature-induced Lifshitz transition in WTe_2. *Phys. Rev. Lett.* **115**, 166602 (2015).

44. Goossens, A. M. *et al.* Mechanical cleaning of graphene. *Appl. Phys. Lett.* **100**, 073110 (2012).

45. Cucchi, I. *et al.* Microfocus laser–angle-resolved photoemission on encapsulated mono-, bi-, and few-layer 1T′-WTe_2. *Nano Lett.* **19**, 554–560 (2019).

46. Ok, S. *et al.* Custodial glide symmetry of quantum spin Hall edge modes in monolayer WTe_2. *Phys. Rev. B* **99**, 121105 (2019).

47. Song, Y.-H. *et al.* Observation of Coulomb gap in the quantum spin Hall candidate single-layer 1T'-WTe_2. *Nature Communications* **9**, 4071 (2018).

48. Varsano, D., Palummo, M., Molinari, E. & Rontani, M. A monolayer transition-metal dichalcogenide as a topological excitonic insulator. *Nature Nanotechnology* **15**, 367–372 (2020).

49. Jia, Y. *et al.* Evidence for a monolayer excitonic insulator. *arXiv:2010.05390 [cond-mat]* (2020).

50. Lee, P. A. Quantum oscillations in the activated conductivity in excitonic insulators: possible application to monolayer WTe_2. *Phys. Rev. B* **103**, L041101 (2021).

51. Kwan, Y. H., Devakul, T., Sondhi, S. L. & Parameswaran, S. A. Theory of competing excitonic orders in insulating WTe_2 monolayers. *arXiv:2012.05255 [cond-mat]* (2020).

52. Zhao, W. *et al.* Determination of the spin axis in quantum spin Hall insulator monolayer WTe_2. *arXiv:2010.09986 [cond-mat]* (2021).

53. Wang, P. *et al.* Landau quantization and highly mobile fermions in an insulator. *Nature* **589**, 225–229 (2021).

54. Kim, M. *et al.* Determination of the thickness and orientation of few-layer tungsten ditelluride using polarized Raman spectroscopy. *2D Mater.* **3**, 034004 (2016).

55. Duong, D. L. *et al.* Raman Characterization of the Charge Density Wave Phase of 1T-$TiSe_2$: From Bulk to Atomically Thin Layers. *ACS Nano* **11**, 1034–1040 (2017).

56. Zomer, P. J., Guimarães, M. H. D., Brant, J. C., Tombros, N. & van Wees, B. J. Fast pick up technique for high quality heterostructures of bilayer graphene and hexagonal boron nitride. *Appl. Phys. Lett.* **105**, 013101 (2014).

57. Xu, S.-Y. *et al.* Electrically switchable Berry curvature dipole in the monolayer topological insulator WTe_2. *Nature Physics* **14**, 900–906 (2018).

58. Wallace, P. R. The band theory of graphite. *Phys. Rev.* **71**, 622–634 (1947).

59. Siviniant, J., Scalbert, D., Kavokin, A. V., Coquillat, D. & Lascaray, J.-P. Chemical equilibrium between excitons, electrons, and negatively charged excitons in semiconductor quantum wells. *Phys. Rev. B* **59**, 1602–1604 (1999).
60. Zittartz, J. Anisotropy effects in the excitonic insulator. *Phys. Rev.* **162**, 752–758 (1967).
61. Fei, Z. *et al.* Ferroelectric switching of a two-dimensional metal. *Nature* **560**, 336–339 (2018).
62. Giannozzi, P. *et al.* Advanced capabilities for materials modelling with Quantum ESPRESSO. *J. Phys.: Condens. Matter* **29**, 465901 (2017).
63. Hamann, D. R. Optimized norm-conserving Vanderbilt pseudopotentials. *Phys. Rev. B* **88**, 085117 (2013).
64. Onida, G., Reining, L. & Rubio, A. Electronic excitations: density-functional versus many-body Green's-function approaches. *Rev. Mod. Phys.* **74**, 601–659 (2002).
65. Hybertsen, M. S. & Louie, S. G. Electron correlation in semiconductors and insulators: Band gaps and quasiparticle energies. *Phys. Rev. B* **34**, 5390–5413 (1986).
66. Strinati, G. Application of the Green's functions method to the study of the optical properties of semiconductors. *Riv. Nuovo Cim.* **11**, 1–86 (1988).
67. Marini, A., Hogan, C., Grüning, M. & Varsano, D. yambo: An ab initio tool for excited state calculations. *Computer Physics Communications* **180**, 1392–1403 (2009).
68. Sangalli, D. *et al.* Many-body perturbation theory calculations using the yambo code. *J. Phys.: Condens. Matter* **31**, 325902 (2019).
69. Elliott, J. D. *et al.* Surface susceptibility and conductivity of MoS_2 and WSe_2 monolayers: A first-principles and ellipsometry characterization. *Phys. Rev. B* **101**, 045414 (2020).
70. Rozzi, C. A., Varsano, D., Marini, A., Gross, E. K. U. & Rubio, A. Exact Coulomb cutoff technique for supercell calculations. *Phys. Rev. B* **73**, 205119 (2006).

71. Muechler, L., Alexandradinata, A., Neupert, T. & Car, R. Topological nonsymmorphic metals from band inversion. *Phys. Rev. X* **6**, 041069 (2016).

72. Monney, C. *et al.* Spontaneous exciton condensation in 1T-$TiSe_2$: BCS-like approach. *Phys. Rev. B* **79**, 045116 (2009).

73. Dawber, M., Rabe, K. M. & Scott, J. F. Physics of thin-film ferroelectric oxides. *Rev. Mod. Phys.* **77**, 1083–1130 (2005).

74. Scott, J. F. Applications of modern ferroelectrics. *Science* **315**, 954–959 (2007).

75. Anderson, P. W. & Blount, E. I. Symmetry considerations on martensitic transformations: 'ferroelectric' metals? *Phys. Rev. Lett.* **14**, 217–219 (1965).

76. Shi, Y. *et al.* A ferroelectric-like structural transition in a metal. *Nature Materials* **12**, 1024–1027 (2013).

77. Benedek, N. A. & Birol, T. 'Ferroelectric' metals reexamined: fundamental mechanisms and design considerations for new materials. *J. Mater. Chem. C* **4**, 4000–4015 (2016).

78. Kim, T. H. *et al.* Polar metals by geometric design. *Nature* **533**, 68–72 (2016).

79. Sakai, H. *et al.* Critical enhancement of thermopower in a chemically tuned polar semimetal $MoTe_2$. *Science Advances* **2**, e1601378 (2016).

80. Rajapitamahuni, A., Hoffman, J., Ahn, C. H. & Hong, X. Examining graphene field effect sensors for ferroelectric thin film studies. *Nano Lett.* **13**, 4374–4379 (2013).

81. Fatemi, V. *et al.* Magnetoresistance and quantum oscillations of an electrostatically tuned semimetal-to-metal transition in ultrathin WTe_2. *Phys. Rev. B* **95**, 041410 (2017).

82. Yang, Q., Wu, M. & Li, J. Origin of two-dimensional vertical ferroelectricity in WTe_2 bilayer and multilayer. *J. Phys. Chem. Lett.* **9**, 7160–7164 (2018).

83. Yasuda, K., Wang, X., Watanabe, K., Taniguchi, T. & Jarillo-Herrero, P. Stacking-engineered ferroelectricity in bilayer boron nitride. *arXiv:2010.06600 [cond-mat]* (2020).

84. van Benthem, K., Elsässer, C. & French, R. H. Bulk electronic structure of $SrTiO_3$: Experiment and theory. *Journal of Applied Physics* **90**, 6156–6164 (2001).

85. Cowley, R. A. Temperature dependence of a transverse optic mode in strontium titanate. *Phys. Rev. Lett.* **9**, 159–161 (1962).

86. Müller, K. A. & Burkard, H. $SrTiO_3$: An intrinsic quantum paraelectric below 4 K. *Phys. Rev. B* **19**, 3593–3602 (1979).

87. Veyrat, L. *et al.* Helical quantum Hall phase in graphene on $SrTiO_3$. *Science* **367**, 781–786 (2020).

88. Maher, P. *et al.* Evidence for a spin phase transition at charge neutrality in bilayer graphene. *Nature Physics* **9**, 154–158 (2013).

89. Young, A. F. *et al.* Tunable symmetry breaking and helical edge transport in a graphene quantum spin Hall state. *Nature* **505**, 528–532 (2014).

90. Sanchez-Yamagishi, J. D. *et al.* Helical edge states and fractional quantum Hall effect in a graphene electron–hole bilayer. *Nature Nanotechnology* **12**, 118–122 (2017).

91. Song, T. *et al.* Switching 2D magnetic states via pressure tuning of layer stacking. *Nature Materials* **18**, 1298–1302 (2019).

92. Li, T. *et al.* Pressure-controlled interlayer magnetism in atomically thin CrI_3. *Nature Materials* **18**, 1303–1308 (2019).

93. Park, J. H. *et al.* Measurement of a solid-state triple point at the metal–insulator transition in VO_2. *Nature* **500**, 431–434 (2013).

94. Fu, L. & Kane, C. L. Superconducting proximity effect and Majorana fermions at the surface of a topological insulator. *Phys. Rev. Lett.* **100**, 096407 (2008).

95. Fundazioa, E. $NbSe_2$, a true 2-D superconductor. https://phys.org/news/2015-11-nbse2-true-d-superconductor.html.

96. Wang, H. *et al.* High-quality monolayer superconductor $NbSe_2$ grown by chemical vapour deposition. *Nat Commun* **8**, (2017).

97. Kim, M. *et al.* Strong proximity Josephson coupling in vertically stacked $NbSe_2$–graphene–$NbSe_2$ van der Waals junctions. *Nano Lett.* **17**, 6125–6130 (2017).

98. Lee, G.-H. *et al.* Electron tunneling through atomically flat and ultrathin hexagonal boron nitride. *Appl. Phys. Lett.* **99**, 243114 (2011).

99. Britnell, L. *et al.* Electron tunneling through ultrathin boron nitride crystalline barriers. *Nano Lett.* **12**, 1707–1710 (2012).

VITA

Bosong Sun was born in Tianjin, China. He earned his bachelor's degree in physics from University of Science and Technology of China in 2013. Then he joined the University of Washington. He pursued his Ph.D. degree in physics under the advising of Prof. David Cobden in Nanodevice Physics Lab.